POLISH ACADEMY OF SCIENCES – WROCŁAW BRANCH
WROCŁAW UNIVERSITY OF TECHNOLOGY

ARCHIVES OF CIVIL AND MECHANICAL ENGINEERING

Quarterly
Vol. VI, No. 3

WROCŁAW 2006

ARCHIVES OF CIVIL AND MECHANICAL ENGINEERING
Vol. VI 2006 No. 3

The influence of the rolling direction of the joined steel sheets on the springback intensity in the case of Ω-shape parts made from tailor welded strips

A. ALBUT, G. BRABIE
University of Bacau, 157 Marasesti Street, 5500 Bacau, Romania

The final shape of the draw bended parts is seriously affected by the springback phenomenon. The present work deals with numerical simulation and experimental tests related to draw bending and springback of Ω-shape parts manufactured from tailor welded stripes and it is trying to prove out the important role that the rolling direction of the joined steel sheets has on the springback intensity. The experimental tests and the simulation by finite element method (ABAQUS) have been carried out using two different rolling directions and maintaining constant all other parameters.

Keywords: *springback, draw bending, tailor welded stripes, rolling direction*

1. Introduction

A tailor-welded blank consists of two or more sheets that have been welded together in a single plane prior to draw bending. The sheets joined by welding can be identical, or they can have different thickness, mechanical properties or surface coatings. Since the springback is affected by the material properties (such as Young's modulus and initial yield stress, Poisson's coefficient, constitutive behaviour in plastic field), the punch and die profile radii, the clearances between punch and die, the friction conditions, the blankholder force, the welding line position, etc., the design of the drawing process for tailor-welded stripes is more complicated than in the case of homogeneous ones [1–4].

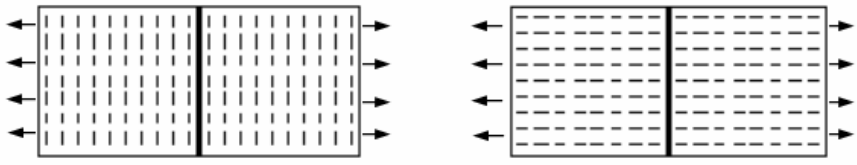

Fig. 1. Different orientation of the welding line with respect to the rolling direction

The rolling direction (RD) of the materials with respect to the draw bending direction has a great influence on springback intensity as well as on the material formability. The purpose of this study was to investigate the influence of the material rolling

direction on the springback parameters in the case of the tailor-welded strips. To achieve this goal, simulation and experimental test were carried out with the weld line perpendicular to the draw bending direction and the material rolling directions parallel and perpendicular to the direction of the deforming force applied (Figure 1).

2. Experimental investigation concerning the influence of the material rolling direction

2.1. Experimental methodology

The tailor-welded stripes used in experiments were made by joining the FEPO and E220 steels sheets. The strips of 350×30 mm dimensions and 0.7 mm thickness were cut out from the tailored blank in the rolling direction along and perpendicularly to the deforming force. The variation of the following springback parameters was analyzed during the tests: θ_1 – sidewall angle between real profile and theoretical profile; θ_2 – flange angle between real profile and theoretical profile; ρ – curvature radius of the sidewall (Figure 2).

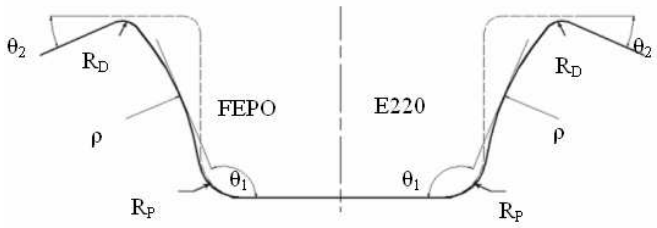

Fig. 2. Springback parameters

Fig. 3. Experimental device

The experimental investigations were performed using the die shown in Figure 3, whose geometry is presented in Table 1. The profile of the part obtained and the parameters of springback were measured with a 3D numerical controlled scanning machine. The data obtained were processed using the AutoCAD software. In order to minimize the influence of the blankholder force, its value was constant and equal to 10 kN. The draw bending tests have been done with lubrication of the tools and TWB sample.

Table 1. Die geometric parameters

Punch geometry (mm)	78×120
Punch profile radius (mm)	10
Die opening (mm)	80
Die profile radius (mm)	5
Punch stroke (mm)	50

2.2. Experimental results of the influence of rolling direction

The values of springback parameters resulted from the experimental tests are graphically represented in Figures 4, 5 and 6 and given in Table 2.

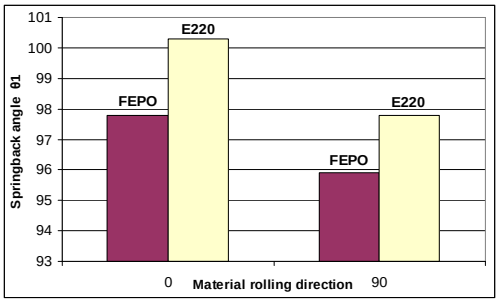

Fig. 4. Variation of the angle θ_1

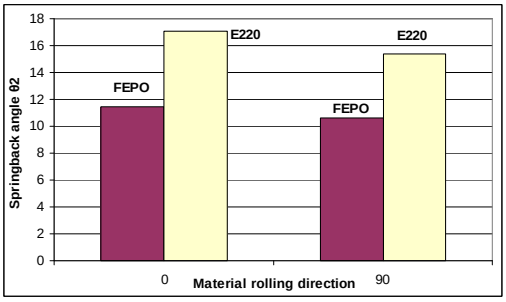

Fig. 5. Variation of the angle θ_2

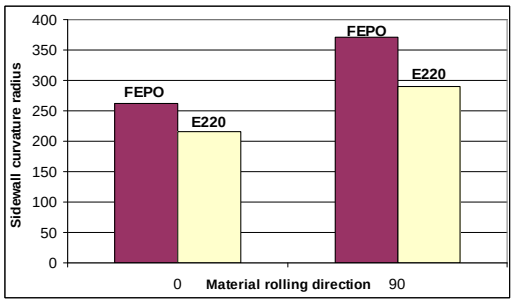

Fig. 6. Variation of the sidewall curvature radius ρ

Table 2. Springback parameters

Rolling direction position [grd]	Zone of the part made from FEPO steel						Zone of the part made from E220 steel					
	Angle θ_1 [grd]		Angle θ_2 [grd]		Sidewall radius [mm]		Angle θ_1 [grd]		Angle θ_2 [grd]		Sidewall radius [mm]	
	Theo-retical	Meas-ured	Theo-retical	Meas-ured	Theo-retical	Meas-ured	Theo-retical	Measured	Theo-retical	Measured	Theo-retical	Measured
0^o	90	97.8	0	11.5	∞	262.84	90	100.3	0	17.1	∞	214.82
90^o	90	95.9	0	10.6	∞	371.16	90	97.8	0	15.4	∞	289.12

Based on the above results the following conclusions can be drawn: the modification of the rolling direction affects the springback parameters of the Ω-shape part; the values of the angles θ_1 (Figure 4) and θ_2 (Figure 5) are higher when the rolling direc-

tion of the TWB sample is parallel to the deforming direction; the sidewall radii ρ are smaller when the TWB sample has the rolling direction parallel to the deforming direction (Figure 6); the springback intensity is smaller in the part area made from FEPO steel in comparison with the E220 steel area for both rolling directions.

3. Analysis by simulation of the influence of the material rolling direction

3.1. Simulation methodology

The simulation of the Ω-shape part draw bending was run by using the ABAQUS software. The geometrical parameters analyzed are the sidewall radius ρ and the springback angles θ_1 and θ_2. The simulations considered a plane strain state. The material was modelled as elastic-plastic, the plastic behaviour being modelled as anisotropic using the Hill's quadratic anisotropic yield criterion. The geometric model used in simulation is presented in Figure 7.

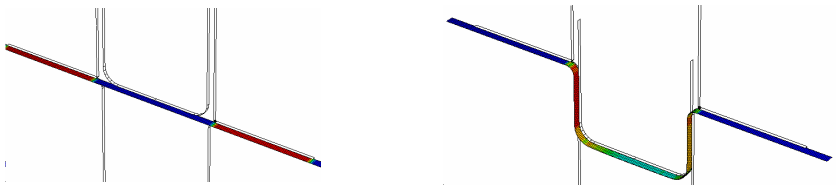

Fig. 7. Geometrical model

The initial dimensions of the sheet were 350 mm length, 30 mm width and 0.7 mm thick. The sheet was modelled as deformable body with 400 shell elements (S4R) on one row with 5 integration points through the thickness. The tools (punch, die and blankholder) were modelled as analytical rigid body. This modelling will lead to a reduced calculus efforts and a better contact behaviour. The rigid body movements were controlled by the reference points.

The boundary conditions imposed on the tools were intended to describe as accurately as possible the experimental conditions. A modified Coulomb friction law combined with penalty method was used to describe the contact condition.

3.2. Simulation results of the influence of rolling direction

The variations of springback parameters (θ_1, θ_2, ρ) as a function of material rolling direction are presented in Figures 8–10 and recorded in Table 3.

From the results presented above the following aspects can be remarked: the modification of the rolling direction affects the springback parameters of the Ω-shape part; the angles θ_1 (Figure 8) and θ_2 (Figure 9) attain higher values when the part is made from TWB having the rolling direction parallel to the deformation direction; the side-

wall radii ρ are smaller when the TWB sample has the rolling direction parallel to the deformation direction (Figure 10); the part area made from FEPO is not so much affected by the springback phenomenon in comparison with E220 steel area for both rolling directions.

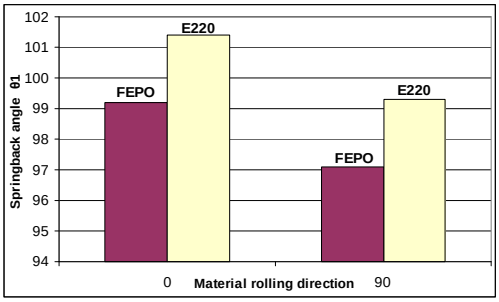

Fig. 8. Variation of the angle θ_1

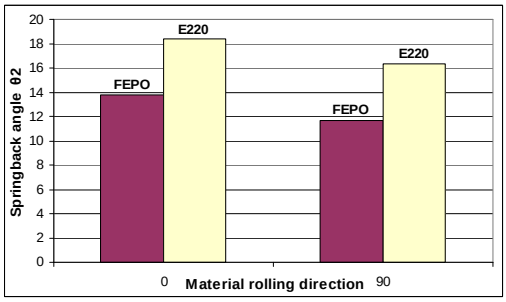

Fig. 9. Variation of the angle θ_2

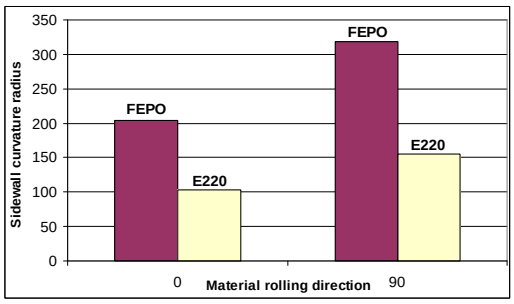

Fig. 10. Variation of the sidewall curvature radius ρ

Table 3. Springback parameters

Rolling direction position [grd]	Zone of the part made from FEPO steel						Zone of the part made from E220 steel					
	Angle θ_1 [grd]		Angle θ_2 [grd]		Sidewall radius [mm]		Angle θ_1 [grd]		Angle θ_2 [grd]		Sidewall radius [mm]	
	Theo-retical	Meas-ured	Theo-retical	Meas-ured	Theo-retical	Meas-ured	Theo-retical	Meas-ured	Theo-retical	Meas-ured	Theo-retical	Measured
0^o	90	99.2	0	13.8	∞	203.93	90	101.4	0	18.4	∞	103.34
90^o	90	97.1	0	11.7	∞	318.72	90	99.3	0	16.3	∞	154.49

4. Analysis of the results obtained

By analyzing the variation of springback parameters obtained from the experimental and by simulation tests, we can draw the following conclusions:

- The tendencies of the variation of springback parameters are the same for both experimental or simulation tests.

• The results obtained from the finite element analysis are characterized by a slight tendency to underestimate the intensity of the springback compared to the experimental results (Table 4). The error arising from the difference between experimental and simulation results is approximately 1.3%.

• The differences between the experimental and simulation tests are caused by the assumption applied in simulation that the blankholder pressure is perfectly uniformly distributed, but in reality that is not true.

• It can be considered that the results generated by the analysis of springback phenomenon using finite element method are sufficiently accurate and can be considered valid.

Table 4. Springback parameters

Rolling direction position [grd]	Zone of the part made from FEPO steel						Zone of the part made from E220 steel					
	Angle θ_1 [grd]		Angle θ_2 [grd]		Sidewall radius [mm]		Angle θ_1 [grd]		Angle θ_2 [grd]		Sidewall radius [mm]	
	Exp. test	Sim. test	Exp. Test	Sim. test	Exp. test	Sim. test	Exp. test	Sim. test	Exp. test	Sim. test	Exp. test	Sim. test
0^o	97.8	99.2	11.5	13.8	262.84	203.93	100.3	101.4	17.1	18.4	214.82	103.34
90^o	95.9	97.1	10.6	11.7	371.16	318.72	97.8	99.3	15.4	16.3	289.12	154.49

The rolling direction of the joined sheets influences the intensity of the springback in the case of draw bending of tailor-welded blanks. One of the main causes that determine the differences between the variations of the springback parameters in the two analysed cases of the rolling direction positions can be the distribution of the stresses in different zones of the formed part. Thus, by analyzing the stress distribution on both faces of the part before and after springback (Figure 11) we can arrive at the following conclusions:

• In the case of both rolling directions, the springback determines a decrease in the stress values in comparison with the stresses generated in the part before the tools removing.

• In the case of both rolling directions, the material placed in the flange area and on the bottom of the part is subjected only to tensile stresses, but after removing the part from the draw bending tools no stresses are found in these areas. Hence, we can conclude that because of the stress equilibrium the flange and bottom of the part will not be affected by springback phenomenon.

• Most of higher stresses occur in the zones of the part corresponding to the die and punch radius profiles where the material grains are stretched and bended simultaneously. After the draw bending tools are removed, the grains from the neutral axis neighbourhood, deformed mostly in the elastic domain, are trying to take their initial position and cause geometric deviations of the part as the effect of springback.

• The 0º rolling direction will determine higher stresses on both faces (inner and outer) of the part in comparison with those generated in the case of the 90º rolling di-

rection. This is because in the case of 0º rolling direction, during the draw bending process the grains are only subjected to tensile or bending stresses, but in the case of 90º rolling direction an important amount of deformation energy is used to change the orientation of grains. This phenomenon is more obvious in the zone of the part made from FEPO steel because of its great resistance to deformation in comparison with E220 steel.

- The curvature of the sidewall in the part area made from E220 steel occurs in the case of the 0º rolling direction because of the stresses difference between external and internal faces of the part. During the draw bending process the grains located closer to the inner face of the part are more stressed in comparison with the grains placed closer to the external face of the part, especially because of the influence of the zones of deformations located in the areas of connection between the wall and flange and bottom.

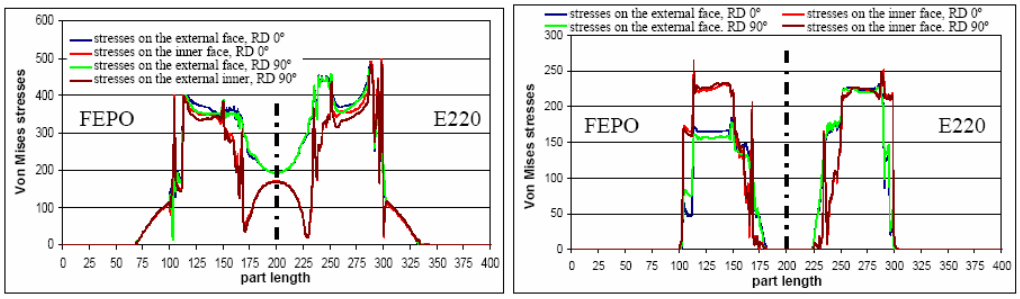

Fig. 11. Equivalent stress distribution along both faces of the part before and after springback

5. Conclusions

The following conclusions can be drawn from the present research concerning the influence of the rolling direction on springback parameters:

- The placing of the rolling direction perpendicularly to the direction of the deforming force leads to the reduction of springback intensity; the reduction of deviation from the theoretical profile is of about 6.5%.
- The draw bending of the samples having the rolling direction parallel to the deforming force can result in higher springback intensity or even the breaking in the deformation area; the increase of deviation from the theoretical profile is of about 8.6%.
- The springback of the zone of the part made from FEPO steel is smaller compared with the zone of the part made from E220 steel, because the strength of the E220 steel is higher than the strength of the FEPO steel.
- Springback intensity is influenced by the distribution of different stresses in different areas of the part. The 0º rolling direction determines higher stresses on both faces of the part in comparison with those generated in the case of the 90º rolling direction.

Acknowledgments

This research was performed with the financial support from the Romanian Ministry of Education and Research

References

[1] Lee J.K., Chun B.K., Kim H.Y.: *Numerical investigation of tailor welded blanks forming and springback*, Simulation of Material Processing, 2001, pp. 729–734.
[2] Samuel M.: *Experimental and numerical prediction of springback and side wall in u-bending of anisotropic sheet metals*, J. of Mat. Proc. Tech., 2000, pp. 382–393.
[3] Chirita B., Brabie G.: *Experimental analysis of different influences on springback of parts formed by u-bending*, 7th International Research/Expert Conference "Trends in the Development of Machinery and Asociated Technology" TMT 2003, Lloret del Mar, Barcelona, Spain, 15–16 September 2003.
[4] Han S.S., Park K.C.: *An investigation of the factors influencing springback by empirical and simulative techniques*, Numisheet'99, Besancon, France, 13–17 September 1999.

Wpływ kierunku walcowania na intensywność powrotnych odkształceń sprężystych wyrobów w kształcie litery Ω wykonanych z blach spawanych laserem

Końcowy kształt wyrobów kształtowanych w procesie gięcia w dużym stopniu zależy od zjawiska powrotnego sprężynowania. W pracy przedstawiono numeryczną symulację i badania doświadczalne dotyczące gięcia i sprężynowania powrotnego wyrobów w kształcie litery Ω, wytwarzanych z blach spawanych laserem. Wykazano istotną rolę kierunku walcowania spawanych laserem blach na intensywność powrotnych odkształceń sprężystych. Badania doświadczalne i symulacja metodą MES z użyciem programu ABAQUS zostały przeprowadzone dla dwóch różnych kierunków walcowania i z zachowaniem stałych pozostałych parametrów procesu.

ARCHIVES OF CIVIL AND MECHANICAL ENGINEERING

Vol. VI 2006 No. 3

Scale effect in shaft friction from the direct shear interface tests

L. BAŁACHOWSKI
Gdańsk University of Technology, Narutowicza 11/12, 80-952 Gdańsk

The thickness of the shear band mobilised on the pile shaft subjected to loading is practically the same for a small model and a large-diameter prototype. At the same normal stress applied to the shaft of the model and of the prototype pile, the normal stiffness of the interface and so the shear conditions are different for both cases. Lateral friction measured for the model and the prototype will differ. This scale effect in shaft friction related to the ratio of the diameter of the model to a mean grain size is studied with the direct shear interface tests, where the pile diameter is modelled with a constant normal stiffness applied to the shear box. The scale effect whose value is lower than unity is obtained for the dilative soil behaviour within the interface. The value of the scale effect smaller than unity is deduced from the direct shear interface tests with the soil contractancy.

Keywords: *model tests, direct shear box, constant normal stiffness*

Notations

d_{50} – mean grain diameter,
e – shear band width,
k – normal stiffness imposed,
u – displacement applied to the upper plate of the shear box,
u_1 – normal displacement at the boundary of the interface,
D – pile diameter,
E_p – pressuremeter modulus,
G – shear modulus,
I_D – density index,
K_0 - earth pressure coefficient at rest,
R – pile radius,
$\Delta\sigma_n$ – the increment of the normal stress to the shaft,
Δu – the increment of the normal displacement,
σ_n – normal stress,
σ_{n0} – initial normal stress,
σ'_v – effective overburden stress,
τ – shear stress,
$\tau_{k\ \mathrm{model}}$ – shear stress on model pile,
$\tau_{k\ \mathrm{prototype}}$ – shear stress on prototype pile,
$\tau_{(k=0)}$ – shear stress in constant normal stress condition,
$\tau_{(k=\infty)}$ – shear stress in no volume changes condition,
τ^* – scale effect.

1. Introduction

In physical modelling, some distortions of the prototype conditions, related to the grain size, can occur in granular soils. They are not taken into account in general si-

militude equations. These distortions are due to formation of shear bands at the interface between the soil and structure as for pile foundations, anchors and nailing or due to localization of the deformation in shear bands within the soil mass for retaining walls or shallow foundations. Observations of the shear zone in the direct shear interface box together with a research into localization have shown that the thickness of the shear bands depends mainly on an average size of grains, and typically approaches ten grain diameters (Desrues [1]). As the same soil is generally used in the model and the prototype, a distortion of physical modelling of foundations will be observed. When the behaviour of the foundation is governed by the mechanism of localization of the deformations in shear bands within the soil mass or by the formation of a shear zone at the interface between soil and structure, the scale effect related to the ratio of the model size to mean size of grains will appear. When the shear mechanism at the pile–soil interface is approximated by means of direct shear test, the different boundary conditions (i.e., the normal stiffness) will be applied to a small-diameter model and a large-diameter prototype pile.

In physical modelling, the development of such a new apparatus as centrifuge, where the miniaturization of models is forced by the limited size of container, requires a possible scale effect to be verified and quantified. One should note that if this scale effect can be responsible for some problems in the interpretation of physical modelling in granular material, it can be practically used and explored for the design of anchores and nails in granular material (Wernick [2], Schlosser and Guilloux [3], Lehane et al. [4]).

The scale effect in the case of shallow foundations has been studied by Habib [5], Kimura et al. [6], and Tatsuoka et al. [7]. They presented some requirements concerning the minimal size of the foundation with respect to the grain size in order to avoid the scale effect related to the localization of deformations within the soil mass.

Two distinct types of the soil behaviour within the interface can be identified. The first one that corresponds to the soil–pile interface presenting dilative behaviour, and the second one, in which the soil within the interface tends to contract during shearing. The analysis of the interface mechanisms has shown (Boulon and Foray [8], Boulon [9]) that a significant scale effect in the shaft friction measured on model piles can be expected due to formation of shear bands along the pile shaft. The scale effect on the shaft friction at rough model piles of different diameters (from 16 mm to 55 mm) embedded in Hostun dense quartz sand was studied in the centrifuge (Bałachowski [10]) for a dilative interface. These results were compared to the prediction given by the analysis of the interface mechanisms and the results of the direct shear interface tests using different normal stiffness (Foray et al. [11]). Garnier and König [12] performed a series of centrifuge tests with rough surface inclusions of different diameters (from 4 mm to 36 mm) embedded in dense Fontainebleau sand and the scale effect evaluated was similar to the previous results. In the case of perfectly smooth shafts, the skin friction in pull-out tests (Reddy et al. [13]) was practically the same regardless the di-

ameter of inclusion, and any scale effect due to shear band formation along the pile shaft was not observed.

In this paper, a complementary approach to centrifuge tests is presented and the scale effect in lateral friction due to shear band formation within the interface is evaluated based on the direct shear interface tests. It is estimated not only for the dilative interface as it was realized in centrifuge test (Bałachowski [10], Foray et al. [11]), but also for the contractive interface. Here, some quartz and carbonated sands are considered.

2. Direct shear interface tests

In the first approximation, the mechanism of the mobilisation of the skin friction along the pile shaft can be considered to be similar to a direct shear interface test with constant normal stiffness (CNS) k, corresponding to the lateral stiffness of the surrounding soil, as suggested in Figure 1. Volumetric changes of the soil within interface induce a normal displacement in the surrounding soil and the changes in the normal stress imposed on the shaft. A simple calculation (Wernick [2]) shows that k can be related to the pressuremeter modulus of the soil E_p (or G) by:

$$k = \frac{\Delta\sigma_n}{\Delta u} = \frac{2E_p}{R}, \tag{1}$$

where:

$\Delta\sigma_n$ – the increment of the normal stress imposed on the shaft,

Δu – the increment of the normal displacement,

E_p – the pressuremeter modulus,

R – the pile radius.

The extensive research program designed to describe the behaviour of the soil–structure interfaces was developed by Plytas [14], Boulon and Foray [8], Boulon [9], Genevois [15] and Hoteit [16] for quartz and carbonated sands using the direct shear interface box with CNS and smooth and rough interfaces. Airey et al. [17] developed cyclic direct shear interface tests with CNS for carbonated sands and studied skin friction degradation due to cyclic shearing.

In the case of the contractive behaviour of the soil within the interface, the normal stress reveals the tendency to decrease during shearing. For a given interface and for an initial normal stress this tendency is stronger at higher normal stiffness imposed on the box. Let us consider the dilative soil behaviour within the interface. As the soil tendency to dilate within the interface is restrained by the surrounding soil mass (normal stiffness imposed on the box), a significant increase in the normal stress can be observed during shearing. The greater the normal stiffness imposed on the box, the higher the normal stress mobilized in the direct shear interface test. The maximal dilatancy within the interface will be observed for dense sand, rough plate, low normal

stress and small normal stiffness. The maximal soil contractancy is expected for loose sand, smooth plate, high normal stress and great normal stiffness imposed on the box. Carbonated sand will contract better than quartz sand during shearing.

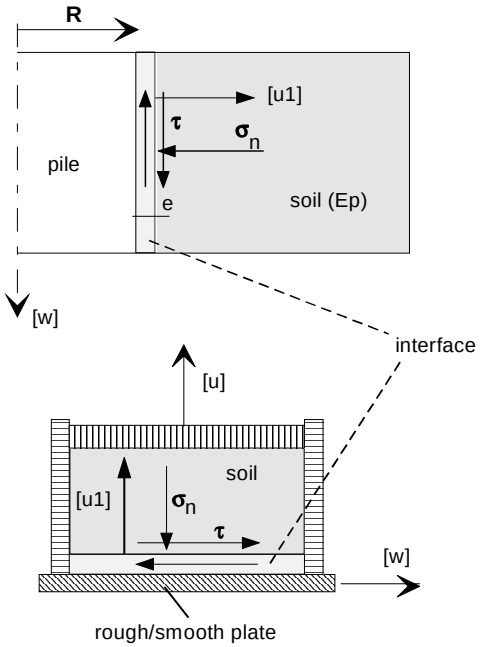

Fig. 1. The analogy between shear mechanism on the pile shaft and the direct shear interface test with constant normal stiffness (Boulon [8])

One should note that the normal stiffness is applied to the upper part of the shear box, and no to the interface itself. The normal displacement u_1 at the boundary of the interface (Figure 1) is larger than the displacement u applied to the upper plate of the shear box. The normal stiffness applied to the shear box and the shear stress measured should be theoretically adjusted to the compressibility of the soil sample in the upper part of the shear box. This adjustment could be made by taking into account unload–reload modulus measured either under oedometric conditions or in pressuremeter test. The influence of the soil compressibility in the upper part of the box can be however considered negligible, as the unload–reload modulus is even several times higher than the initial tangent one at a given stress level.

3. Definition of scale effect

A schematic presentation of the maximum shear stress as a function of CNS k is given in Figure 2 for the interface presenting dilative behaviour. As the normal stiffness applied to the box is inversely proportional to the pile radius, it should be greater

for a model pile than for a large-diameter prototype. Thus, at a given depth represented by a given initial normal stress and for a given sand density and interface roughness, a higher shear stress should be obtained in the case of a small-diameter model pile ($\tau_{k\ \mathrm{model}}$) than along the large prototype pile ($\tau_{k\ \mathrm{prototype}}$).

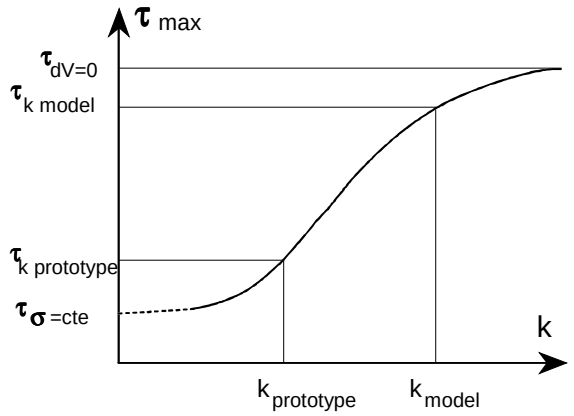

Fig. 2. Maximum shear stress vs. constant normal stiffness – dilative behaviour, Genevois [15]

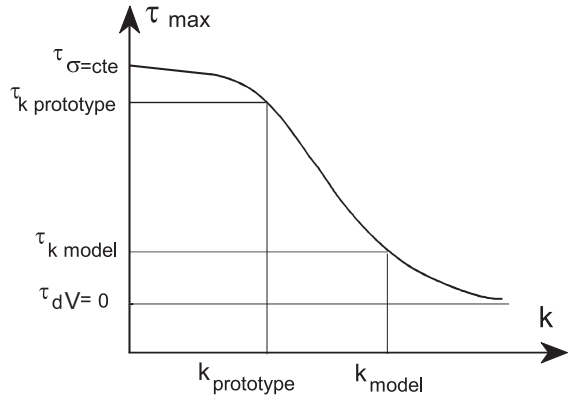

Fig. 3. Maximum shear stress vs. constant normal stiffness – contractive behaviour

An analogous schematic presentation of the maximum shear stress with the CNS *k* is given in Figure 3 for the contractive interface. In this case, at a given initial normal stress, sand density and interface roughness, a higher shear stress should be measured along the large-diameter prototype pile ($\tau_{k\ \mathrm{prototype}}$) than for a small-diameter model pile ($\tau_{k\ \mathrm{model}}$).

The scale effect for the shaft friction τ^* can be estimated based on the interface CNS tests according to the schemes in Figure 2 and Figure 3:

$$\tau^* = \frac{\tau_{k\,\text{model}}}{\tau_{k\ \text{prototype}}}. \tag{2}$$

It will be larger than unity for the dilative interface or smaller than unity in the case of the contractive behaviour of the soil within the interface. For a given interface (soil mineralogical characteristics, soil density, initial normal stress, grain size and plate roughness) this scale effect τ^* should be a function of the imposed normal stiffness, and for a given soil it should be related to the pile diameter.

3.1. Maximal scale effect

The extreme range of the normal stiffness will be either for large-diameter piles with small volumetric changes within the interface, which corresponds to a classical shear test with constant normal stress conditions ($k = 0$), or for small-diameter model piles with strong interface dilatancy/contractancy, which corresponds to the shear test with a high CNS. The upper boundary of the normal stiffness is no volume changes condition ($k = \infty$).

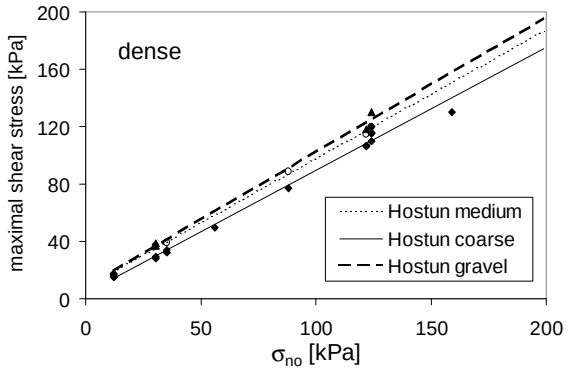

Fig. 4. Maximal shear stress from the direct shear interface test at constant normal stress–rough plate–Hostun material ($I_D \approx 0.8$)

Three different Hostun quartz sands were considered: medium (d_{50} = 0.32 mm), coarse (d_{50} = 0.7 mm) and gravel (d_{50} = 1.2 mm). An analysis of the direct shear interface tests with constant normal stress (Hoteit [16] and Plytas [14]) shows that the maximum shear stress for sands of the same mineralogical characteristics is practically independent of the grain size (Figure 4 and Figure 5). This conclusion will not be valid for very high normal stress applied to the box, or for carbonated sands, when a considerable grain crushing occurs, being the function of the grain size. On the other hand, the shear stress mobilized in CNS test should be related to the dilatancy/contractancy in the interface.

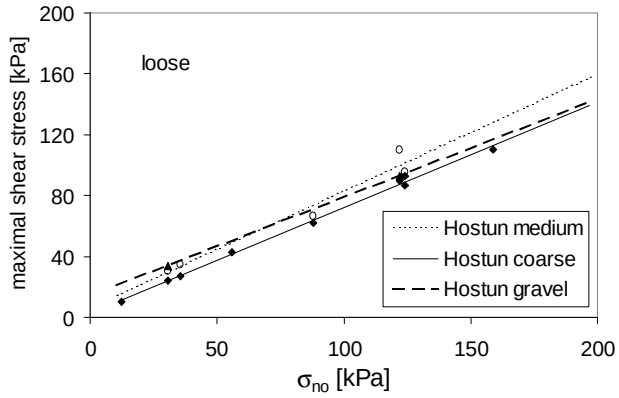

Fig. 5. Maximal shear stress from the direct shear interface test at constant normal stress–rough plate–Hostun material ($I_D \approx 0.3$)

The maximal scale effect in a given direct shear interface test is determined by taking into account two boundary conditions: no volume changes ($k = \infty$) and constant normal stress ($k = 0$):

$$\tau^*_{\max} = \frac{\tau_{(k=\infty)}}{\tau_{(k=0)}}. \tag{3}$$

The results of the direct shear interface tests under these two boundary conditions are given in Figure 6 for the Hostun medium sand.

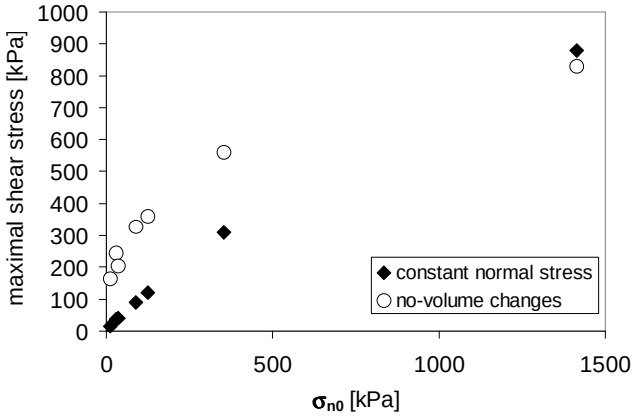

Fig. 6. Maximal shear stress under two extremal boundary conditions, i.e., dense Hostun medium sand and rough plate

The value of the maximal scale effect in friction for the interface presenting highly dilative behaviour (high density, rough plate) is given in Figure 7 for two quartz sands of the same mineralogical characteristic but different grain size. A larger grain size of the sand, a higher maximal scale effect (up to 20) observed in the direct shear interface test, especially at low initial normal stress applied to the shear box. The value of the maximal scale effect attenuates with initial normal stress and becomes negligible at very high initial normal stress.

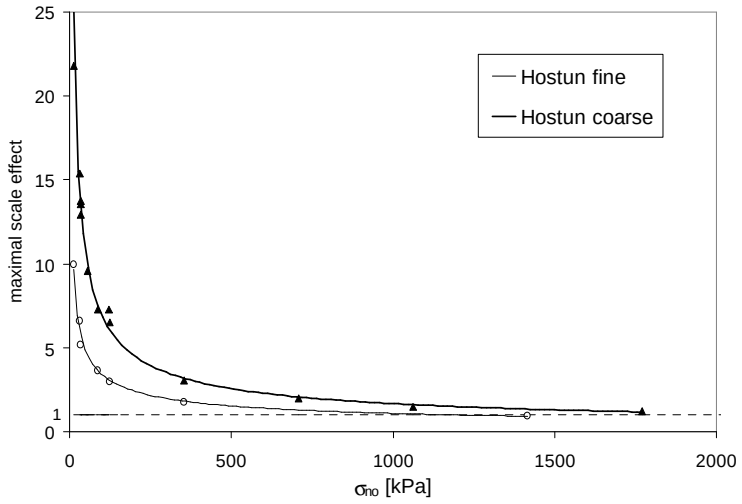

Fig. 7. Maximal scale effect from the direct shear interface box for two quartz sands and rough plate

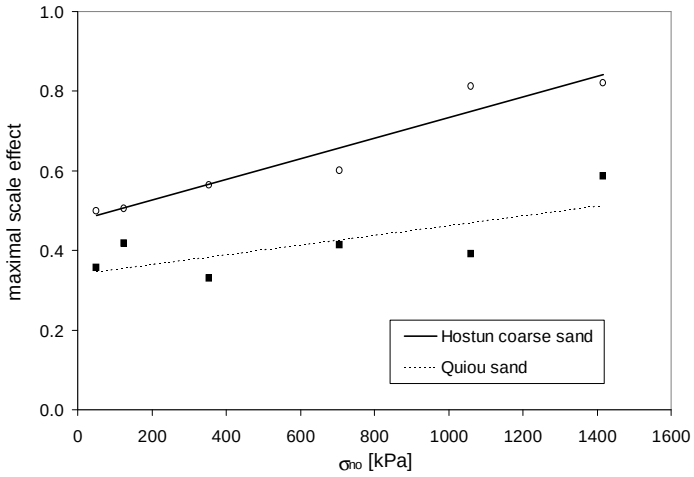

Fig. 8. Maximal scale effect from the direct shear interface box for Hostun quartz sand and Quiou carbonated sand

Maximal (less than unity) scale effect in friction for the contractive interface is given in Figure 8 for a smooth plate and two loose sands: Hostun coarse quartz sand and Quiou carbonated sand, Hoteit [16] and Plytas [14]. The highest scale effect is observed at low initial normal stress and steadily increases with initial normal stress applied to the shear box. For quartz sand the difference between the shear stress at constant normal stress and no volume changes shear tests will attenuate at high initial normal stress (about 2000 kPa). Due to important grain crushing in the shear box tests with carbonated sand, the maximal scale effect is lower in carbonated sand than in quartz sand and does not converge to unity.

3.2. Scale effect for model piles

The scale effect corresponding to the model piles of a given diameter can be estimated from the direct shear interface tests with CNS and shear modulus or pressuremeter modulus determined in calibration chamber according to the following procedure:

- the pressuremeter modulus is estimated for a given depth or vertical stress,
- earth pressure coefficient K_0 at rest is estimated,
- initial normal stress acting on the pile shaft is calculated according to formula (4),
- the constant normal stiffness k is calculated for each model and the prototype pile according to formula (1)

$$\sigma_{n0} = K_0 \, \sigma'_v. \tag{4}$$

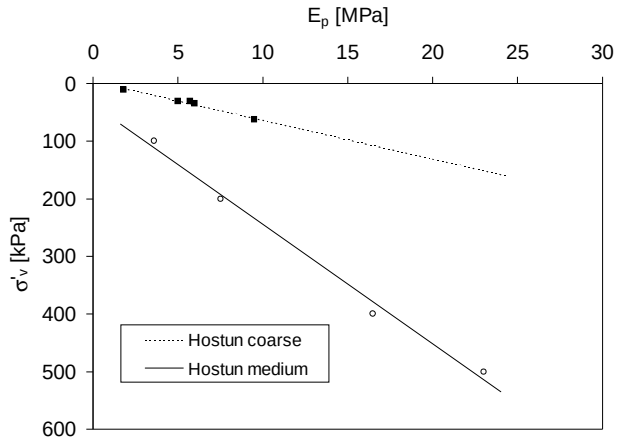

Fig. 9. Pressuremeter tangent modulus in dense sands determined in the calibration chamber in Grenoble

Taking into consideration the pressuremeter modulus data (Figure 9) determined in the calibration chamber by Mokrani [18] for two dense quartz sands and the results of

the direct shear interface tests with CNS, it is possible to estimate the constant normal stiffness for the model and the prototype piles.

3.2.1. Dilative interface

The values of maximal shear stress vs. imposed normal stiffness are available for Hostun dense medium (Figure 10) and Hostun dense coarse sand (Figure 11) and rough plate (Bałachowski [10]). One can estimate the shear stress corresponding to a given stiffness and initial normal stress for the model and for the prototype. The results of the direct shear interface tests at constant normal stress were applied to the prototype pile, 1600 mm in diameter, as its normal stiffness of the interface does not exceed 100 kPa/mm for both Hostun sands. For example, the normal stiffness for a prototype pile embedded in medium sand, calculated with (1) at effective overburden stress σ'_v = 200 kPa will be equal to 20 kPa/mm.

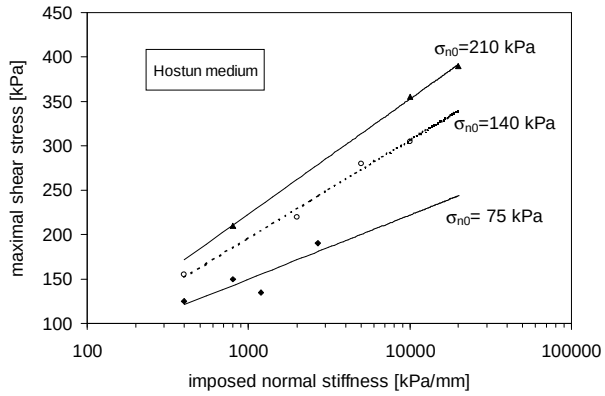

Fig. 10. Direct shear interface tests at CNS for Hostun dense medium sand–rough plate

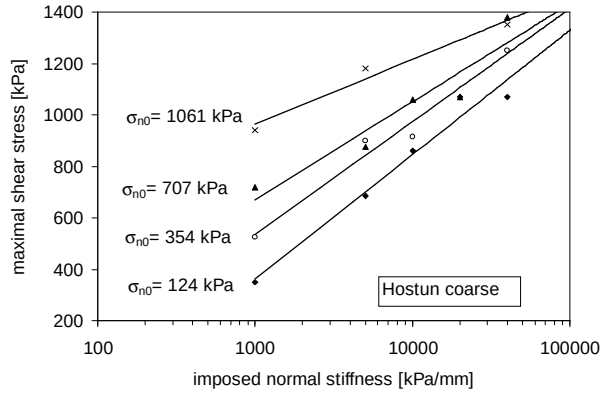

Fig. 11. Direct shear interface tests at CNS for Hostun dense coarse sand–rough plate

For a given depth (initial normal stress), the scale effect is determined to be the ratio of the maximal shear stress estimated for the model to the maximal shear stress for the prototype. It is presented in Figure 12 for Hostun medium sand as the function of the imposed normal stiffness.

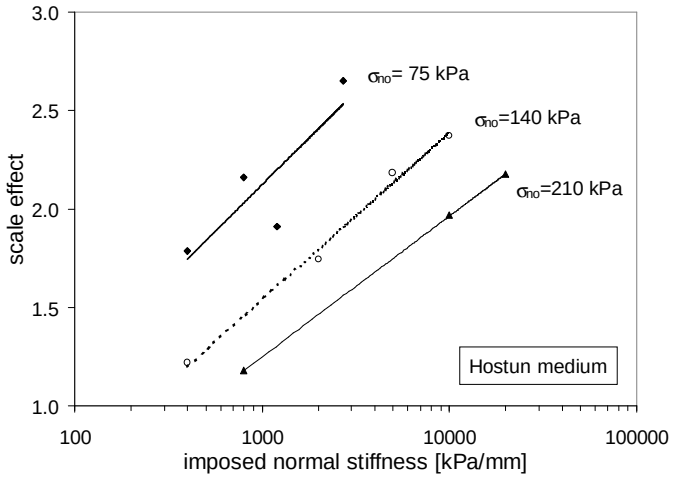

Fig. 12. Scale effect vs. imposed normal stiffness for dense Hostun medium sand–rough plate

The interface analysis showed that the shear band width e is a function of a mean grain diameter d_{50}. Here, it was assumed that:

$$e \approx 10 \cdot d_{50}. \tag{5}$$

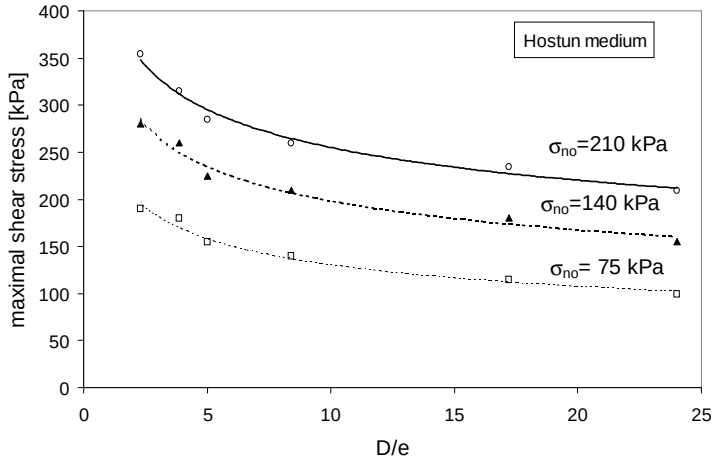

Fig. 13. Maximal shear stress vs. *D*/*e* ratio for dense Hostun medium sand–rough plate

For a given initial normal stress σ_{n0}, a constant normal stiffness k and the pile diameter D, the D/e ratio was calculated. Then the maximal shear stress (Figure 13) and the scale effect (Figure 14) in lateral friction were presented as the function of the D/e ratio and the initial normal stress applied to the box.

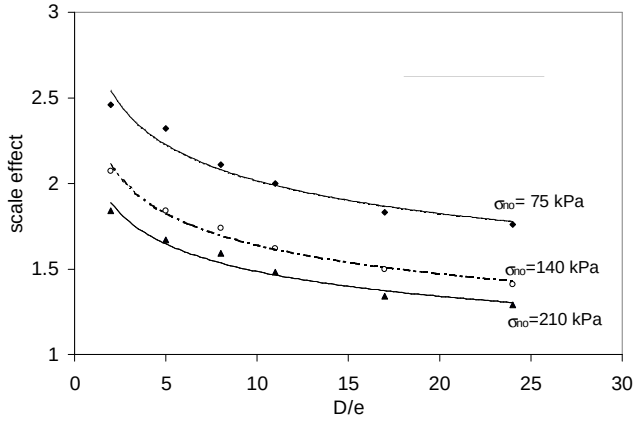

Fig. 14. Scale effect from direct shear interface test with CNS vs. D/e ratio, dense sand and rough plate

3.2.2. Contractive interface

In the case of contractive behaviour of the interface, the maximal shear stress decreases steadily with the imposed normal stiffness applied to the shear box (Figure 15 and Figure 16) (Hoteit [16]). The corresponding scale effect for loose, coarse Hostun quartz sand and loose carbonated Quiou sand and smooth plate is given in Figure 17

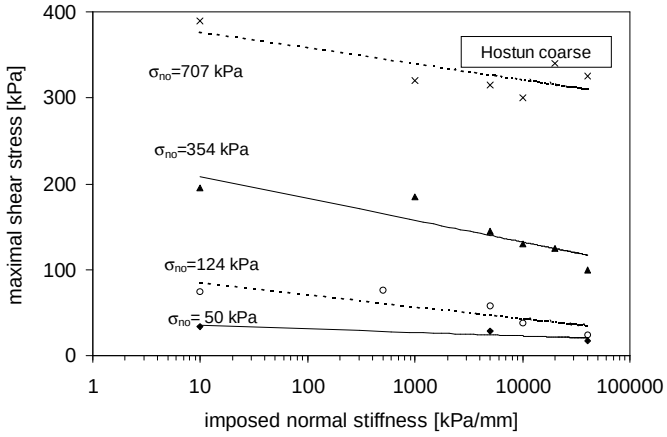

Fig. 15. Maximal shear stress for loose Hostun coarse sand and smooth plate

and Figure 18 as the function of the imposed normal stiffness; whereas its maximal value is presented in Figure 5. As carbonated sands are very sensitive to grain crushing, the scale effect is reduced more rapidly and the process starts at smaller normal stiffness imposed on Quiou sand (*k* of about 400 kPa/mm) than on Hostun one (*k* of about 4000 kPa/mm). Using the same approach as for the dilative interface, the scale effect for loose Hostun and Quiou sands and smooth plate was determined (Figure 19 and Figure 20) as the function of the *D/e* ratio. The strongest scale effect is observed for small models and great initial normal stress. It is stronger for carbonated sands than for quartz sands. This scale effect attenuates for the *D/e* ratio exceeding 20.

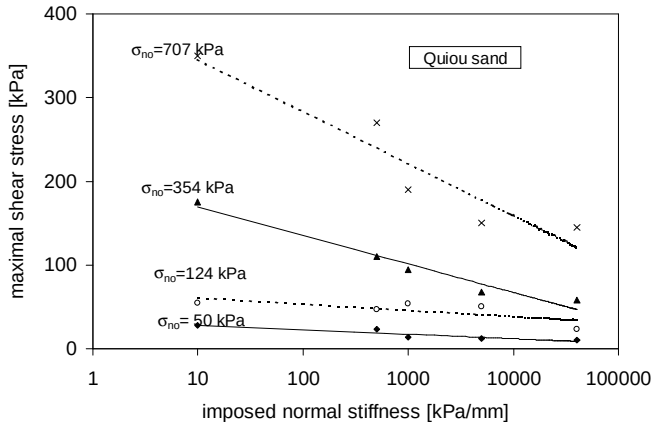

Fig. 16. Maximal shear stress for loose Quiou sand and smooth plate

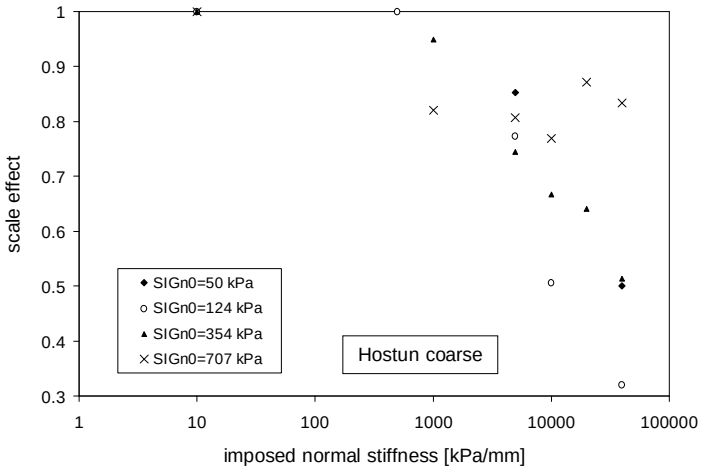

Fig. 17. Scale effect vs. normal stiffness imposed on loose Hostun coarse sand and smooth plate

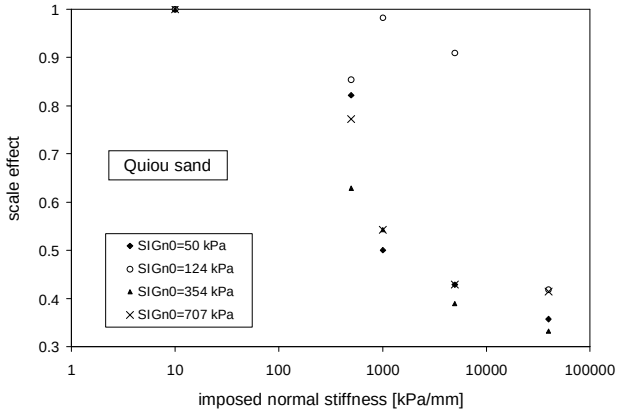

Fig. 18. Scale effect vs. normal stiffness imposed on loose Quiou sand and smooth plate

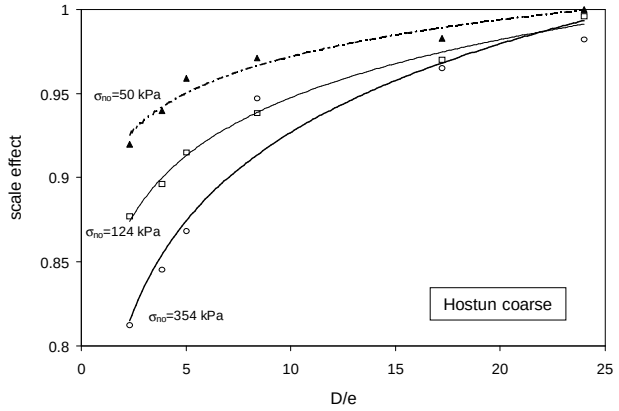

Fig. 19. Scale effect vs. the *D/e* ratio for loose Hostun coarse sand and smooth plate

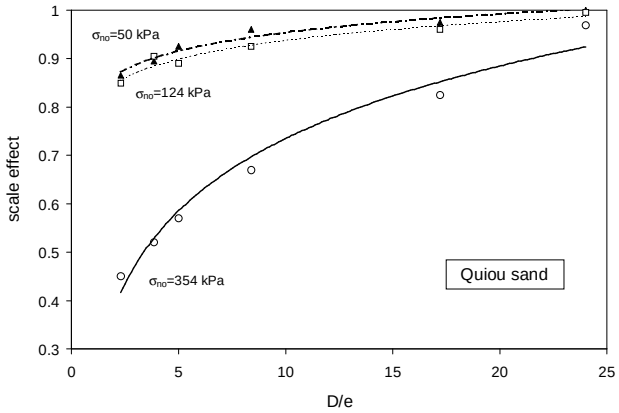

Fig. 20. Scale effect vs. the *D/e* ratio for loose Quiou sand and smooth plate

4. Conclusions

Scale effect in lateral friction due to shear band formation in the soil–structure interface was determined based on direct shear interface tests with constant normal stiffness. This scale effect greater than unity was obtained for the dilative interface, and smaller than unity – for contractive soil behaviour within the interface. For the latter, the scale effect in carbonated sand will be more pronounced than in quartz one.

The tests on small-diameter models should be carried out with a special attention. In order to avoid the scale effect, the diameter of the model should be larger than the sum of the diameters of 200 grains at highly dilative or contractive soil within the interface.

Making use of the direct shear interface test to model correctly the lateral friction mobilisation on the pile shaft, we have to take account of its limitations. They are as follows:

- For the inclusions of a very small diameter, the phenomenon is a really axisymmetrical problem and cannot be reproduced in plane strain conditions in the direct shear test. The circumferential stress influence and its evolution during the shearing cannot be reflected in the direct shear interface test.
- In the case of contractive soil behaviour within the soil–pile interface, the arching phenomena can appear and the contact between the contracting interface and the surrounding soil mass can be lost. These phenomena will not exist during the shear test in the interface shear box.
- In these cases, the scale effect determined with the direct shear interface tests will be underestimated.

Acknowledgements

The direct shear interface data comes from the Laboratory 3S in Grenoble. The author acknowledges the possibility of interpreting them.

References

[1] Desrues J.: *An introduction to strain localisation in granular media*. *Physics of granular media*, Proc. Winter School, Les Houches, February 1990, Nova Sciences Publications, pp.127–142.
[2] Wernick E.: *Stresses and strains on the surface of anchors*, Revue Française de Géotechnique, special number on the anchors, 1978, pp. 113–119.
[3] Schlosser F., Guilloux J.: *Le frottement dans le renforcement des sols*, Revue Française de Géotechnique, 1981, No. 16.
[4] Lehane B.M., Jardine R.J., Bond A.J., Frank R.: *Mechanisms of shaft friction in sand from instrumented pile tests*, JGE, 1993, Vol. 119, No. 1.
[5] Habib P.: *Effet d'échelle et surface de glissement*, Revue Française de Géotechnique 1985, No. 31.

[6] Kimura T., Kusakabe O., Saitoh K.: *Geotechnical model tests of bearing capacity problems in a centrifuge*, Géotechnique, 1985, No. 35.
[7] Tatsuoka F. et al.: *Progressive failure and particle size effect in bearing capacity of a footing on sand*, Geotechnical Engineering Congress, Geotechnical Special Publication No. 27 of ASCE, 1991.
[8] Boulon M., Foray P.: *Physical and numerical simulation of lateral shaft friction along offshore piles in sand*, 3rd Int. Conference on Numerical Methods in Offshore Piling, Nantes, 1986, pp. 127–147.
[9] Boulon M.: *Numerical and physical behavior under monotonous and cyclic loading*, [in:] Kolkman et al. (Ed.), *Modelling Soil–Water–Structure Interactions*, Rotterdam, Balkema, 1988, pp. 285–293.
[10] Bałachowski L.: *Différents aspects de la modélisation physique du comportement des pieux: chambre d'etalonnage et centrifugeuse*, Thèse de doctorat à l'INPG, 1995.
[11] Foray P., Bałachowski L., Raul G.: *Scale effect in shaft friction due to localisation of deformations*, Centrifuge'98, Tokyo, 1998, Kimura et al. (Ed.), Balkema, 1, pp. 211–216.
[12] Garnier J., König D.: *Scale effects in piles and nails loading tests in sands*, Centrifuge'98, Tokyo, Kimura et al. (Ed.), Balkema, 1998, 1, pp. 205–210.
[13] Reddy E.S., Chapman D.N., Sastry V.V.R.N. : *Direct shear interface test for shaft capacity of piles in sand*, Geotechnical Testing Journal, 2000, 23 (2), pp. 199–205.
[14] Plytas C.: *Contribution à l'étude expérimentale et numérique des interface sols granulaire-structure, application à la prévison du frottement latéral des pieux*, Thèse à l'Universite Joseph Fourier, Grenoble, 1985.
[15] Genevois J.M.: *Capacité portante des pieux à grande profondeur. Simulation physique à l'aide d'une chambre de calibration*, Thèse de doctorat à l'Université Joseph Fourier, Grenoble I, 1989.
[16] Hoteit N.: *Contribution à l'étude de comportement d'interface sable-inclusion et application au frottement apparent*, Thèse à l'Universite Joseph Fourier, Grenoble, 1990.
[17] Airey D.W., Al-Douri R.H., Poulos H.G.: *Estimating of pile friction degradation from shearbox tests*, Geotechnical Testing Journal, 1992, Vol. 15, No. 4, pp. 388–392.
[18] Mokrani L.: *Simulation physique du comportement des pieux à grande profondeur en chambre de calibration*, Thèse de doctorat à l'INPG, 1991.

Efekt skali dla tarcia na podstawie badań bezpośredniego ścinania w kontakcie

Przy tym samym naprężeniu normalnym na pobocznicy modelu pala o małej średnicy i prototypu o dużej średnicy zjawisko mobilizacji tarcia przebiega w innych warunkach brzegowych. Zjawisko to może zostać odzwierciedlone w badaniu bezpośredniego ścinania w kontakcie ze stałą sztywnością normalną, odwrotnie proporcjonalną do rozpatrywanej średnicy pala. Przeanalizowano wartości maksymalne tarcia uzyskane w aparacie bezpośredniego ścinania dla piasków kwarcowych i węglanowych oraz gładkiego i szorstkiego kontaktu przy różnym zagęszczeniu piasku. Określono efekt skali jako stosunek tarcia mobilizowanego na modelu do tarcia mobilizowanego dla pala o dużej średnicy. Efekt skali zmierzony w aparacie bezpośredniego ścinania w kontakcie przy stałej sztywności normalnej ma wartość większą od jednego w przypadku dylatancji w kontakcie lub wartość mniejszą niż jeden dla kontraktancji na styku konstrukcja–grunt.

ARCHIVES OF CIVIL AND MECHANICAL ENGINEERING

Vol. VI 2006 No. 3

Selected problems in evaluating topography of coated abrasives

S. ZABORSKI
Technical University of Wrocław, ul. Łukasiewicza 5, 50-371 Wrocław, stanislaw.zaborski@pwr.wroc.pl

W. PSZCZOŁOWSKI
Higher Education Institution for Managers in Legnica

The paper presents some problems connected with the topography of coated abrasives. Various classes of coating are discussed, ranging from conventional single-layer ones to modern engineered coatings of the TRIZACT type. Actual parameters of the active face for various makes are given. Principal in-service properties of abrasive belts are discussed: instantaneous grinding efficiency and variation in surface roughness of the machined workpiece. A grinding process model is outlined which, after completion, will be capable of controlling precisely automated grinding operations using coated abrasives.

Keywords: *topography, coated abrasives, TRIZACT type coating, grinding operations*

1. Introduction

In recent years, major advances in material removal processes using coated abrasives have been made. New design solutions and new abrasive materials have significantly extended their range of applications. Main benefits of the technology include: uniform cutting speed, tool flexibility, capacity for machining extensive areas, cutting forces and residual stresses lower than those in bonded abrasive grinding. Other advantages worth mentioning are such that there is no need for tool balancing, dressing and using grinding fluids [2].

Both literature studies and earlier investigations [2, 4, 5, 7] have clearly shown that there is no closed set of quantities that could define the active face of a coated abrasive. The number of grains or particles actively involved in cutting, their spatial geometry, extent and character of wear are considered to be the deciding factors. All they must be taken into account when designing optimized manufacturing processes.

2. Types of coated abrasives

Cutting properties of coated abrasives depend primarily on the type of abrasive mineral and the coating structure. The most widely used are single-layer continuous or programmed coats (with standard grit) available in grades from P16 to P2500 (Figure 1a). Their cutting performance can vary within broad limits due to varying sizes and shapes of grains, non-uniform grain coverage and different coat structure. The overall wear of the monolayer abrasives is relatively fast. Modern abrasive products

with structured coats of the TRIZACT type (Figure 1b) are free from these shortcomings.

Another solution offering exceptional advantages are single-layer structured coats made up of spherical abrasive particles of the HERMESIT type (Figure 2a), less patterned aggregate products (KULEX) (Figure 2b) [2] or highly patterned TRIZACT coatings (Figure 2c) [2, 3, 4, 6].

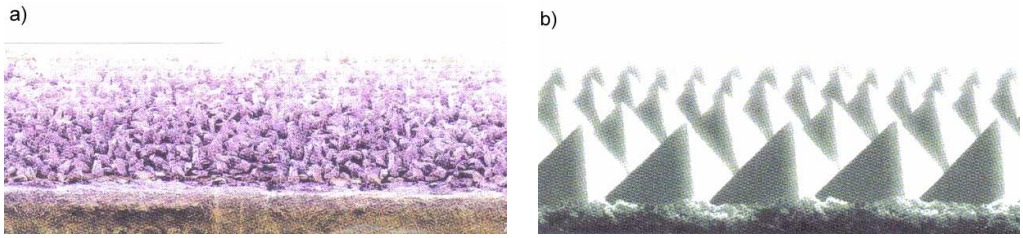

Fig. 1. Various types of coating: conventional (a), modern (TRIZACT type) (b) [6]

Such products offer improved grinding performance and cost-effective operation. The coat life is significantly longer and the material removal rate remains approximately constant till the complete wear-out of a tool. Products with the aforementioned coats yield consistently uniform finish on machined surfaces.

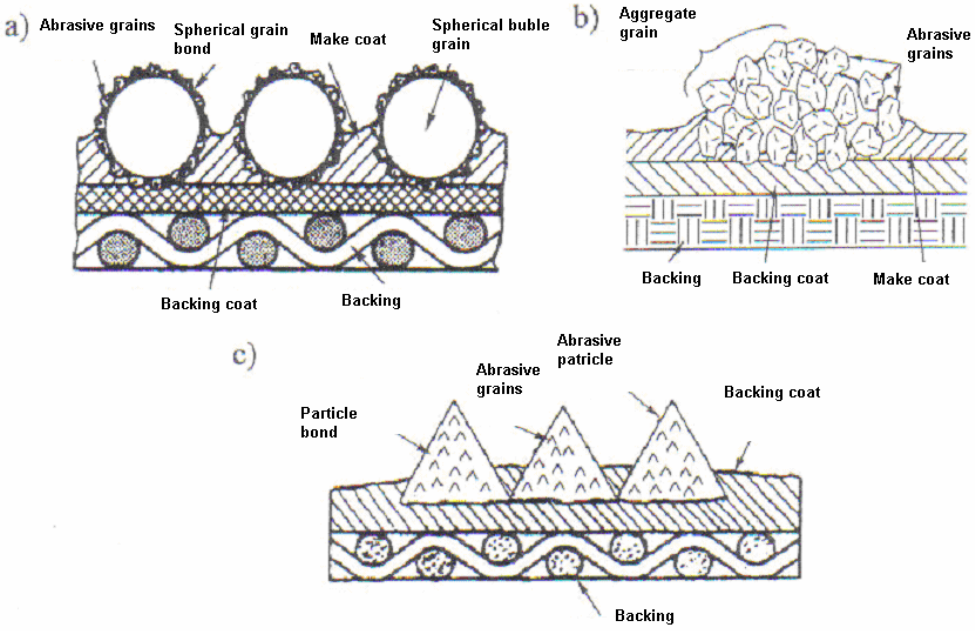

Fig. 2. Schematic cross-sections of coats made up of abrasive particles: spherical (a), aggregate (b), pyramidal (c)

3. Characteristics of the active surface of coated abrasives

Topography of the active face of a coated abrasive may be analyzed in the static conditions, i.e., for a tool itself, and in the dynamic conditions, i.e., for a tool in actual operation. In coated abrasives, the continuous wear of the cutting layer gives rise to extremely large differences between the coat topography in the two conditions.

From the geometrical point of view the active surface of a coat may be considered as a set of irregularities produced by spherical abrasive particles bonded to the backing. Papers [1, 2, 4, 5] have clearly indicated that cutting performance of coated abrasives is primarily affected by the topography of their active face whose defining characteristics are as follows:

- the size and shape of an individual abrasive particle,
- the number of abrasive particles per a unit area (N_{st}),
- the spacing between abrasive particles (l_{st}) and its statistical distribution,
- the number of standard grains on the active face of a particle,
- the height of the particle vertex above the make coat level and its statistical distribution.

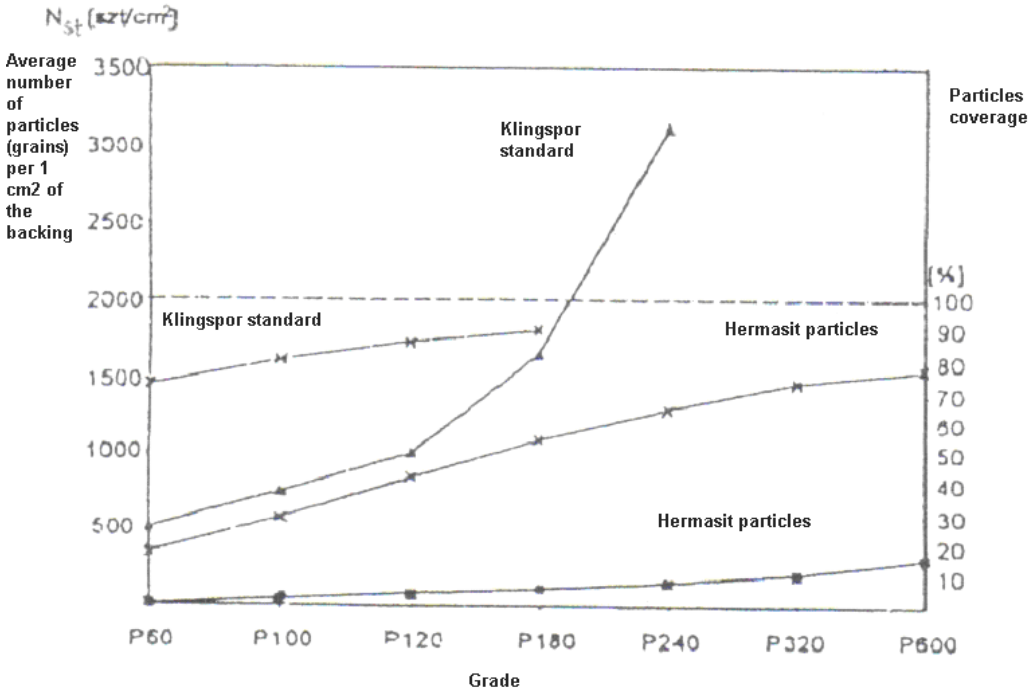

Fig. 3. Comparison of the number N_{st} of particles making up the active face of a belt as a function of coating grade

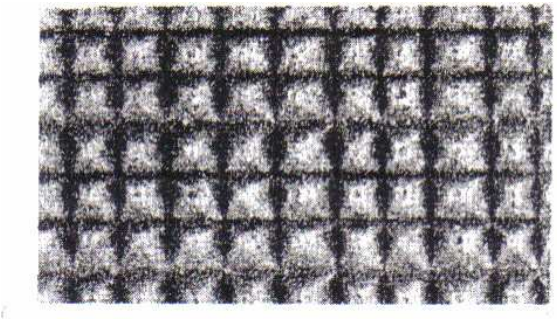

Fig. 4. A TRIZACT abrasive of A16 grade

The investigations have shown that in standard coatings at the same grain size there can be 10 to 20 times more grains per a unit area than abrasive particles. At larger grains the ratio becomes even higher. It should also be noted that the belts with structured coats have limited grain coverage compared with that of standard coats (Figure 3).

When comparing various mucker belts with coats made up of bubble particles or aggregates it is possible to note that differences in the number of particles of the same grade per a unit area are small.

Spherical abrasive particles are well defined in shape, and their size is by 8–9 times larger than that of standard grains of the same grade. The coatings covering the range from P60 to P120 may be considered as tools with full coat.

Histograms of particle spacing show that the frequency of finding the same distance is close to the normal distribution irrespective of grade. The higher the grade, the more uniform the spacing value – the tendency can be easily judged based on the standard deviation value.

The structured coats of the TRIZACT type were analysed in the same way. Profilograms and computer visualization techniques showed that the belts investigated contained two types of particles:

a) coats from the A6–A65 range had 20 particles along the 10 mm gauge length,

b) coats from the A80–A160 range had 15 particles along the 10 mm gauge length.

It was further shown that the abrasive particles were shaped as tetragonal pyramids with the bases of 0.45×0.45 mm and 0.6×0.6 mm, with the vertex angles ranging from 60 to 90 degrees.

The height of the abrasive polyhedrons, whatever the grade, ranged from 260 to 360 μm and the vertices formed a highly regular pattern.

4. Performance characteristics of structured coated abrasives

The two performance characteristics were determined for the abrasive belts tested:

- changes in instantaneous grinding efficiency defined as mass of material removed in a unit of time Q(g/s) over the whole operation time in minutes (Figure 5),

- changes in surface roughness index R_a(μm)) over the whole operational time (Figure 6).

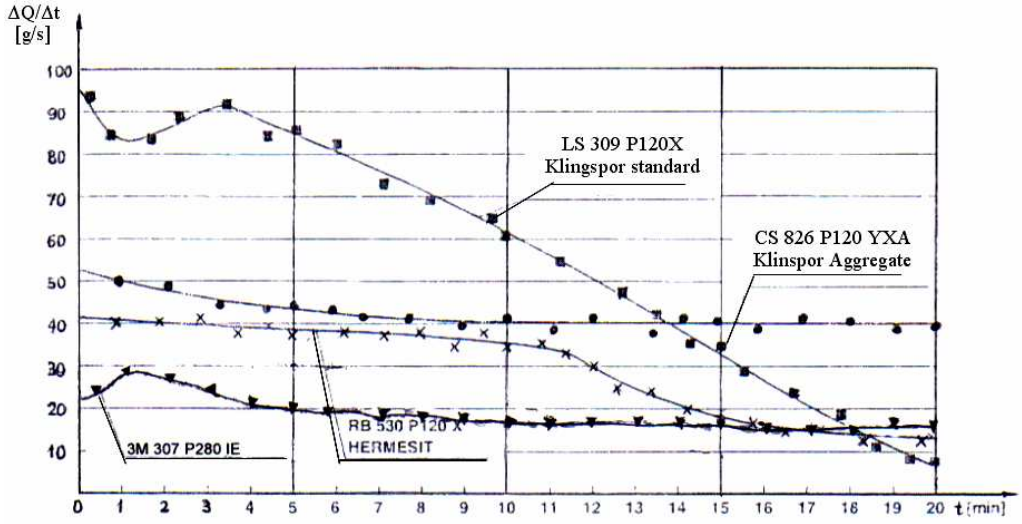

Fig. 5. Instantaneous grinding efficiency as a function of time

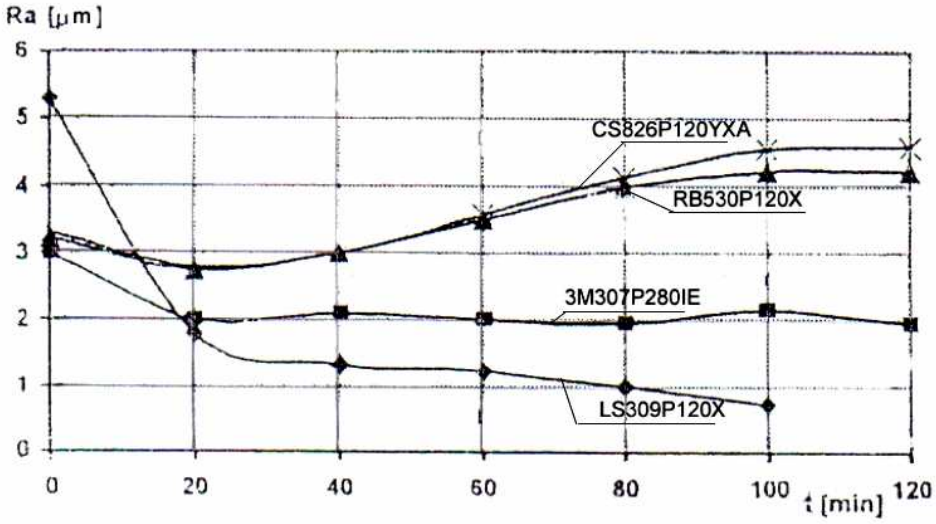

Fig. 6. The effect of coating type on the surface roughness index R_a with the grinding time t

The following belts were tested:

1. LS309 P120X single-layer coated (KLINGSPOR).

2. CS826 P120YXA with aggregate particles (KLINGSPOR).
3. RB530 P120X with abrasive particles of the HERMESIT type (HERMES).
4. 3M 307 P280JE with abrasive particles of the TRIZACT type (3M).

The tests were performed in grinding under a constant contact force F_y = 10 N. The ground specimens of 1.0 cm^2 cross-section area were made of 0.45% steel. A flat contact roller of a Sh90 hardness was used, the grinding speed was v_s = 30 m/s.

The following findings shall be listed:

- Among the structured coating belts, the products No. 2 and 4 had the most stable grinding efficiency. Also, the respective volumes of material removed were the highest of them all (Figure 5).
- If absolute values of the instantaneous grinding efficiency in an initial stage of the operation are to be taken into account, the highest values are obtained for belts with standard coating LS309. This behaviour is accompanied by the most rapid decrease in the grinding efficiency.
- The narrowest scatter of the roughness index R_a was found for RB530 belts which managed to maintain this quality during the whole test period.

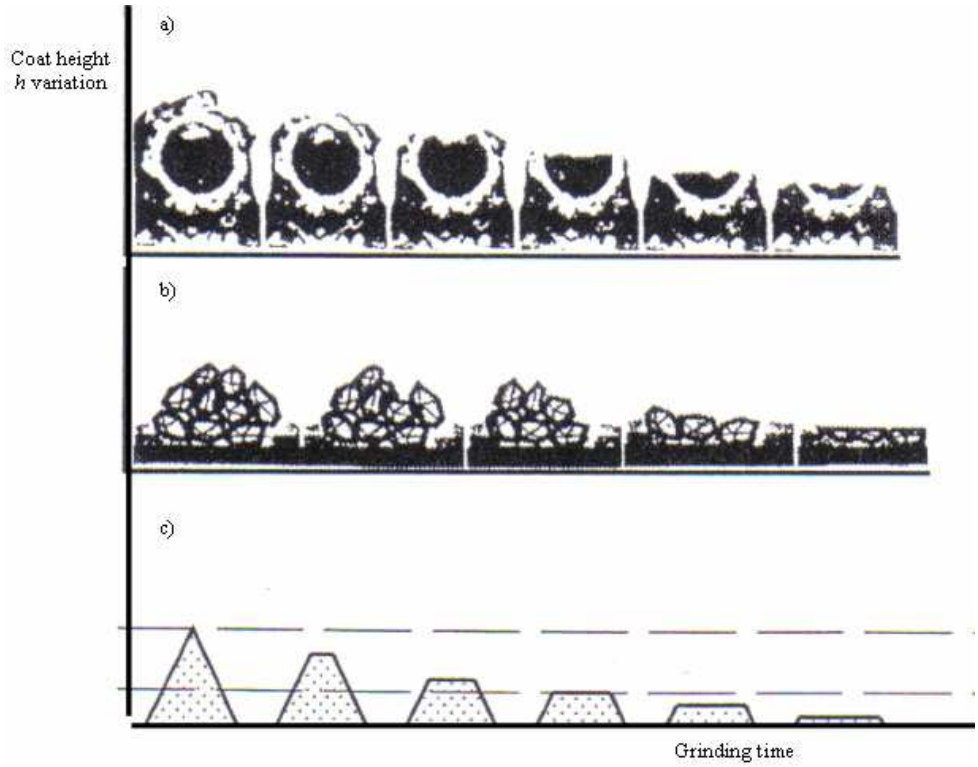

Fig. 7. Schematic illustration of how the particular types of coating are being worn: *a* – HERMESIT particles, *b* – KULEX particles, *c* – TRIZACT particles

The appearance of plots $Q = f(t)$, $R_a = f(t)$ and $h = f(t)$ (Figure 7) is closely related to characteristic structural features of the coatings tested and their behaviour in service. As shown in [2], standard belts have the highest number of grains per a unit area and thus their better efficiency in the initial stages of the process is fully understood. Their cutting ability becomes gradually reduced due to wear (Figure 5). In structured coatings, a smaller number of particles are involved in cutting in the initial stages of the operation and thus their efficiency is generally lower than in the former case. On the other hand, the fracture or fragment of particles is exposed to a moderate rate so that new sharp structure edges are produced. The overall result is that the efficiency remains almost constant (Figure 7).

To sum up, the structured coats have better properties than the monolayer ones. Their uniform performance with time, measured in terms of both cutting efficiency and quality of finish, makes them a preferred choice for numerically controlled grinders.

5. A subsystem for optimizing coat parameters

Modular manufacturing processes set high requirements concerning accuracy and quality of machining operations and thus the role of finishing operations gets more and more important. For a variety of machined materials involved one has to use belts with a rigorously selected set of structural features [3, 7]. The structured/engineered coatings can be exactly adjusted to a grinding job. The grain coverage can be controlled by selecting both the type of grain/particle deposition pattern and the value of spacing.

A fine type of tool as it is, a structured belt due to its structural complexity is a difficult component to be integrated into an automated grinding process.

The authors have devised a test programmer for: 1) analyzing, controlling and optimizing the coat parameters, and 2) relating them to the grinding operation outcome.

A generalized criterion for most grinding operations will be the particle coverage index K_n relating the necessary number of particles within the cutting zone to the stipulated grinding efficiency of a tool and the required surface finish quality. The input and output variables for the model are: grain composition of an abrasive, grain (particle) grade, structural features of a coat, physical–mechanical properties of a machined material, workpiece surface roughness index prior to and following the operation, grinding allowance, grinding process variables (grinding speed, contact force etc).

The model constructed will be capable of controlling the process by varying the radial component of the cutting force – the force being easily measured and controlled. The test goal presented forms a principal subject of a doctor's thesis to be completed soon.

6. Final remarks

For a consistent high-quality finish in belt grinding it is necessary to use belts with structured coats. Their performance characteristics are generally better than those of

conventional coats. For most grinding jobs, the optimization criterion should be the abrasive particle coverage index as related to the grinding efficiency of a belt.

The process model to be constructed soon by the present authors shall relate the geometry of the ground surface to both structural characteristics of the belt coat and variables of the grinding operation.

References

[1] Hallum D.L.: *Grinding innovations increase choices*. American Machinist, 1996, 140, 1.
[2] Pszczołowski W., Rosienkiewicz P.: *Grinding with coated abrasives* (in Polish), WNT, Warszawa, 1995.
[3] Dennis P.: *Superfinisch mit Diamantbändern*, Industrie Anzeiger, 1990, 112, 73, 80–84.
[4] Morazow W.A.: *Prospects for applying structured coated abrasives in modular machining processes* (in Polish), Technologia i automatyzacja montażu, 1996, 1.
[5] Pszczołowski W., Pszonka A.: *Scout investigations on a new class of coated abrasives as viewed by surface engineering* (in Polish), Raporty ITMiA serii Spr, 42/96, Wrocław, 1996.
[6] Company catalogues (Klingspor, 3M, Hermes, Vitex).
[7] Pszczołowski W., Rosienkiewicz P.: *Topography of coated abrasives in commercial abrasive products* (in Polish), XXI Naukowa Szkoła Obróbki Ściernej, Warszawa, 1998.

Wybrane problemy oceny topografii ściernych nasypów przestrzennych

Przedstawiono wybrane problemy związane z topografią przestrzennych nasypów ściernych. Omówiono różne nasypy ścierne (od standardowego do nowoczesnego przestrzennego nasypu typu TRIZACT). Podano parametry czynnej powierzchni narzędzi nasypowych. Istotnym zagadnieniem rozpatrywanym są właściwości eksploatacyjne taśmy ściernej wyrażone przez zmianę wydajności chwilowej szlifowania i zmianę chropowatości obrobionej powierzchni. Poczynione będą próby opisania doboru najkorzystniejszych parametrów nasypu ściernego dzięki wprowadzeniu modułów dla różnych warunków obróbki.

ARCHIVES OF CIVIL AND MECHANICAL ENGINEERING

Vol. VI 2006 No. 3

The possibility of adjusting concrete mixtures' fluidity by means of superplasticizer SNF

A. KAPELKO
Wrocław University of Technology, Wybrzeże Wyspiańskiego 27, 50-370 Wrocław

One of the disadvantages of superplasticizers' use is that the concrete mixture modified by this kind of admixtures loses its workability very quickly. This paper summarizes a current state-of-the-art effects of superplasticizer SNF addition to the cement material, in particular its mechanisms and the methods of addition. The paper presents the author's experimental investigation into the variation of concrete mixtures' fluidity in the function of time and the change of concrete technical properties as a result of superplasticizer's SNF addition. The experiments were carried out using two types of aggregates: mineral and granite, and two kinds of Portland cement: CEM I 32,5R and CEM I 42,5R. The tests have shown that SNF has a significant influence on the fluidity of cement materials. The superplasticizer added three times in the total amount of 2.0% allows us to adjust the fluidity of concrete mixtures and to keep the consistency on the fluid and half-fluid level. A faster loss of the fluidity of concrete mixtures, both a control one and modified by SNF, takes place when more cement is added and influenced by the following factors: fineness, cement mineral composition and aggregate type. The author proposes to use a parameter S_m (average slump) in order to estimate the efficiency to SNF's addition and to maintain high workability of concrete mixtures in the function of time. The modification of concrete mixtures by the superplasticizer, introduced to reduce the amount of water (reduction of the water to cement ratio), increases the compressive strength from 1 to 3 classes in comparison to compressive strength of control concrete. The modification considerably reduces the water absorption of concretes. Moreover, superplasticizer's addition increases the brittleness of concretes.

Keywords: *concrete mixtures, superplasticizer SNF, fluidity, concrete properties*

1. Introduction

A modification of cement materials by chemical admixtures has been reported in numerous monographs, journals and scientific research reports, and very often is the subject of conferences and seminars. Monographs, see, for example, Rixom [1], Ramachandran [4], Dodson [3], Neville [2], Jamroży [6], Kurdowski [7], Kapelko [8], and research reports, for example, Kucharska [5, 9], outline the different kinds of chemical admixtures, their action, their influence on the properties of fresh and hardened cement materials and finally their possibilities of practical use.

Recently, an increasing attention has been given to superplasticizers, which can be divided into five basic groups: a) sulfonated melamine-formaldehyde condensates (SMF), b) sulfonated naphthalene-formaldehyde condensates (SNF), c) modified lignosulfonate esters (MLS), and d) polycarboxylate derivatives. The most popular are the first two groups of superplasticizers, i.e, SMF and SNF.

Basically, superplasticizers added to material cements allow us: a) to reduce a *w/c* (water/cement) ratio, while maintaining an initial fluidity level of concrete mixture, or b) to maintain a constant *w/c* ratio, while keeping an initial consistency constant or increasing concrete mixture's fluidity.

Because of the plasticising effect of those admixtures, there exists the possibility that the cement content will decrease significantly without the changes in concrete's technical properties, which has been outlined by Kapelko [8, 12].

Chemical content of plasticizing admixtures, among them of superplasticizer SNF, is presented in many reports, for example, in that by Kucharska [9].

The main effects of superplasticizer on concrete properties are as follows: the dispersion of cement granules and plasticizing effect associated with this phenomenon; the adsorption of cement granules on the superplasticizer surface, which causes the repulsion of the granules; the increase in shear potential; and the stabilization of grout due to electrostatic repulsion.

Based on the literature review presented above, it can be concluded that the basic characteristics of superplasticizer's SNF performance are still a subject of ongoing investigations and further research. The method of adding SNF to the cement material, together with water, or retardation of the process is associated with numerous expected effects, for example, allows the admixture and the cement to be used in smaller amounts, keeps the fluidity level during a longer time, decreases the speed of workability loss, defines the compatibility of cement-admixture SNF and so on [3–4, 13–30, 32–34].

The analysis of the literature citied in this paper shows that there is a need for more general, careful and complex investigations into the fluidity behaviour of concrete mixtures versus time and into the changes of concrete's technical properties, taking into account concrete durability in the exposure class according to standard [36]; this concrete is enriched with triple superplasticizer SNF.

The author's research presented is aimed at broadening the knowledge about the effects of multiple superplasticizer SNF addition to the cement material on the properties of this cement, also in the aspect of its usefulness in the building practice.

2. Tests and their results

2.1. Materials

Ordinary superplasticizer SNF, i.e., a water solution of sodium salt of formaldehydic polycondesates of sulfonic-naphthalene acids, was used in the experiments. Two kinds of Portland cement were used: CEM I 32,5 R and CEM 42,5 R from the Górażdże Cement Plant. The content of tricalcium aluminate in the clinker of these cements reached 9.8 %. Based on the literature review done in the part 1 of this paper, it is known that SNF adsorbs mostly in C_3A cement's phase. Why the cement with such a high content of tricalcium aluminate was used? Because the aim of tests was to use

the total amount of SNF, that is 2.0% by weight of the cement content. This quantity of superplasticizer does not produce incidental results associated with, for example, air-entraining, which was pointed out by Kapelko [12]. In addition, it should be emphasized that the majority of cements produced in Poland are characterized by a high content of C_3A [7]. Taking into account the facts that a significant part of SNF is used during its first addition together with water and that the fast workability loss takes place, the repeated double addition of SNF in adequate amount has restored the initial fluidity of concrete mixture. It allowed us to use the whole and also the safe amount of SNF to adjust the fluidity after the workability loss through the second and the third SNF addition and to observe the speed of fluidity loss and the period when a high level of workability is kept. The possibilities of implementing the results in the building practice were being kept in mind.

The following aggregates were used in concrete mixtures: a) 8–16 mm gravel from Mietków Mine, b) 2–8 mm gravel from Mietków Mine, c) 0–2 mm sand from Mietków Mine, d) 8–16 mm basalt grit from Strzegom-Graniczna, e) 4–8 mm basalt grit from Strzegom-Graniczna. The tap water was used to make grouts.

The mineral aggregates were experimentally combined in order to obtain an optimum aggregate composition, characterized by maximum compactness and minimum amount of water absorbed by the aggregate [6, 8].

2.2. Characteristics of concrete mixtures

Six concrete mixtures were made using CEM I 32,5 R and mineral aggregate: two of them were control concrete mixtures of the consistency S1 or S2 and with the respective cement amount of 290 kg/m^3 and 350 kg/m^3, and four of them were concrete mixtures with SNF in an appropriate amount. Among concrete mixtures with SNF, an appropriate amount of admixture was added to two of them, hence the fluidity of concrete mixtures could increase significantly (keeping *w/c* constant). An appropriate amount of water was removed from two other concrete mixtures, therefore an initial consistency of concrete mixture could be sustained (a decrease in *w*/*c* value) and the amount of water removed from grouts was substituted for an appropriate amount of

Table 1. The composition and characteristics of concrete mixtures with superplasticizer SNF (CEM I 32,5 R and mineral aggregate)

Code of concrete mixture	Amount of SNF [%]	Amount of cement C [kg/m^3]	Amount of water W [kg/m^3]	Amount of aggregate K [kg/m^3]	*w*/*c*	ΔW kg, [%]	Slump [mm]	Density [kg/m^3]
C1	0.0	290	203	1917	0.700	–	45	2410
C1 A	1.0	290	203	1894	0.710	–	150	2390
C1 B	1.0	290	168	1941	0.579	35 (17.2)	20	2402
C2	0.0	350	198	1855	0.567	–	30	2403
C2 A	0.8	350	198	1855	0.576	–	170	2406
C2 B	1.2	350	164	1903	0.469	34 (17.2)	20	2421

aggregate content (gravels + sand) [8, 10–12]. The results of the quality tests on concrete mixtures are shown in Table 1.

Six concrete mixtures were made using CEM I 42,5 R, granite aggregate and mineral sand: two control mixtures of the consistency S1 or S2 and the cement amount of 320 kg/m^3 and 380 kg/m^3; additional four were modified by SNF in an appropriate amount. The SNF modifications were obtained similarly to the previous case of concrete mixtures based on mineral aggregate (Table 2).

Table 2. The composition and characteristics of concrete mixtures with superplasticizer SNF (CEM I 42,5 R and granite aggregate)

Code of concrete mixture	Amount of SNF [%]	Amount of cement C [kg/m^3]	Amount of water W [kg/m^3]	Amount of aggregate K [kg/m^3]	w/c	ΔW kg, [%]	Slump, [mm]	Density [kg/m^3]
C3	0.0	320	196	1879	0.612	–	30	2395
C3 A	1.0	320	196	1872	0.622	–	150	2391
C3 B	1.0	320	167	1912	0.522	31 (15.8)	30	2403
C4	0.0	380	204	1831	0.537	–	50	2415
C4 A	0.8	380	204	1821	0.545	–	190	2408
C4 B	1.2	380	169	1876	0.445	35 (17.2)	40	2430

2.2.1. The changes in consistency of concrete mixture versus time

The tests were carried out on eight concrete mixtures: four control mixtures (C1, C2, C3 and C4) and four modified by SNF (C1A, C2A, C3A and C4A) of initial contents outlined in Tables 1 and 2.

The control mixtures of an initial consistency S1 or S2 according to [36] were fluidised due to adding an appropriate amount of water to reach the consistency S3 or S4 according to [36] expressed by the slump, sustaining the initial content of cement. Due to such a method the values w/c of concrete mixture changed from 0.700; 0.567; 0.612 and 0.537 to 0.776; 0.663; 0.710 and 0.620, respectively.

In order to reach the same consistency as in control mixtures, the modified concrete mixtures were fluidised by adding SNF in the amount of 0.8% or 1.0% by weight of cement. Such a modification increased to a small extent the w/c value of concrete mixtures, because some amount of water was introduced through adding SNF in the form of water solution (Tables 1–2). The mixing of components took place in the laboratory concrete mixer and continued for 3 minutes. Before the consistency change was determined, the mixture was being mixed for 1 additional minute. The change in the consistency of control concrete mixtures versus time was being determined till the concrete mixture lost its fluidity, which approximated the slump of 0–20 mm.

The fluidity of concrete mixtures with superplasticizer was controlled and determined in the following way: a) the first amount of SNF was added together with water to obtain the value of fluidity at the level of the fluidity of control mixture, b) when the concrete mixture had lost its fluidity to the level of an initial consistency of control

mixture, the procedure of SNF addition was being repeated until the time the level of fluidity similar to that from the first SNF addition was obtained, c) the SNF was added for the third time when the slump of concrete mixture decreased to the level of an initial consistency of a control mixture; the change in consistency of this mixture after the third SNF addition was being determined till the time when concrete mixture lost its workability (slump of ca. 0 mm).

Together three additions contained 2% of SNF by the weight of cement. It is considered to be a safe amount of admixture, because according to the paper [12] the air-entraining of concrete mixtures modified by superplasticizer SNF does not exceed 2% [35].

Figures 1–4 show the empirical relations between the concrete mixture consistency and the time of its sustainability (slump versus time): a) for the control mixtures (C1, C2, C3 and C4) and b) for concrete mixtures with SNF (C1A, C2A, C3A and C4A), and the time difference in adding superplasticizer.

Table 3. The time when the of fluidity of concrete mixtures is sustained at the level of particular consistency classes S1 – S4

Code of concrete mixture	The time when the fluidity of concrete mixtures is sustained at the level of particular consistency class, t [min]			
	S4	S3	S2	S1
C1	0	25	120	200
C2	5	30	100	225
C3	0	15	75	240
C4	10	40	135	160
Total time t_s [min]	15	110	430	825
C1A	0	130	130	75
C2A	10	110	155	80
C3A	0	15	95	120
C4A	15	70	115	85
Total time t_{sm} [min]	25	325	495	360
Time difference, $\Delta t = t_{sm} - t_s$ [min]	10	215	65	–465

In Figures 1–4, one can find the period of time t during which the fluidity of a concrete mixture is sustained at the level of a particular class of consistency, from S1 to S4. Table 3 presents those times t for particular concrete mixtures – control and modified by SNF. In addition, this table shows the total times t_s and t_{sm} respectively for control concrete mixtures and concrete mixtures with SNF. The last row of Table 3 gives the value of the time difference: $\Delta t = t_{sm} - t_s$ for a particular class of the consistency of concrete mixtures.

Based on the relationships between the slump of concrete mixtures with superplasticizer and the time (Figures 1–4), the mean slump S_m was calculated for the time period from $t = 5$ minutes till $t = t_c$, where t_c is the time corresponding to the point of the intersection of the slump curve and the time axis. The value of S_m is a proportion of

surface between the curves to the time period, ranging from t_c = 5 minutes to the period length t_c – 5 minutes.

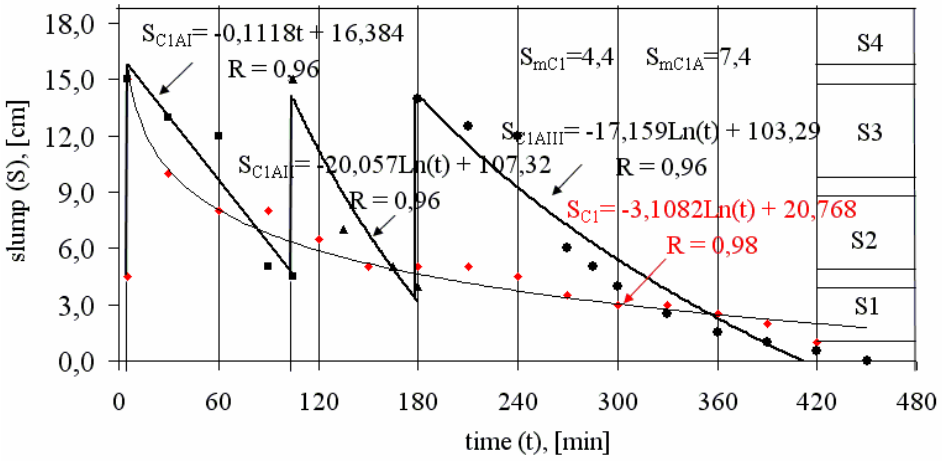

Fig. 1. Correlation relationship between the consistency of concrete mixtures (slump *S* [cm]) and the time *t* [min]: control concrete mixture (C1) and concrete mixture with superplasticizer SNF (C1A)

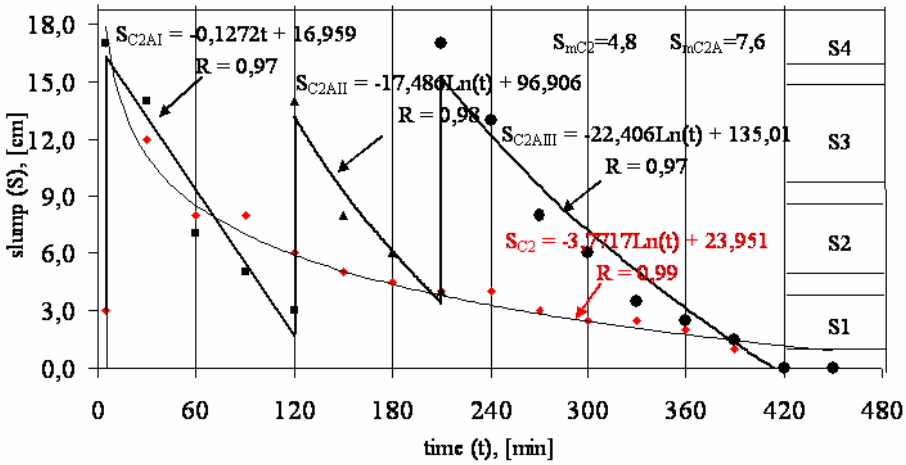

Fig. 2. Correlation relationship between the consistency of concrete mixtures (slump *S* [cm]) and the time *t* [min]: control concrete mixture (C2) and concrete mixture with superplasticizer SNF (C2A)

In the case of the control concrete mixtures, the values of S_m were calculated for the same time period as in the case of modified concrete mixtures (5 minutes, t_c). Figures 1–4 present the values of mean slump S_m of concrete mixtures presented in Tables 1 and 2.

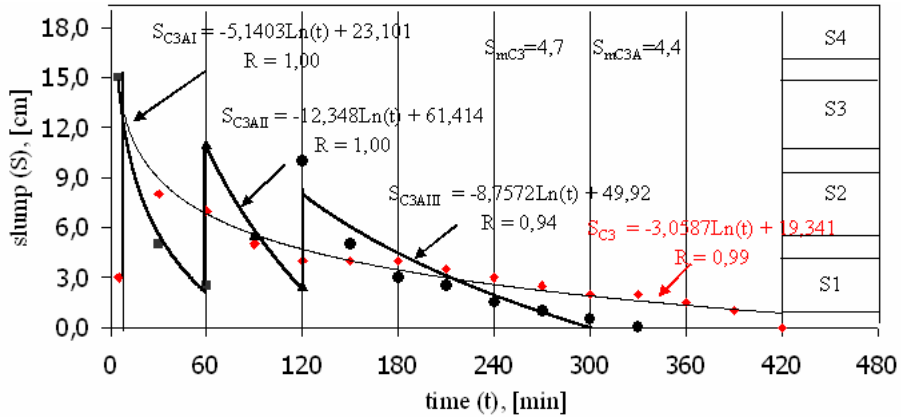

Fig. 3. Correlation relationship between the consistency of concrete mixtures (slump *S* [cm]) and the time *t* [min]: control concrete mixture (C3) and concrete mixture with superplasticizer SNF (C3A)

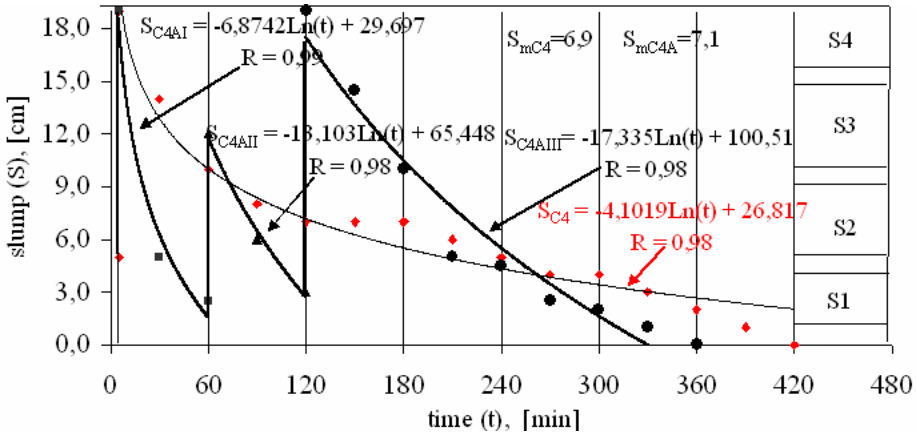

Fig. 4. Correlation relationship between the consistency of concrete mixtures (slump *S* [cm]) and the time *t* [min]: control concrete mixture (C4) and concrete mixture with superplasticizer SNF (C4A)

2.3. Characteristics of concretes

The following properties of concretes outlined in Tables 1 and 2 were determined: compressive strength, tensile splitting strength and water absorption after 28 days of hardening in the laboratory conditions. The specimens used for all determinations were cured in a climatic chamber at a temperature of 18 °C (±2 °C) and a relative air humidity of 95% (±5 °C). For each type of concrete the compressive strength was determined using 6 cube specimens with a 150 mm side [36]. The average compressive strength values are shown in Figures 5 and 6. In addition, the dispersion of results in the form of standard deviation was calculated. The results obtained are given in Figures 5 and 6. Compressive strength classes for concretes after 28 days of hardening, determined according to European Standard [36], are given in Figures 5 and 6.

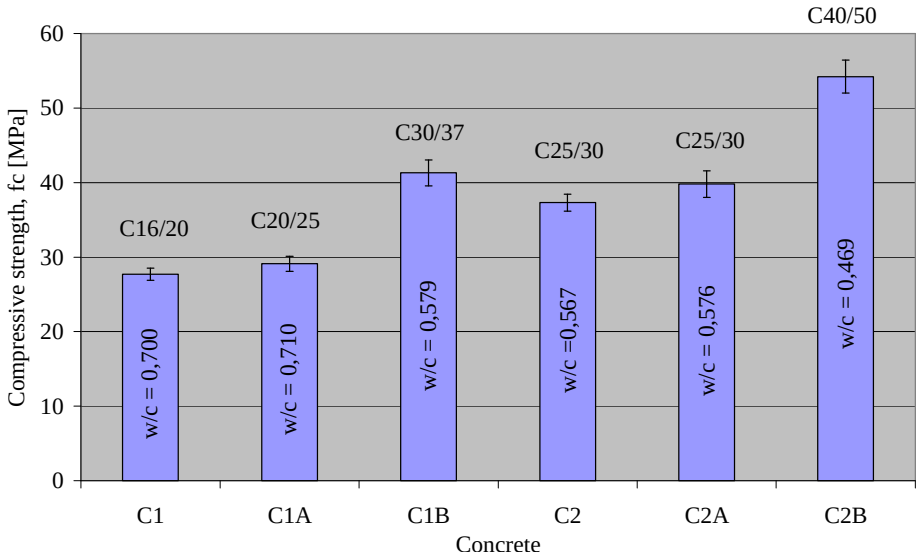

Fig. 5. Compressive strength of concrete mixtures based on mineral aggregate

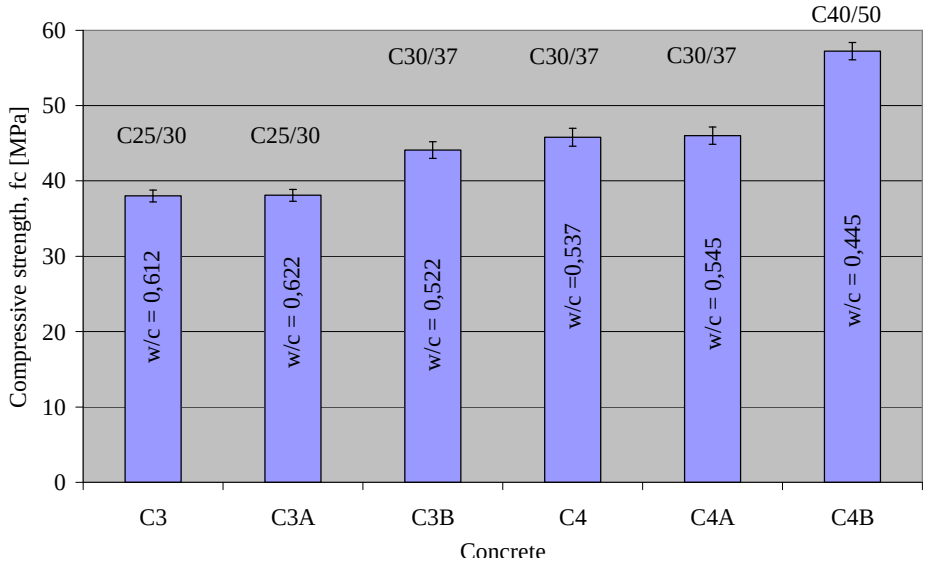

Fig. 6. Compressive strength of concrete mixtures based on granite aggregate

For each type of concrete, a tensile splitting strength was determined using 6 cube specimens with a 160 mm diameter and height (Brazilian method) [6, 8]. Based on the values of the mean tensile splitting strength f_{tm} and the mean compressive strength f_{cm}, the values of concrete brittleness were calculated. The material brittleness k is defined as a ratio of the mean tensile splitting strength of concrete f_{tm} to the mean compressive

strength of concrete f_{cm}. Materials are considered to be brittle, when their $f_{tm}/f_{cm} \leq 0.125$. The lower the ratio k, the more brittle the material. The calculated values of brittleness for different types of concretes presented in Tables 1 and 2 are given in Figure 7.

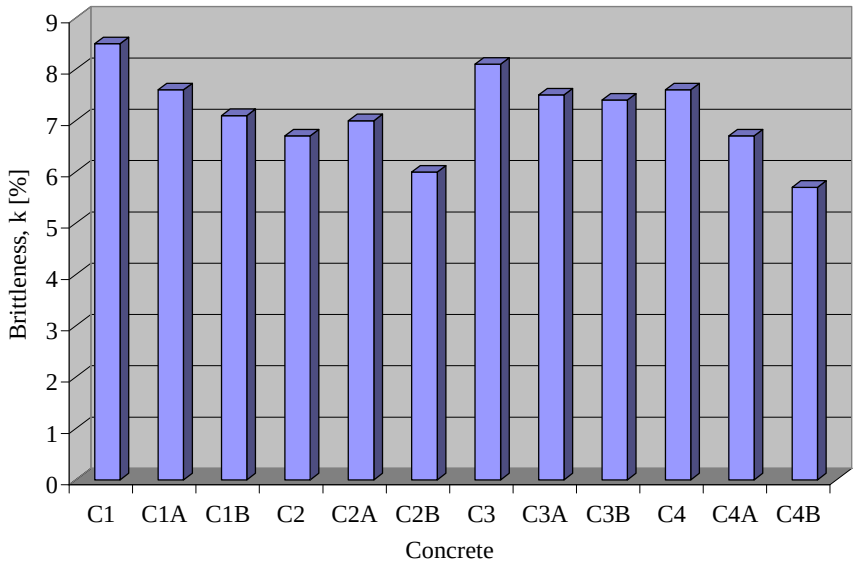

Fig. 7. Brittleness of concrete

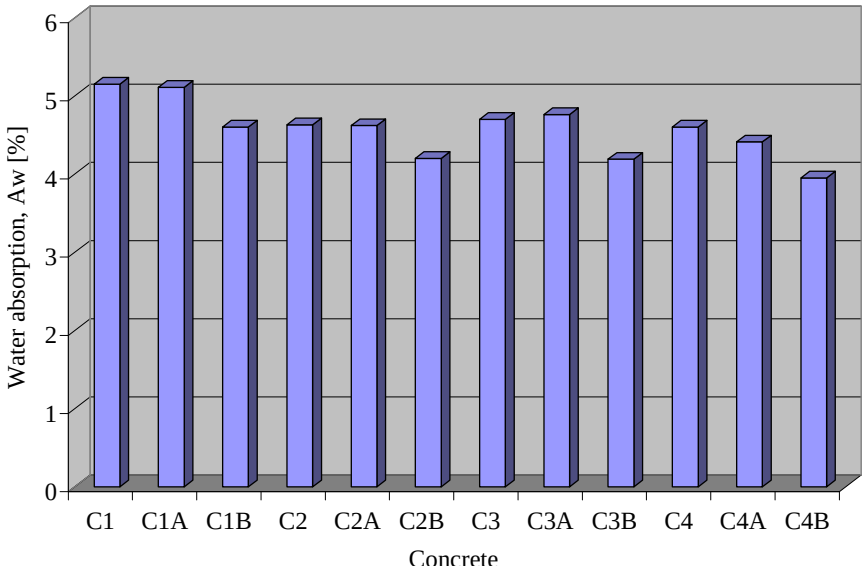

Fig. 8. Water absorption by concrete

Further, the water absorption was determined using cube specimens with a 100 mm side, five for each type of concrete. The water absorption by concretes with characteristics presented in Tables 4 and 5 is given in Figure 8.

3. Discussion of the test results

In concrete mixtures containing mineral and granite aggregates with SNF addition in the amount of 1.0–1.2% by weight of the cement content, it is possible to reduce the amount of water by 15 to 17%, while keeping the initial consistency S1 or S2, according to [43] (Tables 1–2). Through water removal, the *w*/*c* ratio of concrete mixtures decreases significantly, for example, for concretes C1, C2, C1B and C2B (Table 1), *w*/*c* ratios equal to 0.700, 0.567, 0.579 and 0.469, respectively. Similar changes were observed in concretes made from granite aggregate and CEM I 42,5 R (Table 2). More effective is SNF addition to concrete mixtures containing larger amount of cement (Tables 1–2). In the case where concrete mixtures were made from two types of aggregates, different amount of cement characterized by two strength classes and appropriate amount of superplasticizer, the investigations into concrete mixture workability versus time show that it is possible to adjust the fluidity of concrete mixture during different time periods, depending on the technological demands. Triple SNF addition in the total amount of 2.0% by weight of cement content allows the consistency to be kept on a high level of fluidity (high slump) according to its standard ranging from S1 to S4 [36]. The periods of workability persistence at the level of consistency S4 for control concrete mixtures and concrete with SNF admixture are very similar and last to 15 and 25 minutes, respectively. The period of fluidity persistence of four control mixtures at the level of consistency S3 lasts 110 minutes. On the other hand, when those mixtures are modified with triple SNF addition, this period is as long as 325 minutes being by 215 minutes (3h 35') longer than that typical of control concrete mixtures. In addition, the difference between the periods of workability persistence, at the level of consistency S2, of control concrete mixtures and concrete with SNF admixture reaches 65 minutes. The workability is kept longer in the case of control concrete mixtures (Table 3).

The SNF effectiveness with respect to its counteraction against setting cement granules is kept as long as admixture particles are able to create a protection film on the cement surface. Some SNF particles are being adsorbed on the hydration products and then superplasticizer access to cement is not sufficient, which, in turn, results in its workability worsening. The hydratation products and an ongoing process of hydratation reduce the fluidity of concrete mixtures. As was mentioned before, the SNF was being added to mixtures together with the whole amount of water. Superplasticizer was being adsorbed mainly on the dehydrated layers of C_3A and C_4AF [2–7, 9]. Because cement contained relatively high per cent of such phases as C_3A, 9.8%; C_4AF, 8.2%; C_3A/C_4AF, 1.2% and alkalies, 0.8%, the amount of SNF being used for mixture fluidising was smaller than that added one minute after basics components

were being mixed [9]. During this period, an intensive and also short reaction between water and C_3A and gypsum proceeds, ettringit is formed, which adsorbs SNF to much lower degree than C_3A. Ca^{2+} and SO_4^{2-} ions and alkalies are being transported to the solution and the process of their loosening is activated by superplasticizer [2–7, 9]. Because of this effect, a further ettringit formation is retarded. During this process a considerable amount of water is used [7]. Because in our experiments the Portland cements characterized by the properties presented in Tables 1 and 2 were being used, the workability loss observed after the first and the second SNF addition was faster in comparison to the workability loss after the third superplasticizer addition. The fact that an initial workability was kept for a long time, after being reproduced through the third superplasticizer addition, could be explained by its significant retardation when cement initiates its setting, when SNF is added in the amount of 2.0% by weight of cement [12].

When making the comparison between the workability loss of control concrete mixtures and concrete modified by SNF (after single SNF addition), both having the same slump (Figures 1–2), it can be concluded that the workability within the period of 60 minutes is lost more quickly in control mixtures. On the other hand, in concrete mixtures with mineral aggregate and CEM I 32,5 R without admixture, but with triple SNF dosage, the workability loss up to the level of 0–20 mm measured with slump occurs almost at the same time (7 h).

A workability loss observed in the case of concrete mixtures prepared with CEM I 42,5 R is higher than that for concrete with CEM I 32,5 R (Figures 1–4). This is associated mainly with the specific surface of those binders and the cement fraction in concrete mixtures.

The concrete mixtures made from cement CEM I 32,5R and mineral aggregate and from cement CEM I 42,4R and granite aggregate are characterized by similar periods of fluidity persistence at respective consistency levels: a) S3 – 55 and 55 minutes, b) S2 – 120 and 110 minutes and c) S1 – 425 and 400 minutes. Concrete mixtures made from granite aggregate lose their fluidity slightly quicker in comparison to concrete mixtures from mineral aggregate which is associated with the impact of these aggregate on workability worsening [2–3]. The periods of consistency persistence depend also on the amount of Portland cement: if larger amount of binder is used, those periods are becoming longer for the mixtures made from granite aggregate and shorter for the mixtures from mineral aggregate (Table 3 and Figures 1–4).

The values of the parameter S_m calculated for concrete mixtures made from mineral aggregate and modified with SNF (C1A and C2A) are respectively by 67 and 59% higher compared to these for control mixtures (C1 and C2). On the other hand, for control concrete mixtures (C3 and C4) and concrete with the fraction of SNF (C3A and C4A) prepared with granite aggregate, the values of average slump are very similar (Figures 1–4).

In the author's opinion, independently of the workability loss after sequential superplasticizer SNF addition, we can use the parameter S_m for estimating the effective-

ness of multiple SNF dosage with respect to a high level of concrete mixtures' fluidity versus time: a) when this parameter reaches similar values for control mixtures and those with SNF, the modification by superplasticizer can be treated as not very effective, which is the case of concrete mixtures made from granite aggregate (Figures 3–4 and Table 3), b) when the values of the parameter S_m are significantly higher for concrete mixtures with superplasticizer in comparison to these for control concrete mixtures, the modification with superplasticizer can be treated as effective, which has been proved by the investigations carried out with mineral aggregate (Figures 1–2 and Table 3).

Double and sequential superplasticizer addition to concrete mixtures containing granite aggregate should be made more precisely, better directly before building in and the process of consolidation in the construction.

The results of compressive strength determination (Figures 5 and 6) testify to a significant SNF influence on the compressive strength after 28 days of hardening. Because of water reduction through plasticising effect of admixtures and sustaining the control consistency, the concretes' compressive strength increases (C1B, C2B, C3B and C4B) in comparison to strength of control concrete (C1, C2, C3 and C4). The control concretes reached, according to standard [36], compressive strength classes: C16/20≈C20/25, C25/30, C25/30≈C30/37 and C30/37, respectively, while modified concretes obtained much higher classes: C30/37, C40/50, C30/37 and C40/50, respectively. A high increase observed in compressive strength of concretes with SNF is associated mainly with *w*/*c* reduction (Tables 1, 2). Single SNF dosage in appropriate amount (Tables 1, 2) in order to fluidize concrete mixtures increases *w*/*c* to a small degree in comparison to control mixtures and results in compressive strength resistance at the same level both for modified and control concretes (Figures 5, 6). The compressive strength of concretes made from concrete mixtures diluted with water and with the same slump as that of mixtures fluidised with appropriate amount of SNF was not determined. Control concrete mixtures were useful only for estimating the SNF impact on workability changes in the function of time. It is obvious that control concretes made from concrete mixtures characterized by very high *w*/*c* ratio will have low technical parameters, but concretes with superplasticizer have lower *w/c* ratio and therefore much higher compressive strength.

SNF added to concrete mixtures in order to fluidize them and to reduce the amount of water increases brittleness of concrete (Figure 7). A bigger influence of superplasticizer on the brittleness of concrete was observed in concretes made from concrete mixtures with the reduced amount of water and the consistency of control concrete mixtures. Moreover, it was found that brittleness of concrete after 28 days of hardening in laboratory conditions was more effective when granite aggregate was used than when mineral aggregate was added [2].

The water absorption of control concretes and concretes modified by SNF is similar (Figure 8). If superplasticizer is introduced into concrete mixtures simultaneously with the removal of an appropriate amount of water, which preserves their initial con-

sistency, the water absorption A_W decreases by 9 to 14% relative to the water absorption of nonmodifical concrete mixtures (Tables 1–2). This is mainly due to a reduction of the mixtures' *w/c* brought about by adding superplasticizer. According to standard [35], the water absorption by concrete should not be higher than: a) 5% for concretes exposed to environmental action, b) 9% for concretes protected against environmental action.

Analysed concretes based on mineral and granite aggregates with cement content of 320–380 kg/m^3 satisfy standard requirements [35] with regard to water absorption and both types of conditions. Of concretes whose cement content is 290 kg/m^3 and which are based on mineral aggregate, only concrete C1B with reduced amount of water (decrease in *w*/*c* ratio caused by superplasticizer addition) meets standard requirements [35]. These results are of great importance for concrete used in water conditions and temperature variability [36].

Collepardi [30] summarizes the research in the field of superplasticizers SNF, SMF and based on polycarboxylates PC. He describes the influence of material and technological factors on the rate of slump loss and analyses the progress in slump retention on an adequate level. As the author of this paper, also Collepardi [30] indicates many problems associated with the usage of different superplasticizers. Slump loss is one of the most serious problems for ready-mixed concrete industries. When a concrete mix must be transported for a long time, an initial slump level should be kept to avoid the redosing of concrete with the water content above and below that required for the mix design. However, slump loss cannot be avoided because of the intrinsic requirement for cement mixes which should set and harden in a relatively short time. Therefore, a right and proper solution would be a zero-slump-loss concrete mix for about one hour. By using superplasticizers based on SNF or SMF polymers it is not easy to achieve this target, because in general slump loss is greater in superplasticized concrete with respect to the corresponding plain mix at given initial slump. The cement content as well as the chemical and mineralogical composition of cement play an important role in determining such a singular slump loss although the detailed mechanism is not clear: it seems that the content of C_3A, gypsum and alkalies as well as the form of calcium sulfate used as set regulator can affect the rate of slump loss. On the other hand, PC-based superplasticizer acts as both an immediate superplasticizer and a slump loss reducing agent, and appears to be more effective than that based on SNF.

4. Summary

From the tests carried out on material cement with superplasticizer SNF the following conclusions can be drawn:

1. SNF introduction to concrete mixtures based on mineral and granite aggregates in the amount of 1.0–1.2 % by weight of the cement content allows us to reduce water content by 16 to 17 % while sustaining the consistency of control concrete mixture.

2. Triple superplasticizer addition allows us to adjust significantly the concrete mixtures' fluidity and to preserve the consistency at the level of S3 and S2 for 240 and 285 minutes when mineral aggregate and CEM I 32,5R are used, and for 85 and 220 minutes when granite aggregate and CEM I 42,5R are used. The time when consistencies S3 and S2 are sustained in control concrete mixtures is 55 and 220 minutes and 55 and 210 minutes, respectively. Especially long time of fluidity preservation is observed for the concrete mixtures with SNF at the consistency level S3 (slump from 110 to 150 mm). The quicker fluidity loss was found for concrete mixtures not modified and modified by superplasticizer SNF, made from mineral and granite aggregates and containing greater amount of cement, i.e., 350 and 380 kg/m^3, in comparison to concrete mixtures with cement content of 290 and 320 kg/m^3, respectively. The quicker workability loss of concrete mixtures with SNF after its first and second dosage is associated mainly with relatively high content of C_3A and C_4AF phases and alkalies. Therefore, the slower fluidity loss of concrete mixtures modified by superplasticizer SNF can be expected to occur when cements with low content of C_3A and C_4AF are used or when admixture is added with certain retardation, for example, one minute after initialising the process of mixing basic components [1–2, 5, 6, 9]. After the third SNF addition the workability of concrete mixtures is sustained for longer, which is associated with the fact that superplasticizer retards the setting time of Portland cements. The superplasticizer should be added more precisely, better directly before in building and the process of consolidation in the construction.

The straight lines and logarithmic curves are a good representation of the relationship between mixture consistency and the time at a correlation coefficient of 0.94–1.00. The author proposes to use the parameter S_m – an average slump – as the estimation of multiple SNF dosage's effectiveness with respect to the high level of concrete mixtures' fluidity in the function of time.

3. It is recommended to produce the concrete mixtures with a reduced cement content in 1 m^3 of the mixture to minimize the unfavourable influence of increased C_3A content on quicker slump loss. It can be obtained through the substitution of certain amount of cement for fly ash, which is highlighted in standard [36]. It is obvious that such a treatment, which on the one hand increases concrete mixtures workability, on the other one, cannot decrease the technical parameters which have to be sustained when material is exploited in engineering constructions.

4. In modern ready-mixed concrete plants, it is possible to use superplasticizers SNF which allows certain retardation after mixing basic components. In author's opinion the time of superplasticizer addition should be determined in previous experiments in consistency versus time, while taking into account mainly: a) the content of phases C_3A, C_4AF, alkalies and gypsum in cement, b) the amount of cement in 1 m^3 of concrete, the type of aggregate (working recipe) and the value of *w*/*c* ratio, c) expected time of concrete mixture's transportation to building place, depending on environment temperature, d) the possibility of adding SNF in an appropriate amount to the concrete in truck concrete mixer, which allows fluidisation of concrete mixture, sus-

taining it at this level during the period of its supply and consolidation in construction. It is also necessary to compare economical effectiveness of production cost of 1 m^3 of concrete to ensure the assumed level of concrete mixture's workability during engineering construction forming.

5. Superplasticizer added to concrete mixtures in order to fluidize them does not influence the water absorption. SNF addition and at the same time water reduction in concrete mixtures and sustainability of the initial consistency level decrease water absorption by concrete by 9 to 14% relative to control concrete mixtures. The decrease of water absorption can significantly change the type of concrete exploitation, depending on the exposure classes to environmental actions: atmospheric conditions and changeable temperatures.

6. The modification of concrete mixtures by superplasticizer allows us to reduce the amount of mixing water and to decreases significantly *w*/*c* ratio, which in turn improves the compressive strength after 28 days of hardening in comparison to control concretes: a) when mineral aggregate and CEM I 32,5 R are used by 45 to 49%, b) when granite aggregate and CEM I 42,5 R are used – by 16 to 25%. As a result of *w*/*c* decrease in concrete mixtures with SNF, the compressive strength after 28 days of hardening increases significantly in comparison to strength of control concretes. The compressive strength of modified concretes is from 1 to 3 compressive strength classes higher than that of concretes without SNF. The addition of superplasticizer SNF in the amount of 0.8–1.0% by weight of cement which is responsible for concrete mixture fluidisation, with small *w*/*c* change, allows us to sustain the compressive strength after 28 days of hardening at the level of control concrete strength.

7. The SNF addition to concrete mixtures in order to fluidize them and make them water safe increases the brittleness of concrete; however, bigger influence is observed in concretes containing a smaller amount of water.

References

[1] Rixom M. R., Mailvaganam N.: *Chemical Admixtures for Concrete*, E & F. N. Spon, London/New York, 1986.
[2] Neville A. M.: *Properties of Concrete*, Polish Cement, Kraków, 2000.
[3] Dodson V.: *Concrete Admixtures*, Van Nostrand Reinhold, New York, 1990.
[4] Ramachandran V.S.: *Concrete Admixtures Handbook: Properties, Science and Technology*, Noyes Publications, New Jersey, 1984.
[5] Kucharska M.: *Plasticizers in Concrete Technology – Examples of Application*, Proceedings of the Conference *The Concrete before Millennium*, Kraków, 9–10 of November 2000, pp. 55–72.
[6] Jamroży Z.: *Concrete and its Technologies*, PWN, Warszawa–Kraków, 2000.
[7] Kurdowski W.: *Cement Chemistry*, PWN, Warszawa, 1991.
[8] Kapelko A.: *Technical and Economic Conditions of Cement Substances Modification with Chosen Chemical Admixtures*, Monograph 26, Wrocław University of Technology, 1992.

[9] Kucharska L.: *Traditional and modern concrete admixtures decreasing amount of mixing water*, Cement–Lime–Concrete, 2000, 2, pp. 46–61.
[10] Kapelko A.: *Properties of cement product modified with calcium gluconate*, Cement-Lime–Concrete, 1998, No. 3, pp. 99–103.
[11] Kapelko, A.: *The effect of a new set-retarding superplasticizer on the properties of cement-based materials*, Cement–Lime–Concrete, 1999, 3, pp. 75–80.
[12] Kapelko A.: *Possibilities of cement content reduction in concretes with admixture of superplasticizer SNF*, Journal of Civil Engineering and Management, June 2006, Vol. XII, No. 2, Vilnius, pp. 117–126.
[13] Termkhajornkit P., Nawa T.: *The fluidity of fly ash–cement paste containing napthalene sulfonate superplasticizer*, Cement and Concrete Rasearch, 2004, 34, pp. 1017–1024.
[14] Chandra S., Björnström J.: *Influence of cement and superplasticizers type and dosage on the fluidity of cement mortars.* Part I, Cement and Concrete Research, 2002, 32, pp. 1605–1611.
[15] Chandra S., Björnström J.: *Influence of cement and superplasticizers type and dosage on the fluidity of cement mortars.* Part II, Cement and Concrete Research, 2002, 32, pp. 1613–1619.
[16] Uchikawa H., Hanehara S., Sawaki D.: *The role of steric repulsive force in the dispersion of cement particles in fresh paste prepared with organic admixtures*, Cement and Concrete Research, 1997, 27, 37.
[17] Chiocchio G., Paolini A.E.: *Optimum time for adding superplaticizers to Portland cement pastes*, Cement and Concrete Research, 1985, 15, 901.
[18] Bonem D., Sarkar S.: *The superplasticizer adsorption capacity of cement pastes pore composites, and parameters affecting flow loss*, Cement and Concrete Research, 1995, 25, 7, 1423.
[19] Uchikawa H., Sawaki D., Hanehara S.: *Influence of kind and added timing of organic admixure on the composition, structure and property of fresh cement paste*, Cement and Concrete Research, 1995, 25, 2, 353.
[20] Kucharska L., Moczko M.: *Influence of cement chemical composition on its response to superplasticizers addition in light of rheological test*, Proceedings of Interuniversity Research Seminar, Eindhoven University of Technology, 1992, 135.
[21] Aïtcin P.C., Jolicoeur C., MacGregor J.G.: *A look at certain characteristics of superplasticizers and their use in the industry*, Concrete International, 1994, 16(15), pp. 45–52.
[22] Uchikawa H., Sawaki D., Hanehara S.: *Influence of kind and added timing of organic admixture on the composition, structure and property of fresh cement paste*, Cement and Concrete Research, 1995, 25, pp. 353–364.
[23] Aïtcin P.C., Saarkar S.L., Regourd M., Volant D.: *Retardation effect of superplaticizer on different cement fractions*, Cement and Concrete Research, 1987, 17(6), pp. 995–999.
[24] Uchikawa H., Hanehara S., Sawaki D.: *The role of steric repulsive force in the dispersion of cement particles in fresh paste prepared with organic admixture*, Cement and Concrete Research, 1997, 27, pp. 37–50.
[25] Erdogdu S.: *Compatibility of superplasticizer with cement different in composition*, Cement and Concrete Research, 2000, 30, pp. 768–773.
[26] Papo A., Piani L.: *Effect of various superplasticizers on the rheological properties of Portland cement pastes*, Cement and Concrete Research, 2004, 34, pp. 2097–2101.

[27] Fukuda M., Mizunuma T., Izumi T., Lizuka M.: *Slump Control and Properties of Concrete with New Superplasticizer*, I. *Laboratory Study and Test Method*, Proc. Intern. RILEM Symposium on Admixtures for Concrete, 10, E. Vasques. Chapman and Hall, London, 1990.
[28] Jiang S., Kim B.K., Aïtcin P.: *Importance of adequate soluble alkali content to ensure cement/superplasticizer compatibility*, Cement and Concrete Research, 1999, 29, 71.
[29] Khatib J.M., Mangat P.S.: *Influence of superplasticizer and curing on porosity and pore structure of cement paste*, Cement and Concrete Composites, 1999, 21, pp. 431–437.
[30] Collepardi M.: *Chemical Admixtures Today*, Proceedings of Second International Symposium on Concrete Technology for Sustainable, Development with Emphasis on Infrastructure, Hyderabad, India, 27 February–3 March 2005, pp. 527–541.
[31] Kapelko A.: *Special concretes for carrying out pit shafts linings in copper ore mines*, Cement – Lime – Gypsum, 1994, 1, pp. 11–17.
[32] Hsu K.C., Chiu J.J., Chen S.D., Tseng Y.C.: *Effect of addition time of a superplasticizer on cement adsorption and on concrete workability*, Cement and Concrete Composites, 1999, 21, pp. 425–430.
[33] Papayianni I., Tsohos G., Oikonomou N., Mavria P.: *Influence of superplasticizer type and mix design parameters on the performance of them in concrete mixtures*, Cement and Concrete Composites, 2005, 27, pp. 217–222.
[34] Agarwal S.K., Masood I., Malhotra S.K.: *Compatibility of superplasticizers with different cements*, Construction and Building Materials, 2000, 14, pp. 253–259.
[35] PN-88/B-06250 Ordinary concrete.
[36] EN 206-1:2000 Concrete – Part 1: Specification, performance, production and conformity.

Możliwości regulacji ciekłości mieszanek betonowych przez zastosowanie superplastyfikatora SNF

Jedną z wad superplastyfiaktorów jest szybka utrata urabialności mieszanek betonowych modyfikowanych domieszkami tego rodzaju. Przedstawiono stan wiedzy w zakresie efektów związanych z mechanizmem i sposobem wprowadzenia superplastyfikatora SNF do tworzyw cementowych. W pracy opisano badania własne autora, który zajmował się ciekłością mieszanek betonowych w funkcji czasu oraz zmianą właściwości technicznych betonu podczas 3-krotnego dozowania superplastyfikatora typu SNF. Eksperymenty przeprowadzono dla dwóch rodzajów kruszyw: mineralnego i granitowego oraz cementów portlandzkich CEM I 32,5 R i CEM I 42,5 R. Opierając się na wynikach badań, stwierdzono istotny wpływ SNF na uplastycznienie tworzyw cementowych. Dodanie superplastyfikatora w trzech porcjach o łącznej ilości 2.0% pozwala regulować ciekłość mieszanek betonowych i utrzymywać ją na poziomie konsystencji ciekłej i półciekłej. Mieszanki betonowe kontrolne i modyfikowane SNF szybciej przestają być ciekłe, gdy zawierają więcej cementu, co jest związane z miałkością, składem mineralogicznym cementu oraz rodzajem kruszyw.

Autor proponuje wykorzystać parametr S_m (średni opad stożka) w ocenie efektywności dodawania superplastyfikatora SNF i zachowania wysokiej urabialności mieszanek betonowych w funkcji czasu. Modyfikacja mieszanek betonowych superplastyfikatorem, aby obniżyć w nich zawartość wody (zmniejszyć *w*/*c*), podwyższa ich wytrzymałość na ściskanie od 1 do 3 klas w porównaniu z wytrzymałością betonów kontrolnych. Ta modyfikacja istotnie obniża nasiąkliwość betonów. Dodanie superplastyfikatora zwiększa kruchość betonów.

ARCHIVES OF CIVIL AND MECHANICAL ENGINEERING

Vol. VI 2006 No. 3

Kinematics and dynamics of some selected two-wheeled mobile robots

S. NOGA
Rzeszów University of Technology, ul. Wincentego Pola 2, 35-959 Rzeszów

In this paper, the problem of the kinematics and dynamics of two constructional conceptions of a two-wheeled mobile robot is considered. The wheeled mobile robot subjected to nonholonomic constraints moves over the inclined plane. Its trajectory consisting of the straight line and the curvilinear path described by the sinusoidal function is analyzed. The kinematic equations for arbitrarily chosen point of the system are derived by using classical equations of mechanics. Kinematic and dynamic parameters of motion from the solution of inverse kinematic and dynamic problem are obtained. Simulation results are presented to illustrate the efficiency of the approach.

Keywords: *mobile robot, nonholonomic constraints, kinematic and dynamic modelling, Lagrange's equations*

1. Introduction

The problems concerning kinematics, dynamics and control of wheeled mobile robots gain more and more attention. This results mainly from the fact that wheeled mobile robots are very often used in industry, especially where the contribution of an operator to some technological processes is not recommended. The mobile robot under investigation is a system which rolls on conventional wheels and is subjected to nonholonomic constrains. Fundamental theory of nonholonomic systems is developed in a number of monographs by, for example, Gutowski [1], Nejmark and Fufajev [2]. The kinematic modelling of mobile robots is investigated by many researchers. The problem of the kinematics of a two-wheeled mobile robot is analyzed in [3–6, 8–10]. In [6, 8, 9], a natural orthogonal complement is applied to a wheeled mobile robot. The problem of motion of the mobile robot along the curvilinear trajectory is discussed in the paper [10], excluding the kinematics of bracket and caster wheel. In papers [3, 4], the kinematics of this system using classical equations of mechanics is described, including the kinematics of bracket and caster wheel. The problem of the dynamics of a mobile robot is considered in papers [4, 6, 8, 11]. In papers [6, 8], a natural orthogonal complement is applied to a wheeled mobile robot. The problem of neural modelling of the mobile robot is discussed in paper [11], excluding the dynamics of a bracket and a caster wheel. In paper [4], the dynamics of this system using classical equations of mechanics is described. This paper continues the recent author's investigations concerning the kinematics and dynamics of mobile robots [3–5, 10, 11].

The present paper is organized as follows. Section two describes the mobile robot system under study. In sections three and four, the kinematics of a two-wheeled mobile robot is studied. In section five, the dynamics of the mobile robot is analyzed. Section six presents some simulation results, and section seven gives some concluding remarks.

2. Model of the system

An assumed model of the mobile robot is presented in Figure 1. The basic units of the model are as follows: frame 4, driving and steering wheels 1 and 2, and bracket with caster wheel 3. Wheels 1 and 2, mounted on the shafts, are driven separately by two electric motors. Wheels rotate about their axes, whose positions are invariable in relation to the frame. The third wheel is mounted on a rotary bracket. In the modelling of the mobile robot system, the following assumptions are adopted:

- There is no slipping between the wheel and the floor, i.e., rolling contact is maintained.
- The vehicle cannot move sideways to maintain the nonholonomic constraint.
- The motion of the mobile robot is confined to the plane *xy*.

Paper [7] presents the specifications and controls of the mobile robot shown below.

The coordinates α_1, α_2, and α_3 are the angles of rotation of wheels 1, 2, and 3, respectively. The angle of rotation of the formative wheel 1z is denoted by α. The angle β is the angle of instantaneous angular displacement of frame 4.

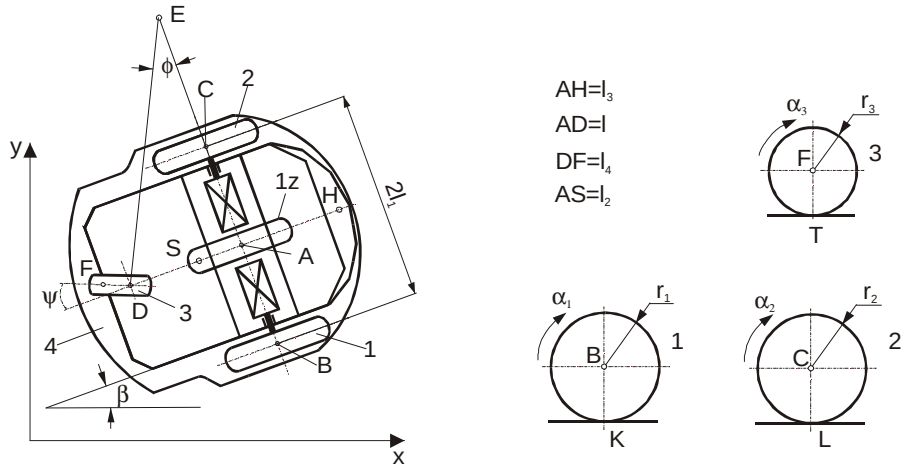

Fig. 1. The two-wheeled mobile robot

The angle ψ is the angle between the longitudinal symmetry axis of the chassis and the bracket. The following elements: l, l_1, l_2, l_3, l_4 are the lengths, and r_1, r_2,

r_3 are the radii defined in Figure 1. The radius r is the radius of the formative wheel 1z . The point *A* is a characteristic point of the frame and the point of intersection of the frame longitudinal symmetry axis with the axis of rotation of wheels 1 and 2. The points *B*, *C*, and *F* are the centres of masses of wheels 1, 2, and 3, respectively. The point *S* is the centre of mass of chassis 4. The point *D* is the connection point of bracket 3 and frame 4.

The position and orientation of the mobile robot are described by seven coordinates: x_A, y_A – the Cartesian coordinates of the point *A*; α_1, α_2, α_3, β, ψ – the angle coordinates.

The mobile robot constitutes a nonholonomic planar system. If no slipping and no sideway motions are assumed, the mobile robot has two degrees of freedom only. One can choose the angles of driving wheels as generalized coordinates for the convenience of control design. The objective of the kinematic analysis of the mobile robot is to derive the kinematic parameters of the system in terms of generalized coordinates.

In the present paper, two conceptions of the constructional schemes of this kind of robot are analyzed. When the centre *S* of mass is situated behind the axis of wheels 1 and 2 (see Figure 2a), we deal with the so-called dragging system [4]. When the point *S* is situated before the axis of wheels 1 and 2 (see Figure 2b), we deal with the so-called propelling system [4].

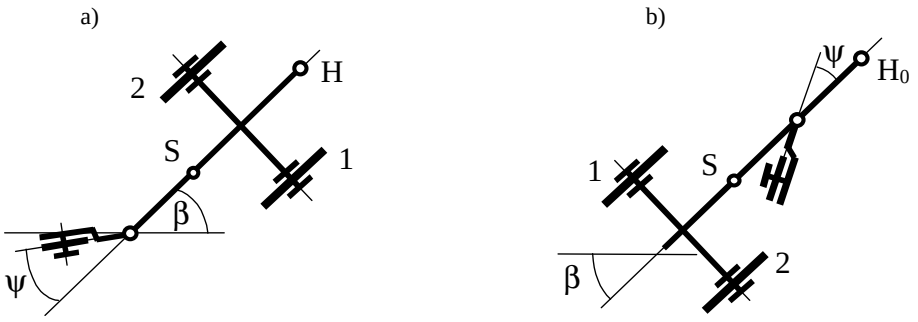

Fig. 2. Schematic diagrams of the two-wheeled mobile robot

3. Kinematics of the dragging system

The robot under consideration is moved on the plane. The chassis and the bracket with the caster wheel undergo planar motion. The velocity distribution of characteristic points of the system is displayed in Figure 3.

The point *E* is an instantaneous centre of chassis 4, and the point *G* is the instantaneous centre of the bracket.

According to the nonholonomic constraints and nonslipping condition, the robot has to move in the direction of the symmetry axis, i.e.:

$$\dot{x}_A = v_A \cos\beta, \qquad \dot{y}_A = v_A \sin\beta, \tag{1}$$

where v_A is the velocity of the point *A*. Likewise, the bracket has to move in the direction of the symmetry axis, i.e.:

$$\dot{x}_F = v_F \cos(\beta - \psi), \qquad \dot{y}_F = v_F \sin(\beta - \psi), \tag{2}$$

where v_F is the velocity of the point *F* (see Figures 1 and 3), and (x_F, y_F) are the coordinates of the point *F* given directly by:

$$x_F = x_A - l\cos\beta - l_4 \cos(\beta - \psi), \qquad y_F = y_A - l\sin\beta - l_4 \sin(\beta - \psi). \tag{3}$$

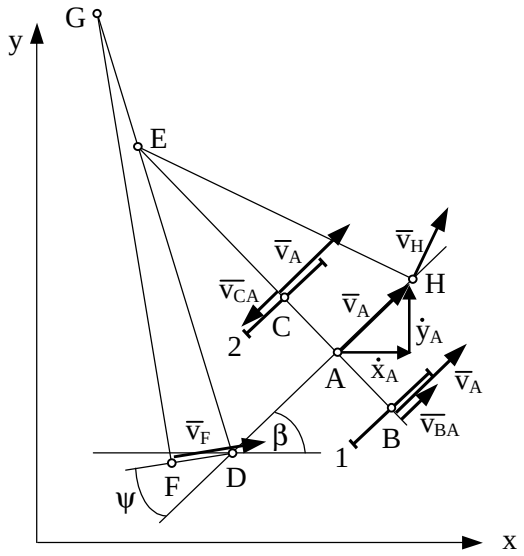

Fig. 3. The velocity distribution of the system

From Equations (1) – (3), the angular velocity of the bracket with respect to the chassis is determined [4]:

$$\dot{\psi} = \frac{1}{l_4}\left[\dot{\beta}\left(l\cos\psi + l_4\right) - v_A \sin\psi\right]. \tag{4}$$

Taking into account kinematic equations for the points *B*, *C*, and *F*, the angular velocities of wheels 1, 2, and 3 are given by [4]:

$$\dot{\alpha}_1 = \frac{v_A}{r} + \dot{\beta}\frac{l_1}{r}, \qquad \dot{\alpha}_2 = \frac{v_A}{r} - \dot{\beta}\frac{l_1}{r}, \qquad \dot{\alpha}_3 = \frac{v_A}{r_3}\cos\psi + \dot{\beta}\frac{l}{r_3}\sin\psi. \tag{5}$$

Taking into account the velocity distribution for the points *A*, *B*, and *C* (Figure 3) and Equation (5), the angular velocity of formative wheel 1z is expressed by:

$$\alpha = \frac{1}{2}(\alpha_1 + \alpha_2). \tag{6}$$

4. Kinematics of the propelling system

The other system is the so-called propelling system. Likewise, the chassis and the bracket with the caster wheel undergo planar motion. The velocity distribution of the characteristic points of the system is shown in Figure 4.

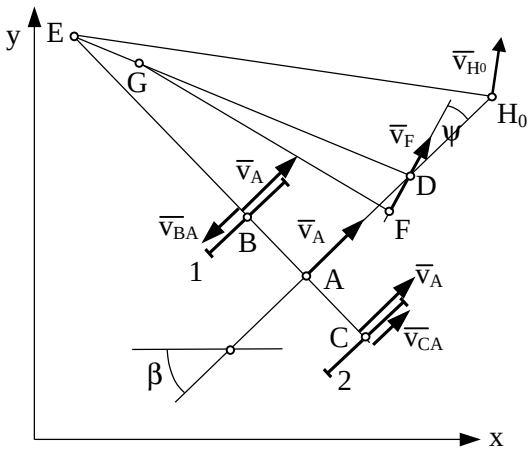

Fig. 4. The velocity distribution of the system

The corresponding formulae describing the kinematics of propelling system are as follows [4]:

$$\dot{x}_F = v_F\cos(\beta + \psi), \qquad \dot{y}_F = v_F\sin(\beta + \psi), \tag{7}$$

$$x_F = x_A + l\cos\beta - l_4\cos(\beta + \psi), \qquad y_F = y_A + l\sin\beta - l_4\sin(\beta + \psi), \tag{8}$$

$$\dot{\psi} = \frac{1}{l_4}\left[\dot{\beta}(l\cos\psi - l_4) - v_A\sin\psi\right], \tag{9}$$

$$\dot{\alpha}_1 = \frac{v_A}{r} - \dot{\beta}\frac{l_1}{r}, \qquad \dot{\alpha}_2 = \frac{v_A}{r} + \dot{\beta}\frac{l_1}{r}, \qquad \dot{\alpha}_3 = \frac{v_A}{r_3}\cos\psi + \dot{\beta}\frac{l}{r_3}\sin\psi. \tag{10}$$

5. Dynamics of the mobile robot

In this section, the dynamics of constructional schemes is described based on classical equations of mechanics; the dynamics of the bracket and the caster wheel is excluded. The motion of the robot is considered in the plane xy inclined to the horizontal plane x_0y_0, where γ is the angle of inclination of the motion plane (Figure 5).

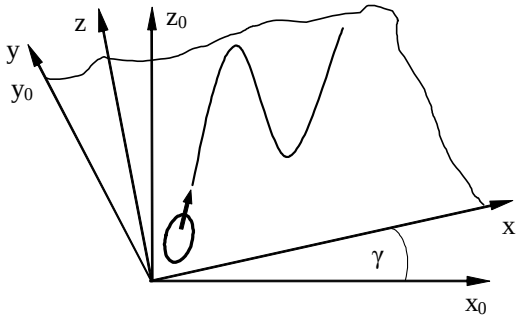

Fig. 5. The motion plane of the system

The mathematical model of the mobile robot described by n generalized coordinates grouped together in the vector q and subjected to $s < n$ nonholonomic constraints is derived. The formulation of the model of interest is based on Lagrange's equations for constrained mechanical systems.

Lagrange's equations of the system at hand have the form [1, 2, 6]:

$$\frac{d}{dt}\left(\frac{\partial E}{\partial \dot{q}}\right) - \frac{\partial E}{\partial q} + \frac{\partial V}{\partial q} = Q + J^T(q)\lambda, \tag{11}$$

where $E = E(q, \dot{q})$ is the kinetic energy of the system, V is the Newtonian potential of the system, Q is the vector of generalized forces, $J(q)$ is the matrix associated with the constraints, q is the vector of generalized coordinates, $\dot{q}$ is the vector of generalized velocities, λ is the vector of the Lagrange multipliers, and the superscript T is the transpose of a matrix operator.

The matrix $J(q)$ is obtained from the equations of kinematic constraints in terms of generalized velocities, i.e., [1, 2, 6]:

$$J(q)\,\dot{q} = 0. \tag{12}$$

5.1. Dynamics of the dragging system

The position and orientation of the mobile robot excluding the bracket with the caster wheel are described by the following vector of generalized coordinates:

$$q = [x_A, y_A, \beta, \alpha]^T. \tag{13}$$

As is mentioned earlier, the mobile robot has two degrees of freedom only. There are two nonholonomic constraints. From Equation (12) the matrix $J(q)$ is given by:

$$J(q) = \begin{bmatrix} 1 & 0 & 0 & -r\cos\beta \\ 0 & 1 & 0 & -r\sin\beta \end{bmatrix}, \tag{14}$$

where $r = r_1 = r_2$.

It is shown that the kinetic energy of the dragging system takes the form [3, 5]:

$$\begin{aligned} E = {} & \frac{1}{2}(m_1 + m_2 + m_4)\dot{x}_A^2 + \frac{1}{2}(m_1 + m_2 + m_4)\dot{y}_A^2 + (m_1 - m_2)l_1\dot{\beta}(\dot{x}_A\cos\beta \\ & + \dot{y}_A\sin\beta) + m_4 l_2\dot{\beta}(\dot{x}_A\sin\beta - \dot{y}_A\cos\beta) + (I_{z1} - I_{z2})h_1\dot{\alpha}\,\dot{\beta} + \frac{1}{2}(I_{z1} + I_{z2})h_1^2\dot{\beta}^2 \\ & + \frac{1}{2}\left(m_1 l_1^2 + m_2 l_1^2 + m_4 l_2^2 + I_{x1} + I_{x2} + I_{z4}\right)\dot{\beta}^2 + \frac{1}{2}(I_{z1} + I_{z2})\dot{\alpha}^2, \end{aligned} \tag{15}$$

where m_1, m_2, m_4 are the masses of members of the system, I_{x1}, I_{x2}, I_{z1}, I_{z2}, I_{z4} are the inertia moments of movable members of the system, $h_1 = l_1/r$ is a nondimensional parameter.

Gravitation potential of the dragging system is:

$$V = (m_1 + m_2 + m_4)\, g \sin\gamma\, x_A - m_4 g\, l_2 \sin\gamma\cos\beta + \left[(m_1 + m_2)r + m_4 h_S\right] g\cos\gamma, \tag{16}$$

where h_S is the distance between the centre of inertia and the motion plane of the robot, g is the acceleration due to gravity.

The vector of unconstrained generalized forces is given by:

$$\tau = \begin{bmatrix} 0 \\ 0 \\ (M_1 - M_2 - N_1 f_1 + N_2 f_2)h_1 \\ M_1 + M_2 - N_1 f_1 - N_2 f_2 \end{bmatrix}, \tag{17}$$

where M_1, M_2 are the driving torques, N_1, N_2 are the axial forces acting on the wheels, f_1, f_2 are the coefficients of rolling friction.

When the robot motion over the inclined plane is realized, the value of the resisting force depends on the robot orientation on the motion plane *xy*. The axial forces are expressed by [4]:

$$\begin{aligned} N_1 &= N_0\left[\left(1-\frac{l_2}{l}\right)\cos\gamma - h_S\sin\gamma\left(\frac{1}{l_1}\sin\beta+\frac{1}{l}\cos\beta\right)\right], \\ N_2 &= N_0\left[\left(1-\frac{l_2}{l}\right)\cos\gamma + h_S\sin\gamma\left(\frac{1}{l_1}\sin\beta-\frac{1}{l}\cos\beta\right)\right], \end{aligned} \tag{18}$$

where $N_0 = 0.5(m_1+m_2+m_4)g$.

Taking into account Equations (14)–(17), Lagrange's equations (11) for this model are as follows:

$$\begin{aligned} &m_4 l_2\ddot{\beta}\sin\beta + (2m_1+m_4)r\ddot{\alpha}\cos\beta + m_4 l_2\dot{\beta}^2\cos\beta - (2m_1+m_4)r\dot{\alpha}\dot{\beta}\sin\beta \\ &\qquad + (m_1+m_2+m_4)g\sin\gamma = \lambda_1, \\ &-m_4 l_2\ddot{\beta}\cos\beta + (2m_1+m_4)r\ddot{\alpha}\sin\beta + m_4 l_2\dot{\beta}^2\sin\beta + (2m_1+m_4)r\dot{\alpha}\dot{\beta}\cos\beta = \lambda_2, \\ &(2m_1 l_1^2 + m_4 l_2^2 + 2I_{x1} + 2I_{z1}h_1^2 + I_{z4})\ddot{\beta} - m_4 l_2 r\dot{\alpha}\dot{\beta} + m_4 g\, l_2\sin\gamma\sin\beta \\ &\qquad = (M_1 - M_2 - N_1 f_1 + N_2 f)h_1, \\ &(2m_1 + m_4 + \frac{2}{r^2}I_{z1})r^2\ddot{\alpha} + m_4 l_2 r\dot{\beta}^2 + (m_1+m_2+m_4)g\, r\sin\gamma\cos\beta \\ &\qquad = M_1 + M_2 - N_1 f_1 - N_2 f_2, \end{aligned} \tag{19}$$

where λ_1, λ_2 are the Lagrange multipliers.

5.2. Dynamics of the propelling system

Likewise, the position and orientation of the mobile robot are described by the vector of generalized coordinates:

$$q = [x_A, y_A, \beta, \alpha]^T. \tag{20}$$

The kinetic energy of the propelling system takes the form:

$$E=\frac{1}{2}(m_1+m_2+m_4)\,\dot{x}_A^2+\frac{1}{2}(m_1+m_2+m_4)\,\dot{y}_A^2+m_4 l_2\dot{\beta}(-\dot{x}_A\sin\beta+\dot{y}_A\cos\beta)$$
$$+\frac{1}{2}(I_{z1}+I_{z2})\,h_1^2\dot{\beta}^2+\frac{1}{2}(m_1 l_1^2+m_2 l_1^2+m_4 l_2^2+I_{x1}+I_{x2}+I_{z4})\,\dot{\beta}^2+\frac{1}{2}(I_{z1}+I_{z2})\,\dot{\alpha}^2. \quad (21)$$

Gravitation potential for this system is expressed by:

$$V=(m_1+m_2+m_4)\,g\sin\gamma\,x_A+m_4 g\,l_2\sin\gamma\cos\beta+[(m_1+m_2)\,r+m_4 h_S]\,g\cos\gamma\,. \quad (22)$$

The vector of unconstrained generalized forces is given by:

$$\tau=\begin{bmatrix}0\\0\\(-M_1+M_2+N_1 f_1-N_2 f_2)h_1\\M_1+M_2-N_1 f_1-N_2 f_2\end{bmatrix}, \quad (23)$$

where the resisting forces are:

$$N_1=N_0\left[\left(1-\frac{l_2}{l}\right)\cos\gamma+h_S\sin\gamma\left(\frac{1}{l_1}\sin\beta+\frac{1}{l}\cos\beta\right)\right],$$
$$N_2=N_0\left[\left(1-\frac{l_2}{l}\right)\cos\gamma-h_S\sin\gamma\left(\frac{1}{l_1}\sin\beta-\frac{1}{l}\cos\beta\right)\right]. \quad (24)$$

Lagrange's equations (11) for this case are written in the form:

$$\begin{aligned}
&-m_4 l_2\ddot{\beta}\sin\beta+(2m_1+m_4)\,r\ddot{\alpha}\cos\beta-m_4 l_2\,\dot{\beta}^2\cos\beta-(2m_1+m_4)\,r\dot{\alpha}\,\dot{\beta}\sin\beta\\
&\qquad+(m_1+m_2+m_4)\,g\sin\gamma=\lambda_1,\\
&m_4 l_2\ddot{\beta}\cos\beta+(2m_1+m_4)\,r\ddot{\alpha}\sin\beta-m_4 l_2\,\dot{\beta}^2\sin\beta+(2m_1+m_4)\,r\dot{\alpha}\dot{\beta}\cos\beta=\lambda_2,\\
&(2m_1 l_1^2+m_4 l_2^2+2I_{x1}+2I_{z1}h_1^2+I_{z4})\,\ddot{\beta}+m_4 l_2 r\dot{\alpha}\dot{\beta}-m_4 g\,l_2\sin\gamma\sin\beta\\
&\qquad=(-M_1+M_2+N_1 f_1-N_2 f_2)h_1,\\
&\left(2m_1+m_4+\frac{2}{r^2}I_{z1}\right)r^2\ddot{\alpha}-m_4 l_2 r\,\dot{\beta}^2+(m_1+m_2+m_4)\,g\,r\sin\gamma\cos\beta\\
&\qquad=M_1+M_2-N_1 f_1-N_2 f_2.
\end{aligned} \quad (25)$$

6. Simulation

In this section, simulation results of inverse kinematic and dynamic problem using the systems suggested earlier are presented. Computer simulation makes it possible to find the solution for the system of Equations (4), (5), (9), (10), (19) and (25), and then to determine the kinematic and dynamic parameters of motion being of our interest. In the first step, the problem of inverse kinematics is realized. Considering the problem of inverse dynamics, we obtain the required time histories of motion parameters as a result of solving inverse kinematics problem. The scheme of executed process is shown in Figure 6.

Fig. 6. The scheme of the problem of inverse dynamics

It is assumed that the point H (the dragging system) or the point H_0 (the propelling system) moves along the trajectory that consists of straight lines and sinusoidal path of the amplitude A_0 = 1 [m] and the period L = 2.45 [m] described by the following function:

$$y_H = A_0 \sin \omega x_H , \tag{26}$$

where $\omega = 2\pi/L$.

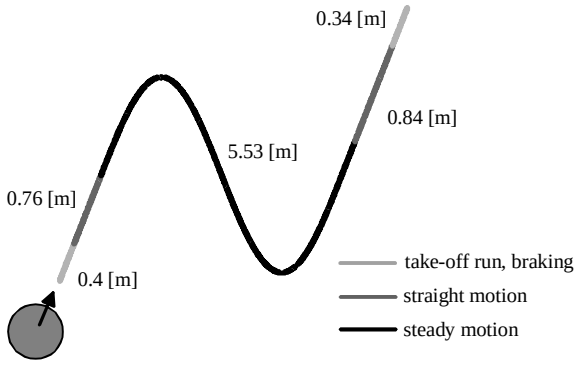

Fig. 7. The assigned trajectory of characteristic point H (H_0) of the system

The motion phases, i.e.: take-off run, steady motion and braking, are analyzed. The parameters characterizing the mobile robot used in calculations are shown in the Table.

Table. Parameters characterizing the two-wheeled mobile robot

m_1 [kg]	m_4 [kg]	I_{x1} [kg·m²]	I_{z1} [kg·m²]	I_{z4} [kg·m²]	N_0 [N]
1.5	5.67	0.00255	0.0051	0.154	43.35
f_1 [m]	l [m]	l_1 [m]	l_2 [m]	l_3 [m]	l_4 [m]
0.01	0.217	0.163	0.07	0.133	0.025
l_5 [m]	r [m]	r_3 [m]	h_S [m]		
0.27	0.0825	0.035	0.1		

In this table, $l_5 = AH$. It is assumed that $f_1 = f_2$ and $m_1 = m_2$. The velocity v_A of the point A equal to 0.3 m/s is used in the calculations and is assumed to be constant. Parameters of the trajectory are selected experimentally.

6.1. Inverse kinematic problem

In this subsection, the results of the inverse kinematic problem of both systems considered are presented. For all examples the time histories of the parameters of motion, including angular velocities and angles of rotation of wheels 1, 2, and 3 and angular velocity and angle of rotation of chassis 4 as well as angular velocity and angle of rotation of the bracket with respect to the chassis, are obtained by using a computer simulation.

Parameters of motion of the dragging system are displayed in Figures 8 and 9. Substantial changes in the angular velocities when the robot is on the move along the turn (upper and lower vertices of the sinusoidal trajectory) are observed. When the robot over the straight line is moved, the angular velocities $\dot{\beta}$ and $\dot{\psi}$ equalize and are equal to null. The angles β and ψ are changed when the system is on the move along the turn.

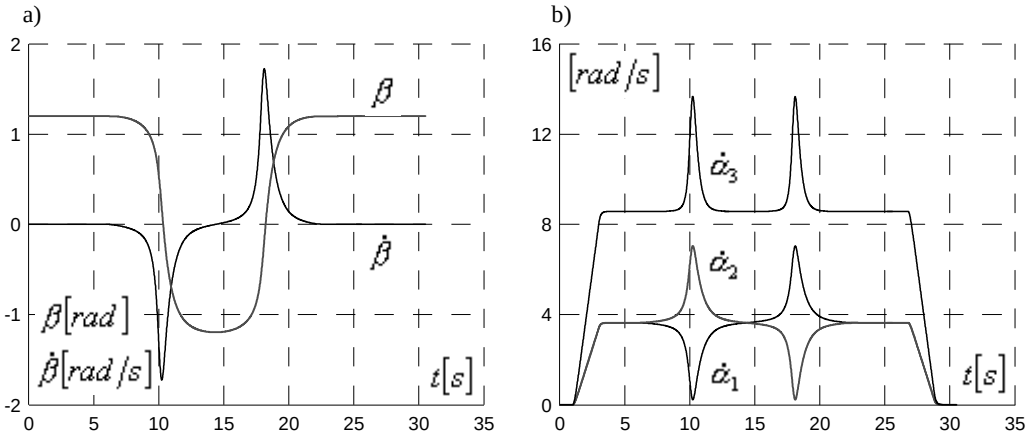

Fig. 8. Time histories of motion parameters of the dragging system

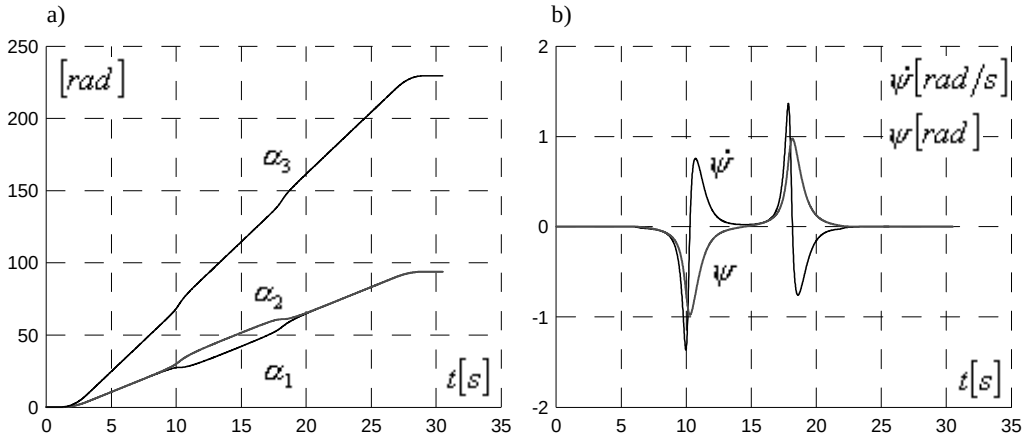

Fig. 9. Time histories of motion parameters of the dragging system

In Figures 10 and 11, the parameters of motion of the propelling system are shown.

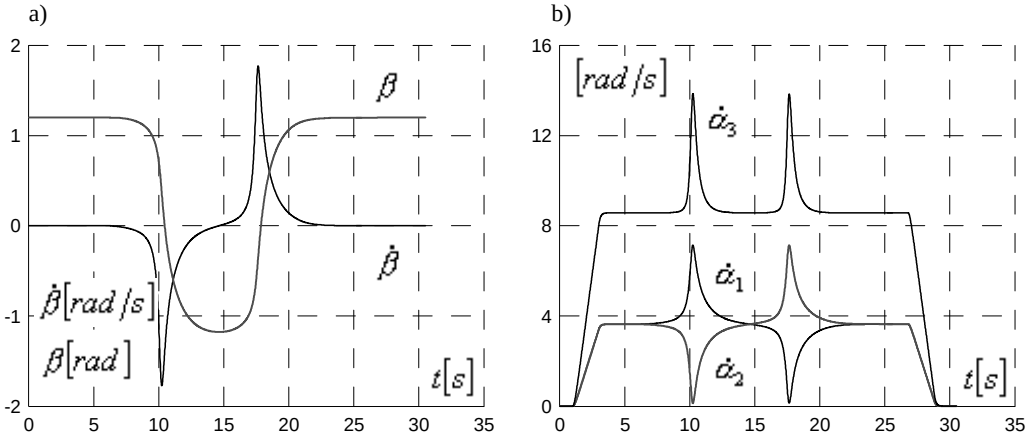

Fig. 10. Time histories of motion parameters of the propelling system

Likewise, the substantial changes of kinematic parameters when the robot is on the move along the turn are observed. Computer simulation results show that the slight qualitative and quantitative differences between the dragging and propelling systems appear. The parameters of motion are needed to solve the problem of the inverse dynamics, i.e., to find the driving torques of wheels 1 and 2, respectively.

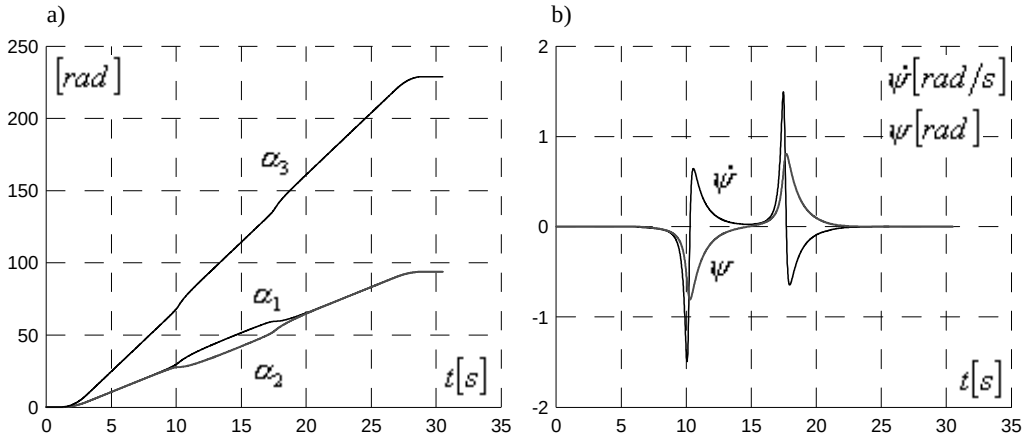

Fig. 11. Time histories of motion parameters of the propelling system

6.2. Inverse dynamic problem

In this subsection, simulation results of an inverse dynamic problem are presented. Computer simulation makes it possible to find the solution for a system of Equations (19) and (25), i.e., to determine the driving torques and the Lagrange multipliers. For both systems the cases where $\gamma = \pi/24$ and $\gamma = 0$ are solved.

Parameters of motion of the dragging model are displayed in Figures 12 and 13.

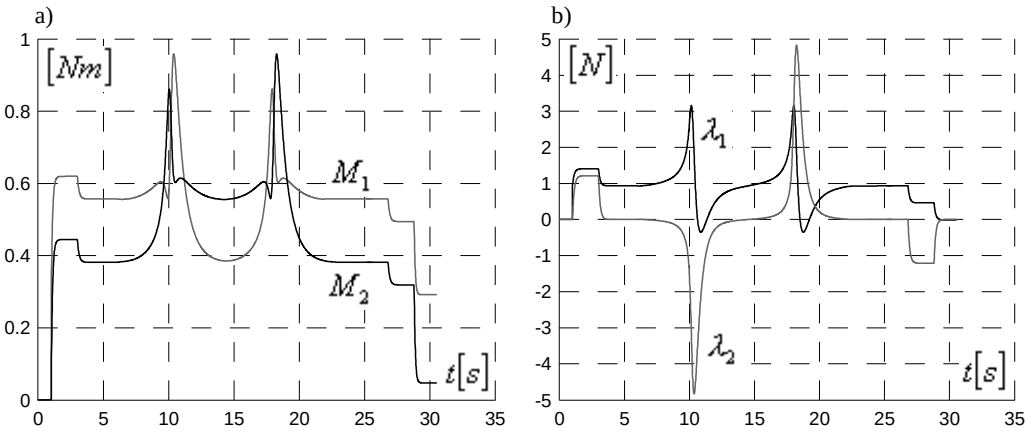

Fig. 12. Time histories of the driving torques (a) and the Lagrange multipliers (b), ($\gamma = \pi/24$)

Substantial changes of the driving torques and the Lagrange multipliers when the robot is on the move along the turn are observed.

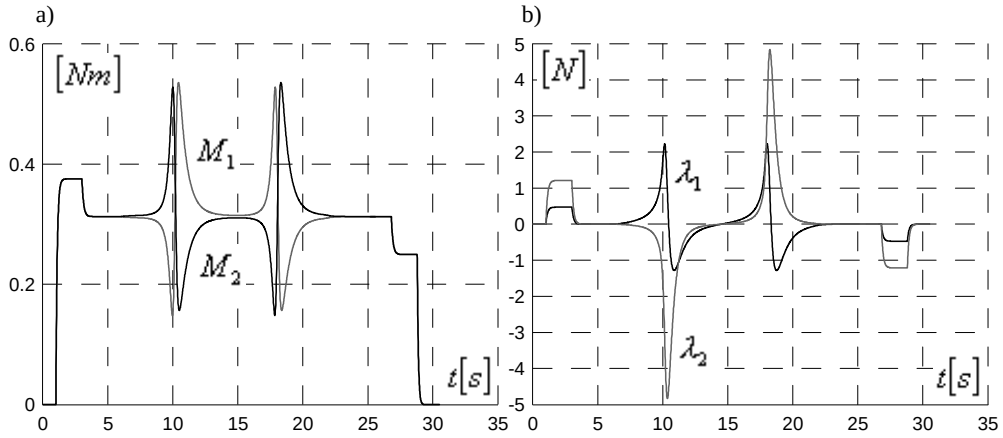

Fig. 13. Time histories of the driving torques (a) and the Lagrange multipliers (b), ($\gamma = 0$)

Considerable changes in the driving torques and the Lagrange multipliers at the take-off run time and braking and when the robot is on the move along the turn are shown in Figures 12 and 13.

The parameters of motion of the propelling model are displayed in Figures 14 and 15.

Likewise, considerable changes in the driving torques and the Lagrange multipliers at the take-off run time and braking and when the robot is on the move along the turn are observed.

For both cases of the systems analyzed, extremum values of the driving torques and the Lagrange multipliers are higher for the propelling system compared to the dragging system.

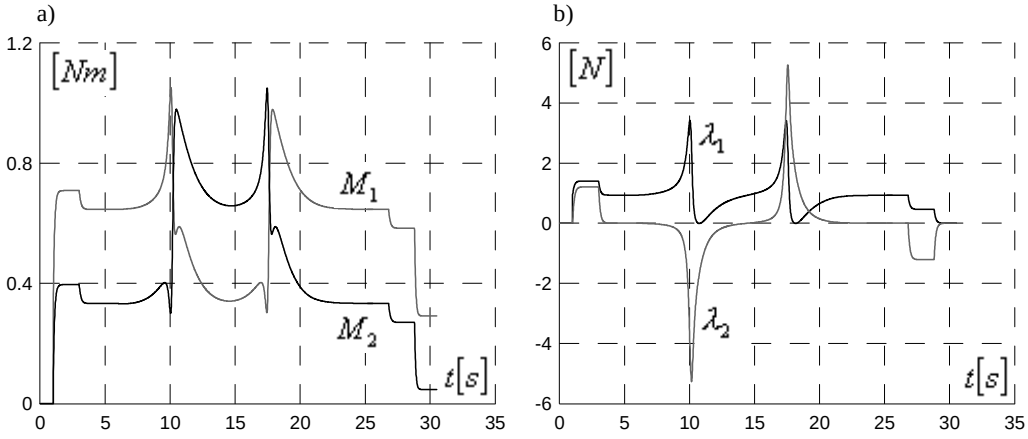

Fig. 14. Time histories of the driving torques (a) and the Lagrange multipliers (b), ($\gamma = \pi/24$)

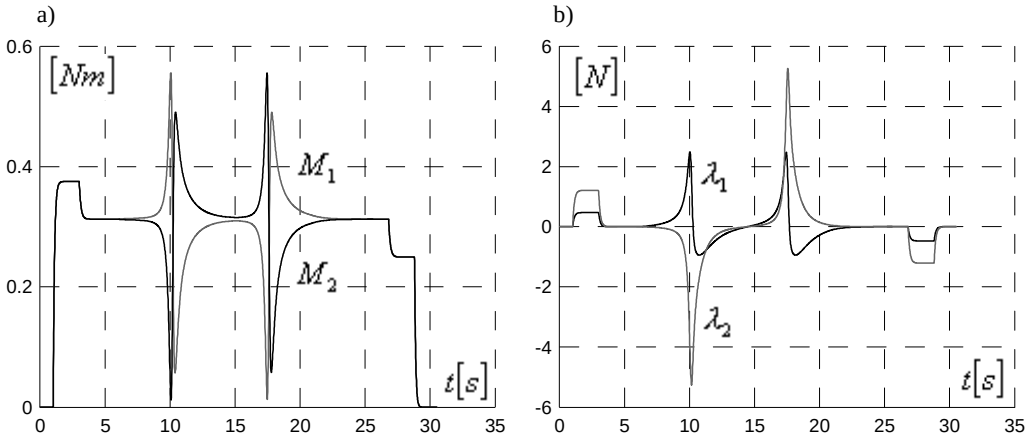

Fig. 15. Time histories of the driving torques (a) and the Lagrange multipliers (b), ($\gamma = 0$)

7. Conclusions

Kinematic and dynamic analysis of the system is involved in the problems of inverse kinematics and dynamics. Motions of the dragging and propelling systems using classical equations of mechanics are described including the kinematics of the bracket and the caster wheel.

In the present paper, the curvilinear trajectory of the point H (the dragging system) or the point H_0 (the propelling system) of the two-wheeled mobile robot is considered. The trajectory planing is an important problem in the process of identification in real time. Such a trajectory should have a persistence of excitation (PE) condition of the above mentioned mobile robot. On the other hand, the trajectory needed should be realized by the robot.

Based on classical equation of mechanics the dynamics of the systems analyzed is described, including the motion over the inclined plane subjected to nonholonomic constraints.

In an available literature, the author has not found examples of using this method for the analysis of the problems of inverse kinematics and dynamics of a two-wheeled mobile robot that includes a bracket and a caster wheel and moves over the inclined plane.

Time histories of motion parameters can be utilized to plan the movement trajectory system in joint variables or to solve the problem of the control of this object.

Simulation results show that the slight qualitative and quantitative differences (with the exception of the motion over the inclined plane) between the dragging and propelling systems emerge.

This consideration can be applied to kinematic and dynamic description of any wheeled mobile robot model, independently of the number of its wheels.

Acknowledgement

The author would like to thank the reviewers for their careful reading of the paper and their helpful comments.

References

[1] Gutowski R.: *Analytical Mechanics*, PWN, Warsaw, 1971 (in Polish).
[2] Nejmark J.I., Fufajev N.A.: *Dynamics of Nonholonomic Systems*, PWN, Warsaw, 1971 (in Polish).
[3] Noga S.: *Kinematics of an optional nonholonomic mobile robot*, Proceedings of the 3th Ukrainian–Polish Scientific Conference *Mechanics and Informatics*, Khmelnitskij, 2005, pp. 77–80.
[4] Noga S.: *Kinetics of a two wheeled mobile robot*, PhD Thesis, Faculty of Mechanical Engineering and Aeronautics, Rzeszów University of Technology, Rzeszów, 2004 (in Polish).
[5] Noga S.: *Modelling and dynamical analysis of the two wheeled mobile robot*, Technical Journal, Cracow University of Technology Publishers, Cracow, 2005, z. 14–M, pp. 63–81 (in Polish).
[6] Ostrovskaya S., Angeles J.: *Nonholonomic systems revisited within the framework of analytical mechanics*, Applied Mechanics Reviews, 1998, Vol. 51, No. 7, pp. 415–433.
[7] *Pioneer 2 Mobile Robot – Operations Manual*, 1999, ActivMEDIA ROBOTICS, LLC.
[8] Yu Q., Chen I.-M.: *A general approach to the dynamics of nonholonomic mobile manipulator systems*, Journal of Dynamic Systems, Measurement and Control, 2002, Vol. 124, pp. 512–521.
[9] Zhang Y.L., Velinsky S.A., Feng X.: *On the tracking control of differentially steered wheeled mobile robots*, Journal of Dynamic Systems, Measurement and Control, 1997, Vol. 119, pp. 455–461.
[10] Żylski W., Hendzel Z., Noga S.: *Inverse kinematics problem of a mobile 2-wheeled robot*, Proceedings of the International Scientific Conference *Mechanics 2000*, Rzeszów, 2000, pp. 491– 495.
[11] Żylski W., Noga S.: *Neural modelling dynamics of a mobile wheeled robot*, Proceedings of the 11th International Symposium on Dynamics of Structures, Rzeszów–Arłamów, 2002, pp. 629–636 (in Polish).

Kinematyka i dynamika wybranych mobilnych robotów dwukołowych

Opisano modelowanie wybranych rozwiązań konstrukcyjnych mobilnego robota dwukołowego oznaczonych jako układ ciągniony oraz układ napędzany. Rozważany pojazd jest układem z więzami nieholonomicznymi. Analizowane są przypadki, w których roboty poruszają się po powierzchni nachylonej. Dla przyjętych modeli koncepcyjnych rozwiązano zadanie odwrotne kinematyki i dynamiki, zakładając, że wybrane punkty pojazdów poruszają się po torze złożonym z odcinków linii prostych i łuku w kształcie funkcji sinus. Zaprezentowano zależności wybranych parametrów kinematycznych i dynamicznych układów od czasu, które otrzymano w wyniku numerycznego rozwiązania wyprowadzonych wcześniej równań ruchu.

Z przedstawionych wyników i metodyki postępowania mogą korzystać potencjalni konstruktorzy na etapie rozważań koncepcyjnych w procesie projektowania tego typu pojazdów.

ARCHIVES OF CIVIL AND MECHANICAL ENGINEERING

Vol. VI 2006 No. 3

Acoustic waves in rubberlike layered media

S. KOSIŃSKI
Częstochowa University of Technology, Faculty of Civil Engineering, ul. Akademicka 3,
42-200 Częstochowa

The paper focuses on the propagation of 1-D acoustic waves in an elastic isotropic material with the elastic potential proposed by Blatz and Ko [1]. Two special models of materials are described by this potential: foamed polyurethane elastomers and solid polyurethane rubbers. The problem of reflection and transmission of 1-D acoustic waves at the interface of two different media and the problem of multiple reflections in an elastic layer of finite length bounded by two elastic half spaces are discussed. The standard procedure for the linearisation of equations of motion was used. This approach is based on the assumption that small, time-dependent motions are superimposed on large static deformations.

Keywords: *rubberlike materials, layered composites, reflection and transmission of acoustic waves, small motions superimposed on large static deformations*

1. Basic equations

The general motion to be discussed here is defined by (1). It is assumed that the solid has been subjected to an initial static homogeneous deformation with constant principal stretches λ_1, λ_2, λ_3 and to a superimposed small motion $u_i = u_i(X_1,t), i = 1,3,$ characterized by a small displacement field which is time dependent. The final and static deformations are very close:

$$x_1 = \lambda_1 X_1 + u_1(X_1,t), \qquad x_2 = \lambda_2 X_2, \qquad x_3 = \lambda_3 X_3 + u_3(X_1,t). \tag{1}$$

The components of the deformation gradients $\mathbf{F}_0$ and $\hat{\mathbf{F}}$ (for static and final deformation) and the components of the right Cauchy–Green tensor $\hat{\mathbf{C}}$ are as follows:

$$[\mathbf{F}_0] = \begin{bmatrix} \lambda_1 & 0 & 0 \\ 0 & \lambda_2 & 0 \\ 0 & 0 & \lambda_3 \end{bmatrix}, \quad [\hat{\mathbf{F}}] = \begin{bmatrix} \hat{\lambda}_1 & 0 & 0 \\ 0 & \lambda_2 & 0 \\ \gamma & 0 & \lambda_3 \end{bmatrix}, \quad [\hat{\mathbf{C}}] = \begin{bmatrix} \hat{\lambda}_1^2 + \gamma^2 & 0 & \gamma\lambda_3 \\ 0 & \lambda_2^2 & 0 \\ \gamma\lambda_3 & 0 & \lambda_3^2 \end{bmatrix}, \tag{2}$$

where $\hat{\lambda}_1 = \lambda_1 + u_{1,1}(X_1,t), \qquad \gamma = u_{3,1}(X_1,t).$

The basic invariants of the right Cauchy–Green tensor $\hat{\mathbf{C}}$ are

$$I_1 = \operatorname{tr}\hat{\mathbf{C}}, \qquad I_2 = \frac{1}{2}\left(I_1^2 - \operatorname{tr}\hat{\mathbf{C}}^2\right), \qquad I_3 = \det\hat{\mathbf{C}} \tag{3}$$

and it follows from (2) and (3) that

$$I_1 = \hat{\lambda}_1^2 + \lambda_2^2 + \lambda_3^2 + \gamma^2, \quad I_2 = \hat{\lambda}_1^2\lambda_2^2 + \hat{\lambda}_1^2\lambda_3^2 + \lambda_2^2\lambda_3^2 + \gamma^2\lambda_2^2, \qquad I_3 = \hat{\lambda}_1^2\lambda_2^2\lambda_3^2. \tag{4}$$

For a compressible hyperelastic material there exists a strain energy function represented by $W = W(\mathbf{F})$, defined in the space of deformation gradients such that the nominal stress tensor ([2], [3]) is defined by

$$\mathbf{S} = \frac{\partial W(\mathbf{F})}{\partial \mathbf{F}}. \tag{5}$$

If the material is isotropic

$$\mathbf{S} = 2W_1\mathbf{F}^T + 2W_2\left(I_1\mathbf{F}^T - \mathbf{C}\mathbf{F}^T\right) + 2W_3I_3\mathbf{F}^{-1}, \tag{6}$$

where $W_i = \partial W / \partial I_i, \quad i = 1, 2, 3.$

It may be easy deduced from (2) and (6) that the non-zero components $\mathbf{S}$ and $\hat{\mathbf{S}}$ of the nominal stress tensor are given by

$$[\mathbf{S}] = \begin{bmatrix} S_{11} & 0 & S_{13} \\ 0 & S_{22} & 0 \\ S_{31} & 0 & S_{33} \end{bmatrix}, \qquad [\hat{\mathbf{S}}] = \begin{bmatrix} \hat{S}_{11} & 0 & \hat{S}_{13} \\ 0 & \hat{S}_{22} & 0 \\ \hat{S}_{31} & 0 & \hat{S}_{33} \end{bmatrix}, \tag{7}$$

where $S_{\alpha i}, \hat{S}_{\alpha i}$ are the components of the nominal stress tensor for static and final deformations, respectively, and

$$\hat{S}_{11} = \frac{\partial W}{\partial \hat{\lambda}_1} = 2W_1\hat{\lambda}_1 + 2W_2\hat{\lambda}_1\left(\lambda_2^2 + \lambda_3^2\right) + 2W_3\hat{\lambda}_1\lambda_2^2\lambda_3^2, \qquad \hat{S}_{13} = \frac{\partial W}{\partial \gamma} = 2\left(W_1 + W_2\lambda_2^2\right)\gamma. \tag{8}$$

Insertion of (8) into the differential equations of finite elasticity gives the non-trivial equations of motion for the superimposed infinitesimal displacement

$$A_{11}^{11}u_{1,11} + A_{13}^{11}u_{3,11} = \rho_R\ddot{u}_1, \qquad A_{31}^{11}u_{1,11} + A_{33}^{11}u_{3,11} = \rho_R\ddot{u}_3, \tag{9}$$

where

$$A_{11}^{11}=\left.\frac{\partial^2 W}{\partial\hat{\lambda}_1^2}\right|_{\lambda_i},\qquad A_{13}^{11}=A_{31}^{11}=\left.\frac{\partial^2 W}{\partial\hat{\lambda}_1\partial\gamma}\right|_{\lambda_i},\qquad A_{33}^{11}=\left.\frac{\partial^2 W}{\partial\gamma^2}\right|_{\lambda_i},\tag{10}$$

and the values of the derivatives are calculated for the initial static deformation λ_i, $i = 1, 2, 3$.

2. Constitutive relations

The purpose of this paper was to consider the propagation of acoustic waves in a compressible isotropic rubberlike solids. A purely mechanical theory is considered. The results are obtained for the generalized Blatz and Ko strain energy function [1]

$$W=\frac{\mu f}{2}\left[I_1-3+\frac{1-2\nu}{\nu}\left(I_3^{-\nu/(1-2\nu)}-1\right)\right]+\frac{\mu(1-f)}{2}\left[\frac{I_2}{I_3}-3+\frac{1-2\nu}{\nu}\left(I_3^{\nu/(1-2\nu)}-1\right)\right],\tag{11}$$

where I_1, I_2 and I_3 are the principal invariants of the deformation tensors, μ and ν are respectively the shear modulus and Poisson's ratio for infinitesimal deformation from the natural reference state, and coefficient f, $0 \le f \le 1$ is a material constant connected with the porosity volume of the material.

There are two special cases important to applications; the first $f = 0$ (foamed polyurethane rubber) and the second $f = 1$ (solid polyurethane rubber). It is easy to find ([4], [5]) that for $f = 0$ the value of the Poisson's ratio is $\nu = 0.25$, and for $f = 1$, $\nu = 0.47$.

3. Conditions for propagation of acoustic waves

Now we consider independently the propagation of acoustic waves in both special materials defined above. For solid polyurethane rubber ($f = 1$) the values of the derivatives and the coefficients in equations of motion (9) take the form

$$W_1=\frac{\mu}{2},\qquad W_2=0,\qquad W_3=-\frac{\mu}{2}\left(\hat{\lambda}_1^2\lambda_2^2\lambda_3^2\right)^{-(1-\nu)/(1-2\nu)},\tag{12}$$

$$\begin{aligned}
&A_{11}^{11}=\mu\left[1+\left(\lambda_2\lambda_3\right)^{-2\nu/(1-2\nu)}\lambda_1^{-(1-\nu)/(1-2\nu)}\left(\frac{2(1-\nu)}{1-2\nu}\lambda_1^{-(1-\nu)/(1-2\nu)}-1\right)\right],\\
&A_{33}^{11}=\mu,\\
&A_{13}^{11}=A_{31}^{11}=0.
\end{aligned}\tag{13}$$

The linearised system of equations of motion reduces to two independent uncoupled wave equations with the constant wave speeds c_L, c_T :

$$c_L^2 = \frac{A_{11}^{11}}{\rho_R}, \quad c_T^2 = \frac{A_{33}^{11}}{\rho_R}, \quad c_L^2(\mathbf{1}) = \frac{A_{11}^{11}(\mathbf{1})}{\rho_R} = \frac{\lambda + 2\mu}{\rho_R}, \quad c_T^2(\mathbf{1}) = \frac{A_{33}^{11}(\mathbf{1})}{\rho_R} = \frac{\mu}{\rho_R}. \tag{14}$$

If the solid is not deformed (**F** = **1**), both these speeds are equal to the speeds of infinitesimal longitudinal and transverse waves in unbounded medium. The components of the nominal stress tensor required in this paper after linearisation are

$$\hat{S}_{11} = S_{11} + A_{11}^{11} u_{1,1}, \quad S_{11} = \mu[\lambda_1 - \lambda_1^{-1/(1-2\nu)} (\lambda_2 \lambda_3)^{-2\nu/(1-2\nu)}],$$

$$\hat{S}_{13} = S_{13} + A_{33}^{11} u_{3,1}, \quad S_{13} = 0. \tag{15}$$

Let us consider now in an analogous manner the second special case which follows from (11) when foamed polyurethane rubber is modelled and $f = 0$. The values of the derivatives and the coefficient of the equations are

$$W_1 = 0, \quad W_2 = \frac{\mu}{2}\left(\hat{\lambda}_1 \lambda_2 \lambda_3\right)^{-2},$$

$$W_3 = \frac{\mu}{2}\left[-\frac{\hat{\lambda}_1^2 \lambda_2^2 + \hat{\lambda}_1^2 \lambda_3^2 + \lambda_2^2 \lambda_3^2 + \gamma^2 \lambda_2^2}{\left(\hat{\lambda}_1 \lambda_2 \lambda_3\right)^4} + \left(\hat{\lambda}_1 \lambda_2 \lambda_3\right)^{(6\nu-2)/(1-2\nu)} \right], \tag{16}$$

$$A_{11}^{11} = \mu\left[3\lambda_1^{-4} + \frac{4\nu - 1}{1 - 2\nu} \lambda_1^{(6\nu-2)/(1-2\nu)} \left(\lambda_2 \lambda_3\right)^{2\nu/(1-2\nu)} \right],$$

$$A_{33}^{11} = \frac{\mu}{\lambda_1^2 \lambda_3^2}, \tag{17}$$

$$A_{13}^{11} = A_{31}^{11} = 0.$$

As in the previous case for $f = 1$ also in this case the linearised equations of motion (9) reduces to two independent uncoupled wave equations with constant propagation speeds. If the medium is not deformed both these speeds take the values as previously

$$c_L^2 = \frac{A_{11}^{11}}{\rho_R}, \quad c_T^2 = \frac{A_{33}^{11}}{\rho_R}, \quad c_L^2(\mathbf{1}) = \frac{A_{11}^{11}(\mathbf{1})}{\rho_R} = \frac{\lambda + 2\mu}{\rho_R}, \quad c_T^2(\mathbf{1}) = \frac{A_{33}^{11}(\mathbf{1})}{\rho_R} = \frac{\mu}{\rho_R}. \tag{18}$$

As above, only two components of the nominal stress tensor are essential in this case. The linearisation of the problem gives the following results:

$$\begin{aligned} &\hat{S}_{11} = S_{11} + A_{11}^{11} u_{1,1}, \qquad S_{11} = \mu[\lambda_1^{(4\nu-1)/(1-2\nu)} (\lambda_2\lambda_3)^{2\nu/(1-2\nu)} - \lambda_1^{-3}], \\ &\hat{S}_{13} = S_{13} + A_{11}^{11} u_{3,1}, \qquad S_{13} = 0. \end{aligned} \tag{19}$$

4. Reflection and transmission of the acoustic wave at the interface

Suppose that half spaces of two different elastic materials are rigidly coupled as shown in Figure 1. Materials on the left- and right-hand sides of the interface are special cases of the Blatz–Ko material when the material coefficient f is equal to zero or unity, respectively. The interface between the two materials is at $X_1 = 0$. In the region $X_1 > 0$, all functions and quantities have the tilde mark.

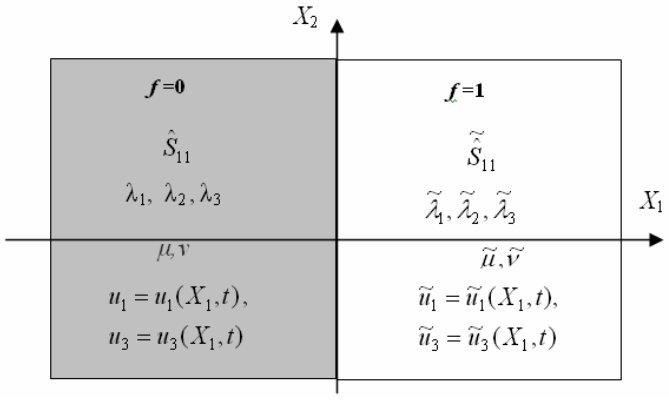

Fig. 1

We consider the linearized boundary value problem. At the interface the continuity conditions must complement the equations of motion. If two solids are in a rigid contact, then the displacement vector and stress vector must be continuous from one medium to the other:

$$U_i = \tilde{U}_i, \qquad \hat{S}_{1i} = \tilde{\hat{S}}_{1i}, \qquad i = 1, 2, 3, \tag{20}$$

where $U_i = x_i - X_i$ (comp. (1)) and the condition $\hat{S}_{12} = \tilde{\hat{S}}_{12} = 0$ is satisfied as identity. The initial static deformations λ_i and $\tilde{\lambda}_i$ are different in both materials under consideration. According to (20), a small wave motion is dynamically admissible if and only if the static deformations and small wave motion satisfy the following conditions:

$$S_{11} = \tilde{S}_{11}, \qquad \lambda_2 = \tilde{\lambda}_2, \qquad \lambda_3 = \tilde{\lambda}_3, \tag{21}$$

$$u_1(0,t) = \tilde{u}_1(0,t), \qquad \rho_R c_L^2 u_{1,1}(0,t) = \tilde{\rho}_R \tilde{c}_L^2 \tilde{u}_{1,1}(0,t),$$

$$u_3(0,t) = \tilde{u}_3(0,t), \qquad \rho_R c_T^2 u_{3,1}(0,t) = \tilde{\rho}_R \tilde{c}_T^2 \tilde{u}_{3,1}(0,t), \tag{22}$$

where the speeds c_L, c_T and $\tilde{c}_L, \tilde{c}_T$ are evaluated at the constant principal stretches λ_i and $\tilde{\lambda}_i$, respectively. Based on Equation (21) it is possible to find the relationship between initial stretches λ_1 and $\tilde{\lambda}_1$

$$\begin{aligned} S_{11} = \tilde{S}_{11} \Rightarrow \mu[\lambda_1^{(4\nu-1)/(1-2\nu)}(\lambda_2\lambda_3)^{2\nu/(1-2\nu)} - \lambda_1^{-3}] \\ = \tilde{\mu}[\tilde{\lambda}_1 - \tilde{\lambda}_1^{-1/(1-2\tilde{\nu})}(\tilde{\lambda}_2\tilde{\lambda}_3)^{-2\tilde{\nu}/(1-2\tilde{\nu})}], \end{aligned} \tag{23}$$

where $\Lambda = \lambda_2\lambda_3 = \tilde{\lambda}_2\tilde{\lambda}_3$.

Poisson's ratio ν of the foamed polyurethane rubber ($f = 0$) equals 0.25 [5] and for this reason condition (23) simplifies and takes the form

$$\lambda_1 = \left\{ \Lambda + \frac{\tilde{\mu}}{\mu}\left[\tilde{\lambda}_1^{-1/(1-2\tilde{\nu})}\Lambda^{-2\tilde{\nu}/(1-2\tilde{\nu})} - \tilde{\lambda}_1\right]\right\}^{-1/3}. \tag{24}$$

If $\tilde{\lambda}_1 = \tilde{\lambda}_2 = \tilde{\lambda}_3 = \tilde{\lambda}$ we obtain additionally

$$\lambda_1 = \left\{ \tilde{\lambda}^2 + \frac{\tilde{\mu}}{\mu}\left[\tilde{\lambda}^{-(4\tilde{\nu}+1)/(1-2\tilde{\nu})} - \tilde{\lambda}\right]\right\}^{-1/3}. \tag{25}$$

Let us consider now the conditions for small wave motion (22). We assume that the incident longitudinal wave in the left half space $u_1^I = u_1^I(t - X_1/c_L)$ propagates in the positive X_1 direction (Figure 2). The interaction of the wave with the interface between the two materials gives rise to a reflected wave $u_1^R = u_1^R(t + X_1/c_L)$ propagating in the negative X_1 direction and a transmitted wave $\tilde{u}_1^T = \tilde{u}_1^T(t - X_1/\tilde{c}_L)$ propagating in the positive X_1 direction.

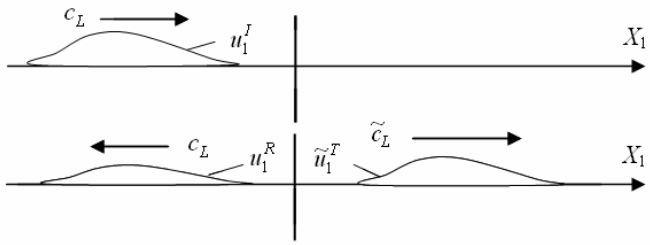

Fig. 2

The superimposed displacement fields in both material regions $X_1 < 0$ and $X_1 > 0$ have the form

$$u_1(x_1,t) = u_1^I\left(t - \frac{X_1}{c_L}\right) + u_1^R\left(t + \frac{X_1}{c_L}\right), \qquad X_1 < 0,$$
$$\tilde{u}_1(x_1,t) = \tilde{u}_1^T\left(t - \frac{X_1}{\tilde{c}_L}\right), \qquad X_1 > 0. \tag{26}$$

Our objective is to determine the reflected and transmitted waves in terms of the incident wave, that is we want to determine the functions u_1^R and $\tilde{u}_1^T$ in terms of the function u_1^I. Using Equations (26) we can write the displacement condition $(22)_1$ and stress condition $(22)_2$ in terms of the three functions described above. Solving these equations for the functions u_1^R and $\tilde{u}_1^T$ we determine the reflected and transmitted waves in terms of the incident wave ([4]):

$$u_1^R\left(t + \frac{X_1}{c_L}\right) = \left(\frac{1-K}{1+K}\right)u_1^I\left(t + \frac{X_1}{c_L}\right), \qquad \tilde{u}_1^T\left(t - \frac{X_1}{\tilde{c}_L}\right) = \left(\frac{2}{1+K}\right)u_1^I\left(t - \frac{X_1}{\tilde{c}_L}\right), \tag{27}$$

where we define $K = \tilde{Z}(Z)^{-1} = \tilde{\rho}_R\,\tilde{c}_L(\rho_R c_L)^{-1}$. The term $Z = \rho_R c_L$ is called the acoustic impedance of the material.

5. Numerical results

The calculations were done for the case where the unbounded region filled with foamed polyurethane rubber ($f = 0$) contains one layer made from solid polyurethane rubber ($f = 1$) of the length $\tilde{d}$ (Figure 3).

Some experimental results for several elastomers are presented in [5]. We assume the following elastic constants and densities: $\tilde{\mu} = 0.233$ MPa, $\mu = 0.221$ MPa, $\tilde{\nu} = 0.47$,

$\nu = 0.25$, $\tilde{\rho}_R = 911\ \mathrm{kg/m^3}$ being in agreement with the main conclusions of this paper. The density of the foam rubber is smaller than the density of solid rubber $\rho_R < \tilde{\rho}_R$ and the elastic constants μ and ν can remain unchanged for modified foam rubber mixtures if the density ρ_R varies. The calculations were made for two values of the density ratios $\rho_R / \tilde{\rho}_R = 0.3$ and $\rho_R / \tilde{\rho}_R = 0.9$. The speeds of wave propagation in undeformed solids in m/sec are equal to $\tilde{c}_T(\mathbf{1}) = 16.02$, $\tilde{c}_L(\mathbf{1}) = 67.38$, $c_T(\mathbf{1}) = 14.74$, $c_L(\mathbf{1}) = 25.32$, respectively.

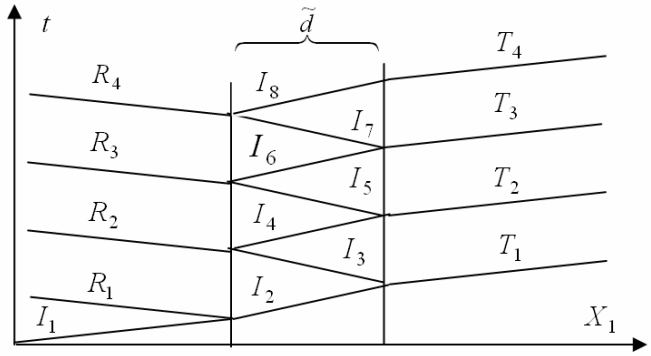

Fig. 3

The propagation of the transverse wave only will be considered below in details. The speed of such a wave in solid rubber defined by $(14)_2$ is independent of the initial deformations. In the foamed polyurethane rubber, the same speed defined by $(18)_2$ depends on the initial deformations.

Let us calculate now the impedance ratio K of both materials connected at an interface when the transverse waves propagate. Insertion of (25) into the expression for impedance ratio K gives

$$K = \frac{Z}{\tilde{Z}} = \frac{c_T \rho_R}{\tilde{c}_T \tilde{\rho}_R} = \left\{ \frac{\mu}{\tilde{\mu}} \frac{\rho_R}{\tilde{\rho}_R} \tilde{\lambda}^{-2} \left[\tilde{\lambda}^2 + \frac{\tilde{\mu}}{\mu} \left(\tilde{\lambda}^{-(4\tilde{\nu}+1)/(1-2\tilde{\nu})} - \tilde{\lambda} \right) \right]^{2/3} \right\}^{1/2}. \tag{28}$$

This relationship K as the function of the initial homogeneous deformation $\tilde{\lambda}$ in rubber is presented in Figure 4. The notations $K_{0.9}$ and $K_{0.3}$ are connected with an adequate density ratio.

The impedances of both materials are the same, $K_{0.9} = 1$ when the principal stretches $\tilde{\lambda}$ are equal to 0.995. According to (25) the principal stretch λ_1 is equal to 0.920. If $K_{0.3} = 1$, we have $\tilde{\lambda} = 0.964$ and $\lambda_1 = 0.548$.

In agreement with (27), we define the reflection R_1 and transmission T_1 coefficients for the first interaction with the interface. They are $R_1 = u_3^R / u_3^I$ and $T_1 = \tilde{u}_3^T / u_3^I$.

$$R_1 = \frac{Z - \tilde{Z}}{Z + \tilde{Z}}, \qquad R_i = \frac{4Z\tilde{Z}}{(Z + \tilde{Z})^2}\left(\frac{\tilde{Z} - Z}{Z + \tilde{Z}}\right)^{2i-3},$$
$$T_j = \frac{4Z\tilde{Z}}{(Z + \tilde{Z})^2}\left(\frac{\tilde{Z} - Z}{Z + \tilde{Z}}\right)^{2j-2}, \qquad i = 2, 3.... \quad j = 1, 2, 3.. \ . \tag{29}$$

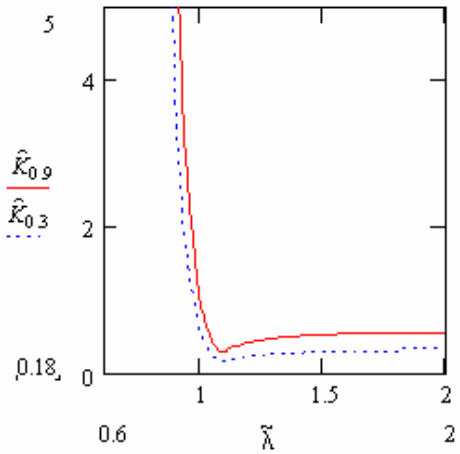

Fig. 4

It is easy to make generalization (29) about these results for multiple wave interactions in the layer of the length $\tilde{d}$ (Figure 3). If the impedances of both materials are equal, i.e., $Z = \tilde{Z}$, there exists the transmitted wave only. The multiple reflections die rapidly away for nearly the same values of impedances, i.e., $Z \approx \tilde{Z}$. It is easy to show that the initial static deformation has important influence on modelling and control of wave phenomena in nonlinear elastic solids. It holds good for the propagation of transverse acoustic waves and also longitudinal acoustic waves.

References

[1] Blatz P.J., Ko W.L.: *Application of finite elastic theory to the deformation of rubbery materials*, Trans. Soc. Rheol., 1962, Vol. 6, 223.

[2] Ogden R.W.: *Nonlinear elastic deformations*, Ellis Forwood Limited Publishers, Chichester, 1984.

[3] Haddow J.B., Erbay H.A.: *Some aspect of finite amplitude transverse waves in a compressible hyperelastic solids*, Q. Jl. Mech. Appl. Math., 2002, Vol. 55, 17.
[4] Bedford A., Drumheller D.S.: *Introduction to elastic wave propagation*, John Willey & Sons Ltd., 1994.
[5] Beatty M.F., Stalnaker D.O.: *The Poisson function of finite elasticity*, Journal of Appl. Mech., 1986, Vol. 53, 807.

Fale akustyczne w gumopodobnych ośrodkach warstwowych

Przedstawiono propagację jednowymiarowych fal akustycznych we wstępnie odkształconym materiale Blatza–Ko. Potencjał sprężysty opisujący ten materiał umożliwia modelowanie zachowania zarówno gumy, jak też gumy piankowej. Rozpatrzono odbicie–załamanie fali akustycznej na granicy dwóch różnych ośrodków oraz przypadek odbicia wielokrotnego.

Do analizy zastosowano standardową procedurę linearyzacji równań ruchu opartą na założeniu, że na duże statyczne deformacje ośrodka nałożone są małe przemieszczenia związane z propagacją fal.

ARCHIVES OF CIVIL AND MECHANICAL ENGINEERING

Vol. VI 2006 No. 3

Development tendency for accident situation in building industry

B. HOŁA
Wrocław University of Technology, Wybrzeże Wyspiańskiego 27, 50-370 Wrocław

A thorough analysis of the accidents in the Polish building industry in years 1992–2004 is presented. The accident situation, if assumed to be a homogeneous phenomenon, is estimated based on the accident rate of minor, serious and fatal accidents and all the accidents jointly as well as based on the accident seriousness index. However, the accident situation is not a homogeneous phenomenon. The frequency of the particular kinds of accidents and their structure change over the years. The standardised accident rate (which takes into account all the kinds of accidents and their structure at the same time) is proposed for the estimation of the accident situation treated as a non-homogeneous phenomenon. It is constructed the model of development tendency for a phenomenon according to the information on the accident situation expressed by the accident rate and the accident seriousness index in the years 1992–2004.

Keywords: *building industry, accident rate, standardised accident rate, model of development tendency for accident situation*

1. Introduction

In comparison with other industries, the building industry is characterized by a high level of hazards to the life and health of workers and a high accident rate. In recent decades, the level of work safety in the Polish building industry has been affected both negatively and positively. The changes associated with, among others, ownership transformations had a negative effect on work safety. The owners of start-up enterprises desire to reap large profits in a short period of time which in many cases entailed cuts in the expenditures on work safety. On the other hand, Poland aspiring to be a member of the EU had to meet many obligations, among others, to bring its law up to the EU standards. Figures 1, 2, 3 present the accidents in the Polish building industry in years 1992–2004 against the background of the above standards [1–8]. Figures 1, 2 and 3 present the total number of persons injured in accidents, in serious accidents and in fatal accidents at work in building industry, respectively. According to Figures 1, 2, 3 the number of persons injured in accidents at work shows a downward tendency in the succeeding years.

The above results are not reliable enough for a correct estimation of the level of work safety and for taking some preventive measures. However they might be the basis for further analysis. The histograms presented in Figures 1, 2, 3 do not show, for example, how often the accidents of persons happen, what is the level of accident seri-

ousness and what kind of development tendency for accident situation is in building industry now. There is no model to estimate this tendency based on bibliography. Therefore such a model was presented in this article.

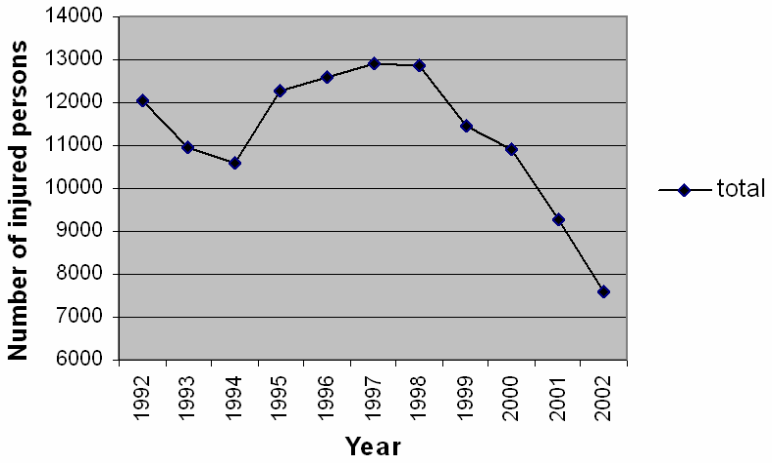

Fig. 1. A total number of persons injured in accidents at work in building industry

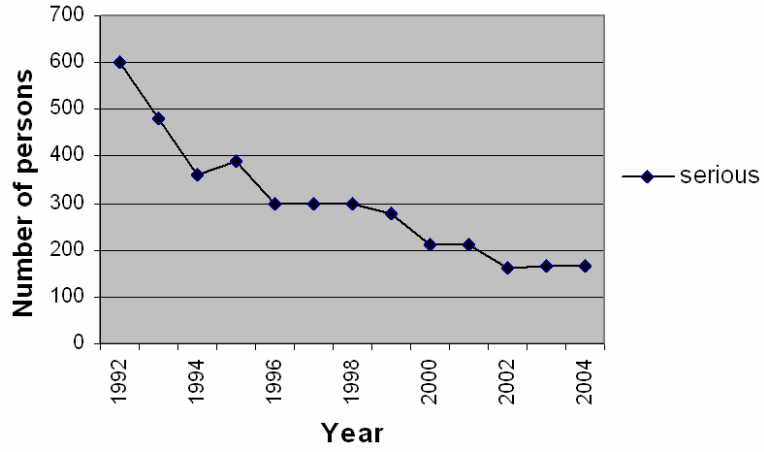

Fig. 2. The number of persons injured in serious accidents at work in building industry

Until now in bibliography the accident situation has been estimated as a homogeneous phenomenon using the standardised accident rate of total, minor, serious and fatal accidents and the accident seriousness index [12]. However, in reality, this approach is wrong, therefore the author has assumed that the accident situation is a non-homogeneous phenomenon.

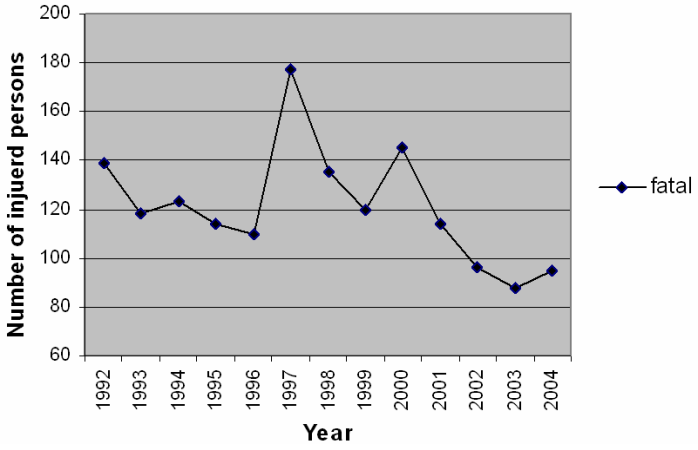

Fig. 3. The number of persons injured in fatal accidents at work in building industry

2. The rates of accident situation

Accident situation is a negative and undesirable occurrence. Therefore, the estimation of an accident situation is considered to be a very important process in receiving information/data. It informs us about the present situation and enables the present data/information to be compared to the previous ones. Additionally it gives the reasons for reduction of the number of accidents.

2.1. Accident situation as a homogeneous phenomenon

The accident rates and the accident seriousness index are very useful for the analysis of accident situation as a homogeneous phenomenon [9].

The accident rate $W_{i,1000}$ provide us with information about the level of individual risk of loss of life or health at work during a working process. The accident rate is usually a ratio of the number of people injured in accidents to the number of people employed, or to the output of production or to the hazard exposure time [10]. In the analysis, presented in the article, the accident rate is described by relation (1) and it is the number of persons injured in accidents at work per 1,000 employees

$$W_{i,1000} = \frac{Lw_i}{Z}1000, \tag{1}$$

where:

Lw_i – the number of persons injured in accidents at work,

$i = 0$ – the total number of all accidents,

$i = 1$ – the minor accidents,

$i = 2$ – the serious accidents,

$i = 3$ – the fatal accidents,

Z – the number of employees.

One of the major consequences of accidents at work is employees' absence from work. It is measured by the accident seriousness index, which is a ratio of the number of workdays lost, as a result of the absence of the injured persons, to the number of all accidents. The index is expressed by the following relation:

$$W_c = \frac{\sum_{j=1}^{Lw}\sum_{i=1}^{2} ds_{i,j}}{Lw}, \tag{2}$$

where:

$ds_{i,j}$ – the number of workdays lost as a result of the absence of the injured person,

$i = 1$ – the minor accidents,

$i = 2$ – the serious accidents,

$j = 1,..., Lw$,

Lw – the total number of minor and serious accidents,

$Lw = Lw_1 + Lw_2$.

One should note that the subscript is a measure of the seriousness of only minor and serious accidents.

2.2. Accident situation as a non-homogeneous phenomenon

The accident situation is not a homogeneous phenomenon. The frequency of the particular kinds of accidents and their structure have changed over the years. For this reason the standardised accident rate, which takes all the kinds of accidents and their structure into account at the same time, is proposed in order to estimate of the accident situation [10, 11]. An algorithm for calculating this rate is proposed below. The algorithm is based on the following assumptions:

Assumptions:

1. Accidents at work are divided into 3 generic groups: minor accidents, serious accidents and fatal accidents.
2. The structure of accidents is understood as the share of the number of accidents belonging to a given group in the total number of accidents and it is described by the following relations:

$$S_i = \frac{Lw_i}{Lw}; \qquad \sum_{i=1}^{3} S_i = 1; \qquad Lw = \sum_{i=1}^{3} Lw_i. \tag{3}$$

Algorithm:

1. Divide the accidents, which occurred in a considered period of time, into the above 3 generic groups.

2. Calculate the accident rates for the generic groups according to relation (1).

3. Select one generic group of accidents to be the basis for the standardisation of the other groups; the accident rate for the selected base group is:

$$W_{p,1000} = W_{i,1000}; \qquad i = 1, 2, 3. \tag{4}$$

4. Calculate for each group the so-called equilibrated accident rates in relation to the base accident rate from the relation:

$$Wz_{i,1000} = \frac{W_{i,1000}}{W_{p,1000}}; \qquad i = 1, 2, 3. \tag{5}$$

The equilibrated accident rate means that if in the base group one accident happened per 1,000 employees, then (for the same accident structure as the one which occurred in the analysed period of time) the accident rate for 1,000 employees in the other groups would correspond to the calculated equilibrated accident rate.

5. Calculate the equivalent values in each group of accidents. This is a number specifying the weight of an accident in a given group in relation to the weight of the base accident (which is equal to unity). The above index is calculated from the relation:

$$\gamma_i \, Wz_{i,1000} = \gamma_p \, W_{p,1000} = 1, \qquad \text{hence } \gamma_i = \frac{1}{Wz_{i,1000}}. \tag{6}$$

6. Calculate the standarised accident rate from the relation:

$$W_S = \frac{\sum_{i=1}^{3} \gamma_i Wz_{i,1000}}{\sum_{i=1}^{3} \gamma_i}. \tag{7}$$

The subscript in relation (7) expresses a heterogeneous accident situation as regards the structure and kind of accidents as one number specifying the aggregate frequency of accidents per 1,000 employees.

3. Model of development tendency and its verification

It is constructed the model of development tendency for accident situation for the period of time $<t_1,...,t_n>$ including the years 1992–2004. The sequence of observations $\{(t_1,w_{i,1}),...,(t_k,w_{i,k}),...,(t_n,w_{i,n})\}$ is obtained for the succeeding years of the period ex-

amined. They are expressed by the pair of variables t_k,$w_{i,k}$, where: t_k denotes the succeeding years of the period examined, k = 1,..., n, and $w_{i,k}$ denotes the level of the phenomenon monitored, i = 0, 1, 2, 3, s, c.

The phenomena monitored were the following:

- the accident rates: total ($w_{0,k}$), minor ($w_{1,k}$), serious ($w_{2,k}$), fatal ($w_{3,k}$),
- the standardised accident rate ($w_{s,k}$),
- the accident seriousness index ($w_{c,k}$).

The trend function is a statistic form of the development tendency description of the phenomenon examined [13]. The general trend function is expressed by the formula:

$$w_i = f_i(t) + u_{i,t}, \qquad i = 1, 2, 3, s, c. \tag{8}$$

where:

$f_i(t)$ – a hypothetical trend function for the phenomenon i,

$u_{i,t}$ – a random element, which measures the accidental deviation of the variation w_i from the trend line.

It is assumed that the trend function is a general model of the development tendency for accident situation and it has a form of the j-grade polynomial, i.e.

$$f_i(t) = \alpha_0 + \alpha_1 t^1 + ... + \alpha_i t^j; \qquad \alpha_j \neq 0, \tag{9}$$

where α_j is the parameter of the j-grade polynomial.

The model of the development tendency may be presented in the matrix form, if there are n observations of the vector of the variables W_i and n observations of the vector of the variables T:

$$W_i = T\alpha_i + U_i, \qquad i = 1, 2, 3, s, c, \tag{10}$$

where:

$$W_i = \begin{bmatrix} w_{i,1} \\ w_{i,2} \\ ... \\ w_{i,k} \\ w_{i,n} \end{bmatrix}, \qquad T = \begin{bmatrix} 1 & t_1 & t_1^2 & ... & t_1^j \\ 1 & t_2 & t_2^2 & ... & t_2^j \\ ... & ... & ... & ... & ... \\ 1 & t_k & t_k^2 & ... & t_k^j \\ 1 & t_n & t_n^2 & ... & t_n^j \end{bmatrix}, \qquad \alpha_i = \begin{bmatrix} \alpha_{i,0} \\ \alpha_{i,1} \\ \alpha_{i,2} \\ ... \\ \alpha_{i,j} \end{bmatrix}, \qquad U_i = \begin{bmatrix} u_{i,1} \\ u_{i,2} \\ ... \\ u_{i,k} \\ u_{i,n} \end{bmatrix},$$

where:

W_i – the vector [n] of observed values of the variable w_i,

T – the matrix $[n, j+1]$ of observed values of time variable,

a_i – the vector $[j+1]$ of the unknown parameters $\alpha_0 \ldots \alpha_j$,

u_i – the vector $[n]$ of random elements $u_1, \ldots, u_n$.

The unknown parameters α of the trend function are estimated according to the least squares method [14].

The determination index is accepted as a measure of adjustment of the model to the real values. This index informs which part of the general variation of characteristic W_i is described by the model. The determination index is calculated according to [14]:

$$R_i^2 = \frac{a_i^T (T^T T) - n(\overline{w_i})^2}{W_i^T W_i - n(\overline{w_i})^2}, \quad i = 1, 2, 3, s, c, \tag{11}$$

where:

n – the number of observations,

$\overline{w_i}$ – an average value of the matrix W_i elements.

It is assumed that the model describes perfectly the phenomenon examined if the calculated value of the determination index is greater that 0.9. However, if the value of the determination index is greater than 0.8 the model describes adequately the phenomenon examined.

4. Results of accident situation analysis in building industry

Based on the number of persons injured in accidents at work in building industry and the number of employees it is estimated (according to formulae (1) and (2)) the accident rate and the accident seriousness index.

The diagrams representing the changes in the values of a total accident rate per 1,000 employees in the Polish building industry and the trend lines (represented by the 3-grade polynomial) are shown in Figure 4. The value of the determination index is greater than 0.83 which means that the model describes variation of the total accident rate in 83% and can be considered as a good one. The trend function has reached the maximum value in the years 1996–1997. In the years 1996–1997, we observed the maximum accident rate per 1,000 employees in the Polish building industry. The trend function has been decreasing during the next years.

The curve representing the values of a serious accident rate per 1,000 employees in the Polish building industry and the trend line (described also by the 3-grade polynomial) are shown in Figure 5. In this case, the value of a determination index is very great and reaches 0.946. This means that the model perfectly describes the phenomenon examined. The trend function (which represents the changes in the values of a serious accident rate per 1,000 employees in the Polish building industry) has a downward tendency during the whole period examined.

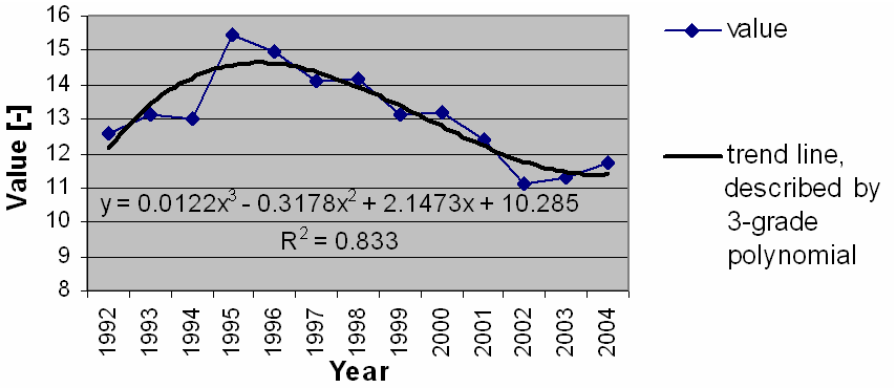

Fig. 4. The changes in the value of a total accident rate per 1,000 employees in building industry and trend line

The changes in the value of a fatal accident rate per 1,000 employees in the Polish building industry are shown in Figure 6. According to the diagram, the phenomenon is characterized by high variability during the period of time examined. In the case of a fatal accident rate, we analysed a few models for the development tendency such as: linear function, power function, logarithmic function, exponential function and 3, 4, 5, 6-grade polynomial. Unfortunately, the functions analysed do not describe the development tendency with a sufficient accuracy. The maximum value of the determination index (equal to 0.2339) is obtained for the 6-grade polynomial. This means that the 6-grade polynomial describes the variation in the fatal accident rates only in 24%.

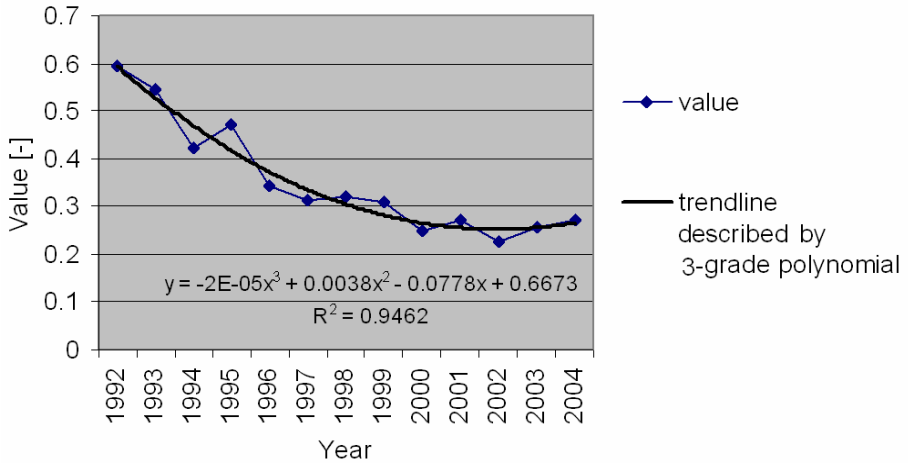

Fig. 5. The changes in the values of serious accident rate per 1,000 employees in building industry and trend line

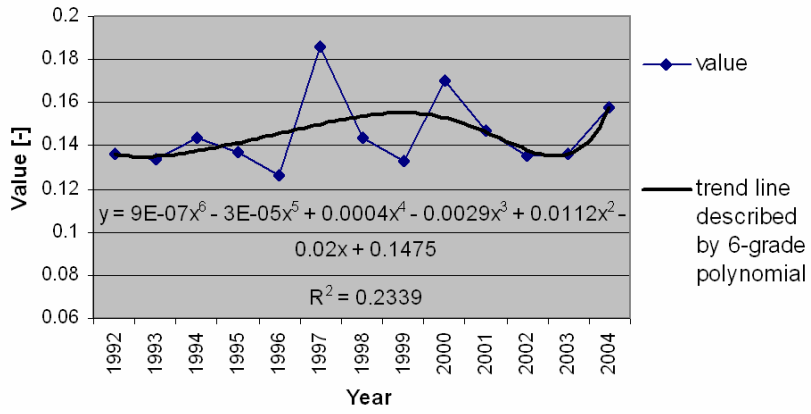

Fig. 6. The changes in the value of fatal accident rate per 1,000 employees in building industry and trend line

The changes in the value of accident seriousness index in the Polish building industry in the years 1992–2004 are given in Figure 7 which shows that this index in the Polish buildings industry has an upward tendency during the successive years. This proves that increasingly serious accidents take place which results in an increasingly larger number of workdays lost due to accident absenteeism. Indirectly, the above index represents also the economic losses sustained as a result of accidents and the effectiveness of prevention aimed at ensuring work safety. The development tendency is shaped by the linear function. The determination index for the linear function (presented in Figure 7) is equal to 0.9312, which means that the development tendency of the phenomenon examined is closely modelled by the function.

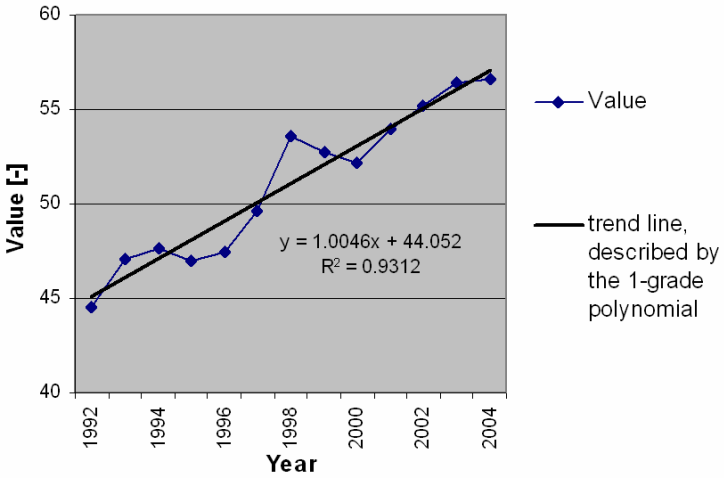

Fig. 7. The accident seriousness index and trend line

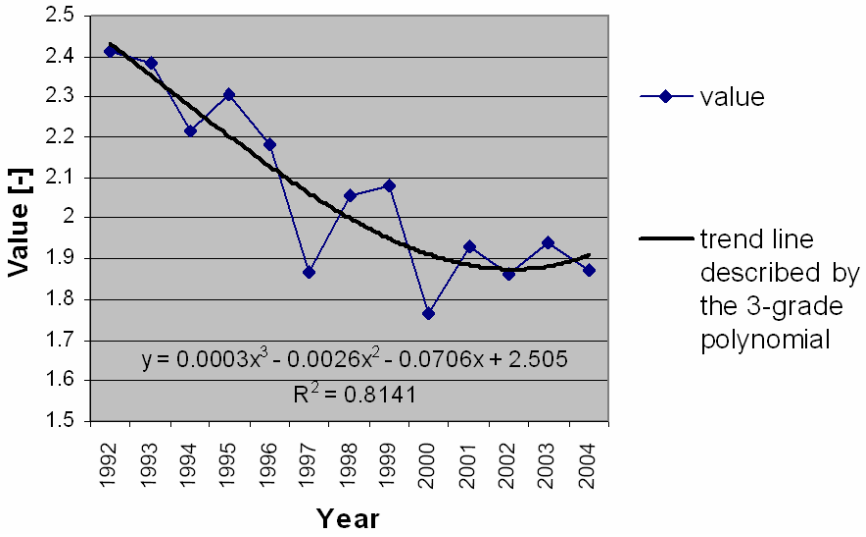

Fig. 8. The changes in the values of standardised accident rate per 1,000 employees in building industry and trend line

The changes in the value of standardised accident rate in the Polish building industry in the years 1992–2004, calculated according to the rules given in point 2, is shown in Figure 8. The 3-grade polynomial describes adequately the changes in the standardised accident rate. The determination index is 0.8141. The trend function reveals a downward tendency; however, it can be noticed a slight upward tendency of the standardised accident rate in year 2003.

5. Conclusions

Up till now, in bibliography the accident situation has been estimated as a homogeneous phenomenon based on the standardised accident rate of total, minor, serious and fatal accidents and the accident seriousness index. However, in reality, the accident situation is not a homogeneous phenomenon. Therefore, for estimating the accident situation as a nonhomogeneous phenomenon the author proposes the standardised accident rate, which makes it easier to follow the changes in the accident situation in a longer period of time.

The standardised accident rate takes into account a simultaneous contribution of all kinds of accidents to the accident situation as well as their structure. The value of the standardised accident rate shows a downward tendency in the years 1992–2004, which means that there is a continuous improvement of the work safety in the building industry. The above values are fully reliable to estimate accurately the level of work safety and to take some preventive measures.

According to the above analysis the *i*-grade polynomial is a general model of the development tendency for the accident situation in the Polish building industry. The trend function, represented by this polynomial, projects the changes taking place in the accident situation in most of the phenomena analysed. In the case of the total, serious accident rates and the standardised accident rate it is the 3-grade polynomial. The fatal accident rate is characterized by considerable fluctuations over the period examined. It makes it impossible to find the trend function which represents the phenomenon examined with a sufficient accuracy. Whereas, in the case of the accident seriousness index, the 1-grade polynomial is the trend function, which describes the development tendency of the phenomenon examined.

The model presented can be useful for forecasting the accident situation in the building industry and for taking some preventive measures (for instance, the new law standards).

References

[1] Accidents at Work in 1995 (in Polish), GUS, Warsaw, 1996.
[2] Accidents at Work in 1997 (in Polish), GUS, Warsaw, 1998.
[3] Accidents at Work in 1998 (in Polish), GUS, Warsaw, 1999.
[4] Accidents at Work in 1999 (in Polish), GUS, Warsaw, 2000.
[5] Accidents at Work in 2001 (in Polish), GUS, Warsaw, 2002.
[6] Accidents at Work in 2002 (in Polish), GUS, Warsaw, 2003.
[7] Accidents at Work in 2003 (in Polish), GUS, Warsaw, 2004.
[8] Accidents at Work in 2003 (in Polish), GUS, Warsaw, 2005.
[9] Hoła B.: *Accident Situation in Polish Construction Industry*, International Conference on Developments in Building Technology, Bratislava, 2001.
[10] Hoła B.: *Model of development tendency of accident situation in construction industry*, Archives of Civil Engineering, 2006, LII, 1.
[11] Hoła B.: *Analysis of accident situation in polish construction industry in period proceeding accession to the european union*, Journal of Civil Engineering and Management, 2004, Vol. X, Supplement 2, 107–113.
[12] Studenski R.: *Organisation of Safe Work in Enterprise* (in Polish), Wydawnictwo Politechniki Śląskiej, Gliwice, 1996.
[13] Ostasiewicz S. et al.: *Statistics: Elements of Theory and Purpose* (in Polish), Wydawnictwo Akademii Ekonomicznej, Wrocław, 1999.
[14] Zeliaś A.: *Statistics Methods*, Polskie Wydawnictwo Ekonomiczne, Warsaw, 2000.

Tendencja rozwojowa wypadkowości w budownictwie

Przedstawiono analizę wypadkowości w budownictwie polskim w latach od 1992–2004. Wypadkowość jako zjawisko jednorodne oceniono na podstawie wskaźników częstości wypadków ciężkich, śmiertelnych i wszystkich wypadków łącznie oraz na podstawie wskaźnika ciężkości wypadków. Wypadkowość nie jest jednak zjawiskiem jednorodnym. W kolejnych

latach zmienia się bowiem częstość poszczególnych rodzajów wypadków i ich struktura. Aby ocenić wypadkowości jako zjawisko niejednorodne, zaproponowano standaryzowany wskaźnik częstości wypadków, uwzględniający jednoczesny udział w wypadkowości wszystkich rodzajów wypadków i ich strukturę. Na podstawie informacji o wypadkowości wyrażonej za pomocą wskaźników częstości wypadków oraz ciężkości wypadków w latach 1992–2004 zbudowano model tendencji rozwojowej zjawiska.

ARCHIVES OF CIVIL AND MECHANICAL ENGINEERING

Vol. VI 2006 No. 3

Information about PhD thesis at the Civil Engineering Faculty and the Mechanical Engineering Faculty of Wrocław University of Technology

Title: *Feature-based computer-aided process-planning system* (in Polish) *Opracowanie systemu wspomagającego planowanie procesów obróbkowych metodą obiektów elementarnych*

Author: Kamil Krot
Supervisor: Professor Edward Chlebus, Wrocław University of Technology
Promoting Council: Scientific Council of Institute of Production Engineering of Wrocław University of Technology
Reviewers:
Professor Józef Gawlik, Cracow University of Technology
Professor Józef Krzyżanowski, Professor of Wrocław University of Technology
Date of PhD thesis presentation: September 19th, 2005
PhD is available in Main Library of Wrocław University of Technology
The monograph contains: 145 pages, 96 figs, 9 tables, bibliography: 101 items
Keywords: *CAPP, process planning, features*

Abstract: The aim of the monograph was to establish a framework for automatic process-planning system, based on recognized features and using an expert system. The system will be designed for the planning of machining prismatic parts on the basis of 3D CAD data. In the first stage of the project includes the analysis of the input data from a CAD system is carried out. Then the algorithms of recognising functional construction and technological features from solid 3D CAD models are developed. The input models are stored in neutral data formants: IGES or STEP. In the next stage, recognized features are clssified. An expert system is used to plan manufacturing processes. The expert system includes the following modules: inferences, technological knowledge database, machine tool database and tool database. The final module of the designed CAPP system generates output data, i.e., CL data files necessary to create programs for NC machine tools.

Title: *Monitoring of energy dissipation in hydraulic shock absorbers* **(in Polish)** *Monitorowanie rozpraszania energii w amortyzatorach hydraulicznych*

Author: Wojciech Poprawski
Supervisor: Doctor Józef Krzyżanowski, Wrocław University of Technology
Promoting Council: Scientific Council of the Institute of Production Engineering and Automation of Wrocław University of Technology
Reviewers:
Professor Czesław Cempel, Poznań Univeristy of Technology
Professor Stanisław Piesiak, Professor of Wrocław University of Technology
Date of PhD thesis presentation: March 24th, 2005
PhD is available in Main Library of Wrocław University of Technology
The monograph contains: 89 pages, 62 figs, 7 tabs, bibliography: 40 items
Keywords: *damping, shock absorbers, condition monitoring*

Abstract: On-line condition monitoring system for railway hydraulic shock absorbers is presented. The shock absorbers are used for controlling the yaw movement of the bogie, high-speed ICE II trains. Uncontrolled yaw (hunting) movement can cause the instability of the bogie, which may lead to the derailment of the train. The hydraulic shock absorbers are the devices widely used in automotive and railway applications. They are the subject of regular servicing. The railway shock absorbers are tested in the special testing rigs after dis-asseblying from the train. The testing procedure is very expensive and time consuming and generates high idle cost. Application of the condition monitoring system of the anti-yaw shock absorbers can increase the safety and reduce the maintenance costs of the train. The train operator will be informed about the condition of shock absorbers, thus the shock absorbers will be replaced if needed, not according to the mileage schedule. The thesis deals with the condition monitoring system for the choice of the measured variables, which describe the properties of shock absorbers. The choice is based on numerical and laboratory experiments. The testing has been performed on the dampers with simulated failures. The performance of shock absorbers can be described using the graphs on the phase plane, combining the force acting on the piston rod and the velocity of the movement between piston and cylinder. The artificial neural networks (ANN) have been successfully applied in the inference engine. The thesis presents the results of the learning of the neural networks and the results of validation testing.

Title: *The usefulness of fractal analysis for assessing geometrical state of machined surface assessment* (in Polish)
Przydatność analizy fraktalnej do oceny stanu geometrycznego powierzchni obrobionej

Author: Marcin Wiącek
Supervisor: Professor Marek Miernik, Professor of Wrocław University of Technology
Promoting Council: Scientific Council of the Institute of Production Engineering of Wrocław University of Technology
Reviewers:
Professor Stanisław Adamczak, Kielce University of Technology
Professor Wit Grzesik, Opole University of Technology
Date of PhD thesis presentation: February 18th, 2005
PhD is available in Main Library of Wrocław University of Technology
The monograph contains: 128 pages, 85 figs, 7 tabs, bibliography: 98 items
Keywords: *machining, surface roughness, fractal analysis*

Abstract: Theoretical model of surface roughness forming, factors and parameters that describe the surface geometrical state as well as the disturbances in real surface after machining were presented. The usefulness of chaotic attractors, Lapunov's exponent and fractal dimensions was evaluated in order to assess the geometrical structure of surface after machining. Chaotic attractors and Lapunov's exponents were recognized to be useless for evaluating the surface geometrical structure; however, of many definitions of fractal dimensions the box dimension was considered to be most useful. Experiments were carried out in lathe. Three materials with different properties and metallographic structures, i.e., steel for treatment C55E, gray cast iron EN-GJL-150 and brass CuZn40Pb2, were turned. The measurements of the of surface geometrical structure were carried out on the Rank Taylor Hobson roughness meter model Form Talysurf 120L. For all three materials the fractal dimension was measured as a function of machining parameters, i.e., feed and cutting speed. Moreover, the correlation between the values of fractal dimensions and roughness parameters *Ra* and *Rku* for 2D and *Sa* and *Sku* for 3D measurements were analysed. Also comparative analysis of fractal dimension values for all there materials was made. Cognitive and utilitarian conclusions as well as further directions of investigations were given.

Title: *Method of machines diagnosing in emergency overloading states* (in Polish) *Metoda diagnozowania maszyn w stanach przeciążeń awaryjnych*

Author: Marcin Kowalczyk
Supervisor: Doctor Franciszek Przystupa, Professor of Wrocław University of Technology
Promoting Council: Institute of Machines Design and Operation of Wrocław University of Technology
Reviewers:
Professor Andrzej Buchacz, Silesia University of Technology
Professor Eugeniusz Rusiński, Wrocław University of Technology
Date of PhD thesis presentation: Novemeber 8th, 2005
PhD is available in Main Library of Wrocław University of Technology
The monograph contains: 147 pages, 140 figs, bibliography: 69 items
Keywords: *diagnoser, states of failure risk, finite element method, working machines*

Abstract: The monograph deals with as the diagnostic method assisting the operation in order to avoid the emergency overload of machines. The states that precede the failure generated by a sudden, random and vehement mechanical loadings impacts are considered. In the study, two periods in which it is possible to conduct the identification of technical state were distinguished. The first one is the state of failure risk that starts after the external impact occurrence, and the second one is the period that precedes an emergency. The main part in diagnosing the state of the machine has the diagnoser. Diagnosing in the emergency state undergoes by conducting the numerical simulation on the model of diagnosis object, whiose run is being corrected by the measurements on real object. Tuning the diagnoser's model state to diagnosed object according to the authors method occurs in all diagnosing cycle and then the calculations are continued in order to identify the technical state. Diagnosing in the time before the emergency state may progress according to the random symptoms, that occur in the case of mining rocks by the bucket wheel excavators. The criterial parameters of the method that provided the selection of loadings boundary value for diagnoser were indicated as well as the way of their determination based on the periodic measurements.

The study also presents an own probabilistic-deterministic model of loadings for this kind of machines.

Information about habilitations at the Civil Engineering Faculty and the Mechanical Engineering Faculty of Wrocław University of Technology

Title: *Fungal biodeterioration in buildings* (in Polish) *Biodeterioracja pleśniowa obiektów budowlanych*

Author: Barbara Rymsza
Promoting Council: Council of Civil Engineering Faculty
Reviewers:
Professor Krzysztof Krajewski, Professor of Warsaw Agricultural University
Professor Zofia Żakowska, Professor of Technical University of Łódź
Professor Lech Śliwowski, Wrocław University of Technology
Professor Adam Latała, Opole University
Date of habilitation colloquium: 26th April, 2006
Habilitation monograph edited by Poznań University of Technology, 2003, is available in Main Library of Wrocław University of Technology.
The work contains: 117 pages, 36 figs, bibliography: 228 items
Keywords: *building physics, mycology, durability and strength of building, protection against corrosion*